Bacterial contact inhibition: single cell to microcolony level analysis using experimental and in silico approaches

Sarah Rixham

PhD
Univeristy of York
Department of Biology

December 2019

Abstract

Bacteria have evolved a diverse range of strategies for survival. To colonise a niche and source nutrients, cooperation and antagonism can both prove advantageous. Contact dependent toxin insertion is one way that bacteria are able to antagonistically manipulate growth of other bacteria in close proximity, but the effect of different contact inhibition systems on the spatial structure of bacterial populations has not been explored. The type VI secretion system (T6SS) and contact-dependent inhibition (CDI) are two contact inhibition systems with differing potency; T6SS is highly toxic whereas CDI has a subtler effect on susceptible target cells. Here I show, with an interdisciplinary blend of microscopy and computational modelling, that the potency of the system determines structure in binary competitions. Tracking single cells during competition with phase contrast microscopy shows that both the rate of inhibition and the toxicity of the system (measured by the extent of growth rate reduction of target cells) defines the system's potency. Simulations exploring the range of these two inhibition potency parameters show continuous change in the structure of microcolonies, from intermixing at low potency, to reduced interaction border and enforcement of clustering at high potency. A T6SS effector mutant with reduced inhibition rate was used to validate simulation predictions, using the fractal dimension as a statistical measure of microcolony structure. Combining empirical and in silico data with spatial statistics has allowed identification of fine scale structural changes imposed by incremental changes in inhibition potency of contact inhibition systems. The methods developed in this analysis can be used to further investigate the diverse range of toxins from these two contact inhibition systems and how other interbacterial interactions affect bacterial population structure. A better understanding of factors affecting population structure is important to understand how natural multispecies populations establish and maintain themselves.

Contents

List of Tables

List of Figures

Acknowledgements

Step by step, I walked the path,
Step by step, I climbed the mountain,
Step by step, I walked the line,
Between success and failure,
The line between the highest points,
The deep crevasses to be crossed,
The meaning and the loss thereof,
What has guided me through these convoluted fractals of the way?
The credit goes to my supervisors Marjan van der Woude and Jamie Wood,
They knew how to advise and encourage,
They know the turns of the path well,
And have an ethereal understanding of individual's needs,
The sharing of passion kept me on the track,
These thanks go to Caroline, Ioannis and Mike,
Who shared and intertwined their path with mine,
And when the mountain came insurmountably steep,
There to give me a gentle push my parents, Penny and Andy,
And the rest of my family,
The (10,000) false peaks came again and again,
Steph was there for me,
And so too close friends,
Then,
There I was,
Looking out over the views,
Inversion of clouds below covering my former route,
Only the euphoric sky above,
Encompassing me in bright, warm, tangible, scented luminosity,
I now continue walking over my bridge,
The highline,
That has been here for me,
On the road to,
The next high peak.

Author's declaration

I declare that this thesis is a presentation of original work and I am the sole author, unless indicated. This work has not previously been presented for an award at this, or any other, University. All sources are acknowledged as References. This work was carried out in parallel with work published by Bottery et al. [1], therefore a similar approach and techniques were used. The fractal dimension Python script used for analysis was written by Michael J Bottery and is unpublished at the time of thesis submission. Strains used were from the labs of Christopher Hayes and David Low at UCSB. Some competitive index data was carried out by Sonya Donato, UCSB and is indicated in the text.

1 Introduction

1.1 Microbial Communities

We live in a microbial world. Microbes shaped the earth and made it inhabitable for eukaryotic life using a range of biochemical processes that have made the atmosphere and soil and used photosynthesis to harness energy from the sun [2]. Now, although invisible to the eye, microbes are everywhere inhabiting many niches that were thought to be uninhabitable [3, 4]. They can adapt to niches however extreme, due to their fast growth and mutation rate as well as their promiscuity for DNA transfer [5]. They play important roles in the world today such as degradation of organic matter [6], removal of environmental contaminants [7], nutrient cycling [8] and controlling climate and weather [4, 9]. Microbes reside on and in all multicellular organisms to provide diverse functions including the development of immune systems, protection against pathogens and nutrient metabolism [10, 11]. Therefore, understanding how microbial communities work is important for advances in human health [12], industrial processes [13] and climate change [4],

Bacteria are found almost ubiquitously in densely packed communities in the oceans, atmosphere, soil and in and on eukaryotic organisms [14]. They are predominantly found in structured communities called biofilm [15]. In biofilms bacteria secrete components to create a structural matrix that can support a heterogenic community [16]. These structured polymicrobial communities can survive deleterious environmental challenges and thrive in a wide range of environments [3].

In complex communities local interactions such as communication, cooperation and competition are involved in shaping community structure [17, 18]. Although cooperation is advantageous to share nutrients and other public goods, it has been shown in complex communities such at the gut that competition may be a strong driver of stability [19].

1.2 Bacterial competition systems

Bacterial competition comes in two main forms: exploitative and interference. Exploitative competition is an indirect mechanism where bacteria compete for space, nutrients and limited resources [20]. In contrast, interference competition is direct antagonistic interactions using a range of molecules to directly attack competitors. These can be secreted molecules such as bacteriocins, antibiotics and antimicrobial peptides [21], or contact dependent mechanisms which include the type VI secretion system and subsets of type V secretion such as contact-dependent inhibition [21].

1.3 Interference competition

1.3.1 Types of bacterial weaponry

Bacteria have a broad range of weapons from biological to mechanical and chemical. Biological mechanisms of antagonism include phage, and mechanical systems cause damage to the cell membrane integrity. However, the chemical armoury is the most extensive with many secreted toxins, and systems that insert toxins into neighbours through secretion machinery on the cell surface [21].

The are several different types of chemical toxins including small molecules and large proteins with enzymatic activity. The main mechanisms of actions are to attack the core machinery such as DNA, RNA, and translation and transcription machinery or to disrupt the integrity of the cell wall or membrane. Polymorphic toxins which are found in both diffusible and contact dependent systems can give some insight into how bacteria have created such a large toxic armoury.

The polymorphic toxin systems are a distinct group of bacterial toxins with a particular molecular and genetic organisation, which have been identified in all major bacterial lineages [22]. These groups of toxins is defined by modularity of the toxin, with a C-terminal toxin and N-terminal transport domain. Downstream of the toxin gene in the same operon an immunity protein is located as well as cassettes encoding ‘orphan’ toxin/immunity pairs containing alternative toxins. The polymorphic toxin systems encode a diverse range of toxins including nucleases, deaminases, peptidases and protein pores [23]. Specific toxins often target related bacteria but the C-terminal toxin domains are widespread. Toxin systems that are part of the polymorphic toxin systems include the colicins in *E. coli*, pyocins from pseudomonads, MafB from *Neisseria* spp. and contact dependent systems including contact-dependent inhibition and some effectors of the type VI secretion system such as the Rhs proteins [22]. There is evidence to suggest that in polymorphic toxin systems toxin immunity pairs can undergo homologous recombination and horizontal gene transfer allowing a large array of toxins to evolve [23, 24].

1.3.2 Ecological role of bacterial competition systems

To understand the role of toxin systems on community structure, simple experimental model systems have been used. In unstructured environments the outcome of competition between a toxin producing inhibitor strain and a susceptible target strain has been shown to be dependent on the frequency of each cell type [25]. Inhibitor strains need a higher starting frequency to outcompete target cells due to the cost of toxin production, giving the target a growth rate advantage. Therefore, the more abundant strain can take over the population. This relationship between cost and inhibition means, depending on the starting conditions one species is always outcompeted and goes extinct.

Chao and Levin [25] extend their investigation to spatially structured environments showing coexistence can be created. Stability can then be resource dependent with inhibitors doing better in higher nutrient environments. Spatial structure allows local concentration of nutrients to build up so inhibitors can persist despite slower growth. Durrett and Levin [26] back up these experiments with computational spatial modelling. They show that structured environments allows inhibitor cells to expand in the population even when starting at lower density than target cells. Durrett and Levin [26] expand their computational model to look at a three strain competition which includes a cheat which does not produce toxins but is resistant to intoxication. In their spatial models coexistence can occur but in well mixed models there is always a winner. Kerr et al. [27] look at three species dynamics using a computational model and experimentation. They show that growth on a surface is needed for stability and maintaining diversity in populations. The results of these examples of diffusible toxin competition systems suggest that spatial structure is vital for population stability and coexistence of competing strains.

These examples of how structure and competition drive stability of polymicrobial communities are so far based upon diffusible (long range) toxins systems but there are also a range of contact dependent (short range) toxin systems that have an effect on fine scale structure and interactions in populations. The two main types of contact inhibition are the type VI secretion (T6SS) and contact-dependent inhibition (CDI). It has been recently shown that the T6SS also has some inhibitory activity but this so far has not been shown in more than one species so this system will not be mentioned [21]. Both T6SS and CDI systems are widespread in gram negative bacteria, including many pathogens and are likely to play a role in community structure and population dynamics [28, 29].

1.3.3 Contact inhibition

1.3.3.1 Contact-dependent inhibition

Contact-dependent inhibition was the first contact dependent inhibitory system discovered in 2005 in the uropathogenic bacteria *Escherichia coli* EC93 [30]. The strain, which dominated the rat gut that it was found in, was shown to inhibit growth of *E.coli* K-12 in planktonic culture. Aoki et al. [30] showed direct contact is necessary for inhibition, by separating strains with a porous membrane and no longer achieving growth inhibition. CDI systems have since been found in other gram-negative bacteria including α-, β-, and γ-proteobacteria [28]. There are also homologous systems in gram-positive bacteria such as *Bacillus* species [31].

CDI is encoded in an operon containing three genes: *cdiA*, *cdiB* and *cdiI* [30]. CdiA and CdiB make up the two partner secretion system, type Vb secretion [30]. The two partner secretion system exports large exoproteins (TpsA) across the cell membrane using a β-barrel pore forming protein (TpsB). CDI proteins CdiA and CdiB show sequence homology with other TpsA and TpsB proteins, respectively [32]. Along with the secretion system, the *cdi* gene cluster includes an immunity protein, CdiI. In gram negative bacteria there are two conformations of the CDI operon: *cdiBAI* found in *E. coli* and other enterobacteria and *cdiAIB* found in *Burkholderia* spp. [28].

CdiB is a 64.5kDa outer membrane β-barrel protein that transfers CdiA across the membrane to contact target cells [32, 33]. CdiA is a modular protein composed of a conserved N-terminal and a heterogeneic C-terminal (CT) [28]. The N-terminal contains a two-partner secretion transport domain [34] and a filamentous haemagglutinin repeat domain [28] which is predicted to form a β-helical rod-like structure [35]. In the central region a receptor binding domain [34] and a YP domain are found [36]. A second filamentous haemagglutinin repeat is found before the conserved VENN motif (or NxxLYN in *Burkholderia*) which demarks the start of the CT toxin region [28]. This CdiA-CT region is then split into a translocation domain which binds to inner membrane receptors to import the toxin into the cytoplasm, and the toxin domain [37].

Ruhe et al. [36] investigated the mechanism of CdiA secretion and interaction with the target cell. They show that the secretion of CdiA is arrested with the CdiA-CT still in the periplasm (Figure 1). Using electron cryotomography they measured that the N-terminal protrudes ~33nm away from the cell with the receptor binding domain at the distal end of the protrusion making a hairpin for the CT to stay in the periplasm. This arrest is dependent on the YP region, which is expected to be elongated. They also suggest a mechanism for entry of the CdiA-CT toxin into the target cell upon receptor binding: they show insertion is dependent on the filamentous haemagglutinin repeat 2 domain and suggest it is integrated into the target cell membrane to facilitate toxin delivery. So far three different CDI receptor binding classes have been characterised: BamA [38], heterotrimeric OmpF/OmpF [39] and Tsx nucleoside transporter [34]. With each outer membrane receptor there are also specific inner membrane transporters involved [37]

As well as the receptor specificity there are also extra regulatory steps in some systems: CysK acts as permissive factor in UPEC536 to activate the latent tRNase [40, 41], or activation of EC869 tRNase toxin by translation elongation factors [42].

To prevent auto-inhibition CdiI acts as an inhibitor for cognate CdiA-CT. Multiple *cdiA-CT* gene fragments linked with *cdiI* sequences form *cdiA-CT/cdiI* 'orphan' modules that are found in CDI containing genomes [43]. These orphan modules are mobile and can be exchanged between CDI systems of different bacteria. Evidence for horizontal gene transfer of CDI systems comes from Ruhe et al. [44] who show CDI systems are found on genomic islands and can stabilise mobile genetic elements [44]. Species may also contain more than one CDI operon [28].

Although CDI was initially discovered as a competitive mechanism, it is also involved in other processes including biofilm formation [45–48], persistence [49] and signalling [50]. Garcia et al. [45] were the first to show CDI involvement in biofilm formation in *Burkholderia thailandensis* by showing that the *bcpAIOB* and BcpA activity is needed for biofilm formation. Heterogeneic expression of *bcpAIOB* is needed and inhibition is not involved as all cells can express the BcpI immunity protein. Garcia et al. [50] extend this by showing that contact dependent signalling switches on genes involved in biofilm formation in *B. thailandensis*. CDI promotion of biofilm formation has also been shown in EC93 but through a different mechanism [47]. Ruhe et al. [47] report CdiA-BamA interaction but also BamA independent auto-aggregation and they identify different regions in the CdiA protein that mediate these adhesive properties. In contrast to the BcpA system, CdiA does not need catalytic activity for biofilm genes to be expressed. Conversely Roussin et al. [48] show that in an *Acinetobacter baumannii* environmental isolate the absence of CDI promotes adhesion and biofilm formation.

Another community function of CDI is the involvement in persister formation found in EC93 [49]. Ghosh et al. [49] show that cells with low levels of CdiI are subject to the toxic activity of CdiA from neighbouring clonal cells. Low levels of toxin activity through a feedforward loop of CdiI degradation leads to persister formation. This occurs in a population in a density dependent manner as a possible bet-hedging strategy in large populations. These cooperative traits suggest that CDI does not only mediate competition but also facilitates cooperation.

1.3.3.2 Type VI secretion

The type VI secretion system (T6SS) was discovered in 2006 when described as a virulence mechanism in *Vibrio cholerae* with Hcp and VgrG proteins being identified as potential effectors [51]. The gene cluster and some of its components were described earlier due to some components being similar to those found in the type IV secretion system [52]. Due to its similarity to the phage tail, and its fascinating structure and mechanism there has been a large amount of research on the T6SS, giving its name a more prominent role in the understanding of inter-bacterial competition than CDI. The T6SS is widespread with it being found in proteobacteria in >25% of genomes [29].

The T6SS is made up of 13-14 core components (TssA-M, PAAR) making up the membrane complex, cytoplasmic base plate, contractile sheath and inner tube puncturing structure. The gene structure (six subfamilies) and genetic regulation can differ between species as well as there being three evolutionary divergent systems, $\mathrm{T6SS^{i}}$ being the canonical system found in proteobacteria [53].

Toxins are inserted into adjacent cells by contraction of the TssBC sheath which shoots the Hcp inner tube, VgrG spike and PAAR tip with associated effectors through the outer membrane of neighbouring bacteria. Effectors can be covalently (specialised) and non-covalently (cargo) attached to Hcp, VgrG or PAAR allowing several effectors to be inserted at once [53]. The loaded and firing conformations are shown in Figure 1.

The range of effectors include peptidoglycan amidases to break down the cell wall, lipases to breakdown the inner membrane as well as pore forming toxins and nucleases. Cell wall and cell membrane effectors act in the periplasm. Nucleases need to be transferred to the cytoplasm, the mechanism for this may be effector specific [53]. The ability to insert several toxins gives the T6SS an advantage in that it can attack several cellular systems at once, and compensate for resistance development, acquisition of immunity proteins or changing environments affecting the efficacy of toxins [54].

T6SS effectors are found along with their cognate immunity proteins and can be transferred between systems or strains to create a dynamic arms race [24]. Immunity proteins can also be found on their own as ‘orphans’.

T6SSs are highly regulated being controlled by: environmental factors, biofilm regulation or pathogenicity [24, 55, 56]. This can be through quorum sensing [57–60], post-translational regulation and other pathways [61, 62]. The T6SS can also be constituently active where it acts as an offensive mechanism or it can act in retaliation as defensive firing [62–64].

T6SS is a system that is involved in both inter-bacterial competition and host cell attack for virulence as well as other functions such as metal ion uptake [53, 65, 66]. Species can often have multiple systems that employ different roles or switch the role via differential regulation [58]. Through competition the T6SS is involved in a range of inter-bacterial interactions including: the development of host-associated community structure [67], colonisation resistance of pathogen [68], self recognition [69], and horizontal gene transfer [70].

1.3.3.3 CDI and T6SS

Comparing T6SS and CDI, difference in complexity of the machinery can be seen, with T6SS being a multiprotein ‘nanomachine’ whereas CDI utilises two proteins CdiB/CdiA to intoxicate neighbours (Figure 1). The T6SS uses a potent mixture of toxins delivered in unison to cause irreversible damage or cell lysis. With CDI the killing is not as aggressive with overall target population reduction being the main phenotype reported and recovery being possible [71]. Bacteria can have multiple T6SS and CDI systems and both systems are encoded on genomic islands or plasmids [28, 58, 72]. Figure 1 outlines the structures of the two systems and Table 1 summarises their similarities and differences. There has so far been no systematic comparison of the two systems to determine the inhibition differences and if that extends to different affects on spatial structure.

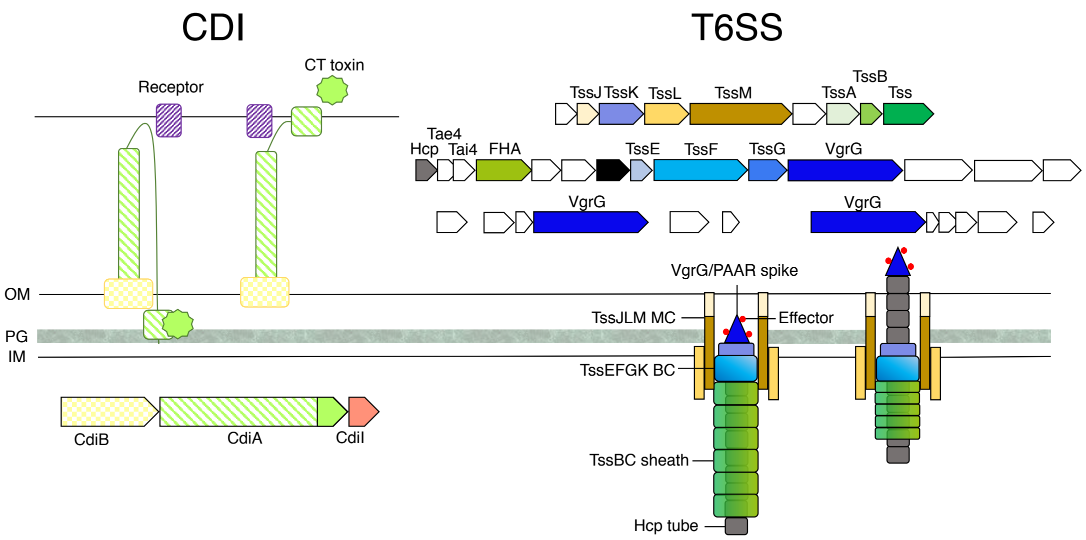

Figure 1: **Genetic and molecular structure of the CDI and T6SS systems.** CDI system structure and mechanism of toxin insertion into the neighbouring cell. Figure constructed based on Ruhe et al. [36]. The T6SS gene cluster organisation is based on the *Enterobacter cloacae* system [73] (the full gene cluster is not included in this diagram). Figure constructed based on Journet and Cascales [73]. Abbreviations used: outer membrane (OM), peptidoglycan (PG), inner membrane (IM), membrane complex (MC), baseplate complex (BC), C-terminal (CT). Gene and proteins are colour coded.

	T6SS	CDI
Inhibition activity	bactericidal, bacteriolytic	bacteriostatic, bactericidal
Toxins	cocktail: amidase, lipase, nuclease, pore forming	single toxin: nuclease, pore forming
Receptor dependent	unknown	yes
Cost	high	low (predicted)
Machinery	'nanomachine' phage tail-like	CdiB/CdiA
Scope of Inhibition	inter-species/intra-species	intra-species/inter-species
Other Attributes	virulence	adhesion, biofilm formation, signaling

Table 1: Comparison of CDI and T6SS attributes.

1.3.3.4 Modelling contact inhibition

Experimental competitions have shown how inhibitor strains carrying active T6SS or CDI systems can outcompete non-toxin producing target strains. To aid in investigation of how these systems affect population structure, mathematical and computational models have been developed to help give greater insight into the ecological effects of contact inhibition.

Blanchard et al. [74] were the first to directly model contact inhibition. They deterministically modelled the system using coupled ordinary differential equations using a nearest neighbour term to describe the contact. They carried out a systematic assessment varying cost, inhibition rate and diffusion parameters in both well mixed and spatial cases (primarily in 1D but confirmed in results in 2D). Their main conclusions were that extinction of either species would occur in the well mixed case, dependent on initial conditions and cost/inhibition parameter. However, in the spatial case coexistence and local patterning can occur, dependent on initial conditions, cost, inhibition rate and diffusion. This fits with models and experimental work for the effect of diffusible toxins [25, 26].

The model by Blanchard et al. [74] presents the basics of the spatial effect of contact inhibition defined by the interplay between growth cost and inhibition. Inhibition is modelled as killing and removal of target cells, which has so far not been reported with CDI. Therefore, their work is closer to modelling T6SS inhibition or generic contact inhibition. There was no experimental evidence to suggest high cost of CDI, at the time of the study by Blanchard et al. [74]. Recently Bottery et al. [1] measured an approximately 3-5% cost in CDI systems in two *E. coli* strains. Other toxin systems also show a production cost. Therefore, the cost assumption by [74] is of interest, but the values they used may not be accurate. Due to heterogeneity being seen at the single cell level [1, 75], stochastic modelling would be a more appropriate to model the cell-cell interactions of contact inhibition, than the deterministic model used here [74].

Subsequent models of contact inhibition have used individual based approaches, allowing for stochasticity to be included and emergence of structure. Borenstein et al. [76] use an individual based model (IBM) to look at the role of T6SS in population structure. In a lattice based model they vary inhibition rate and initial fractions of target cells in range expansion (population growth). They concluded that with a sufficiently large starting population targets cells can withstand attack, calculating the minimum target population needed to expand. They also show domain size is dependent on the starting density in simulations with experimental comparisons. This explains how stability and coexistence is achieved when competing with contact dependent toxin systems. However, a model using experimental values to parmeterise inhibition and cost would give a more robust understanding of what happens in natural populations.

Wong et al. [77] look at the population effects of T6SS interactions firstly experimentally using mutual attack of two species, *Vibreo cholera* and *Aeromonas hydrophila*. They show that with mutual attack coexistence occurs which is dependent on having a viable toxin system for protection. They show T6SS leads to herd protection by killing lone cells and creating a border and interface between cell types to allow clonal expansion of larger clusters. This corroborates the conclusion from Borenstein et al. [76], that small populations collapse and larger domains expand. They also show experimentally that T6SS can protect cheats (strains that don't kill but have immunity). Wong et al. [77] then use simulations in a square lattice to back up their experimental results. They show that through killing of lone cells and cell types segregation coexistence can be maintained. This work is in line with both Blanchard et al. [74] and Borenstein et al. [76] in suggesting that T6SS is involved in creating spatial segregation but furthers their unilateral models to show that mutual attack can also create stable structures.

Work by McNally et al. [78] also looks at T6SS using agent based, partial differential equation and Ising spin models. They look at a situation where there is not an expanding population (as opposed to Borenstein et al. [76] range expansion) with mutual attack representing T6SS killing systems. With their three models and also in microscopy, they show that T6SS drives population separation, which they term 'phase separation'. This backs up what Borenstein et al. [76] and Wong et al. [77] see in their respective models that inhibition causes segregation. They further investigate if T6SS can aid cooperation. They computationally model competitions with populations of 'cooperators' who supply a public good at a growth cost and 'cheats' that do not produce the public good and have a higher growth rate (with mutual attack between the cooperator and cheat). They find in a structured environment with T6SS induced phase separation, that the cooperators survive instead of being out competed by the faster growing cheats. This leads to the conclusion that T6SS can be used to protect public goods secretion from cheats. They back this up in biology by looking at the abundance of T6SSs and secreted products in proteobacteria and bacteroidetes. They suggest that the correlation between the number of T6SSs and effectors with secreted products could mean contact inhibition aids the evolution of cooperative traits such as secretion of public goods. They accept that this is not conclusive with other possible reasons for the correlation. This comprehensive study uses models to explore the ecological effects of T6SS, including statistical analysis and experimental data to back it up.

Other papers have aimed to explore contact inhibition computationally. Wilmoth et al. [79] aimed to use a high-throughput experimental and simulation workflow to look at spatial structure with contact inhibition but it is not clear that they have added any more information to the field. Xiong et al. [80] wanted to show that antagonism can show stability not just separation. They argued that the other models do not extend for long enough time periods to show stability. In their mathematical model they showed that binary systems with contact inhibition can be stabilised by long range interactions via diffusible products.

The most recent analysis of contact inhibition looked at CDI in microscopy and simulations [1]. Bottery et al. [1] investigated two different CDI toxins in *E. coli*, identifying subtle effects of CDI at the single cell level with different systems showing different inhibition dynamics. They showed that contact with CDI inhibitor cells reduces the number of divisions of target cells compared to control target cells that are not in contact with CDI expressing cells. The growth rate reduction can also be variable between cells. Their single cell measurement does not give the full story of the inhibition dynamics, the inhibition rate could be fast with a weak effect on growth rate of the target cell, or inhibition rate could be slow with a strong effect on the growth rate of the target cell. They went on to show with simulations that subtle inhibition can affect spatial structure in expanding populations and defined rate of inhibition as the dominant parameter. This work gives insight into the subtlety of inhibition with CDI and the potential effect on spatial patterns.

Although the models have been directed at slightly different questions, some commonalities can be seen. One main finding is that competition causes separation of cell types allowing target populations under certain conditions to survive attack. The ecological value of this separation effect has been developed by McNally et al. [78] suggesting that this competition favours cooperation via production of public goods, even though T6SS cheats do still profit [77, 78]. The rate of inhibition is explored in several of the models but these are based on the assumption that attack results in target cell lysis and is therefore implemented as dead cell removal from the simulation. This bacteriolytic implementation is an adequate model of inhibition for certain T6SSs but this is not a universal trait of contact inhibition and is not seen in CDI in the systems explored so far at the single cell level [1, 81].

1.4 Using *Enterobacter cloacae* as a model system

Enterobacter cloacae (ECL) has both the CDI and T6SS systems which therefore made it a good model system to compare the two. In ECL the CDI system does not show inhibitory activity under the laboratory conditions used. A strain was made to induce CDI by integrating the *E. coli* arabinose promotor upstream of the *cdiBAI* gene cluster in ECL [82]. Competing CDI+ inhibitor cells against CDI- targets cells on agar plates, with arabinose induction of CDI, resulted in 20-fold inhibition [82]. Although CDI is often found to be an intra-species competition system, due to receptor specificity ECL can also exhibit inter-species inhibition, specifically it has been shown to inhibit *E. coli* [82, 83]. Therefore, *E. coli* can be used as a target strain for both systems as the T6SS is active against *E. coli* but not ECL. In the T6SS of ECL five effectors have been identified (four of the toxins are of known function) [84], these include: Rhs1 a nuclease, Rhs2 a DNase, Tae4 a class 4 amidase and Tle1 a class 1 lipase [84]. The CDI toxin in ECL is an rRNase [82].

E. cloacae is a clinically relevant bacteria as it is a commensal bacteria in the intestinal tract but can be an opportunistic pathogen when in immuno-compromised patients [85]. Routes of infection can include skin, gastrointestinal tract or urinary tract. Infections can be cause by contamination of surgical equipment or medical devices, and ECL can be a particular problem in neonatal units [86]. What causes ECL to be a significant clinical problem is its resistance to many types of antibiotics [87].

1.5 Hypothesis

Visualisation of T6SS killing at a single cell level has shown that the T6SS in several species cause lysis of target cells [88, 89]. This is in stark contrast to the subtle single cell inhibition seen with CDI, which shows that contact with CDI inhibitor cells reduces the growth rate of target cells so that they divide less than control cells in a given time frame [1]. The difference in inhibition dynamics between T6SS and CDI has so far not been explored at a single cell level nor the relative effects of the differing potency of inhibition on population spatial structure.

As current models of contact inhibition simplify inhibition to a single killing dynamic, exploration of the nuance of inhibition potency based on experimental observations can be used to look at fine spatial interactions caused by contact inhibition. This is relevant in densely packed communities where local interaction define growth and death. This leads to my hypothesis that the extent of inhibition with different contact inhibition systems will change the fine scale spatial structure of microcolony growth.

1.6 Aims

In this thesis I aim to further the understanding of the impact of contact inhibition on spatial structure using an iterative experimental and in silico approach. I want to gain a deeper understanding of the relationship between potency of toxin systems at the single cell level and their fine scale structural effect on microcolonies. Specific aims:

1. Investigate the single cell dynamics of the contact inhibitory systems, T6SS and CDI in *E. cloacae.*
2. Use single cell data to parameterise an IBM of contact inhibition.
3. Validate IBM by comparison with single cell data.
4. Use model and microscopy to look at the affect of contact inhibition on fine scale spatial structure.
5. Develop spatial analysis to quantify spatial patterns in simulated and experimental microcolonies.
6. Experimentally validate trends in spatial structure seen in simulations using strains with reduced inhibition potency.

1.7 Approaches

In the pursuit of investigating spatial structure a modelling approach is often used to explore a wider range of inputs and outputs than are possible experimentally. I would like to argue that this needs to be done in close collaboration with experimental work to base observations on biologically relevant parameters [13].

To model the effect of inhibition on spatial structure a spatial model is needed. This can be done mathematically using partial differential equations but these model populations and do not incorporate phenotypic heterogeneity [90]. Computational models using an individual based approach allow states, behaviours and interactions of individual cells to determine population level outcomes. As seen previously many bespoke model setups have been used to model contact inhibition, predominantly with lattice based models. It has been shown that by moving a model from lattice based to lattice free coexistence is promoted [91]. To look at the fine scale interactions of contact inhibition close alignment with bacterial growth on surfaces would be optimal.

CellModeller [92] is a agent based platform that incorporates bacterial interactions such as growth, cell shape, orientation and pushing. This means that the effect of contact inhibition on spatial patterning can be looked at without lattice confinement. CellModeller has been used to show localised patterning in bacterial colonies and results line up with experimental data [93].

Heterogeneity is seen in microbial clonal populations [94] and single cell analysis of CDI also alludes to this [1]. To understand the differences in T6SS and CDI inhibition dynamics measurements were made in time-lapse microscopy and single cell growth was measured [95]. This allowed the growth of cells to be tracked over time to measure if there is differing growth or inhibition dynamics.

To robustly compare spatial structure statistical analysis of images is vital to pick up small scale changes which is relevant when looking at local interactions such as contact inhibition. Methods of spatial analysis have been developed and used in an ecological context [96] but have not been fully integrated with microbial ecology analysis. In this study two different methods were developed for the specific context of microcolony images in microscopy and simulations. The fractal dimension (Fd) can describe the complexity of a shapes outline and this has been used to show differences in CellModeller simulation images previously [93]. The pair correlation function (pcf) can be used to look at cell aggregation [97] and has been used in individual based models to assess different cell interactions [98, 99].

In summary, the aim was to use time-lapse microscopy to measure single cell growth rates with T6SS and CDI inhibition. These single cell growth rates were used to parameterise and validate an IMB of contact inhibition. The spatial patterns created with differing inhibition potency in both simulation and microscopy microcolony growth were explored and spatial statistics were used to quantify these patterns.

2 Methods

Microbial strains and growth conditions.

Microbial strains were stored at -80°C in Lysogeny Broth (LB) medium with 15% (v/v) glycerol. These stocks were made by streaking an agar plate with a single colony and growing overnight at 37°C in 200 rpm rotating racks. The subsequent lawn was swabbed with a cotton bud to inoculate 1ml of LB/glycerol medium. For each experiment, strains were streaked onto agar plates supplemented with appropriate antibiotics (kanamycin (50 μg/mL) or nalidixic acid (100 μg/mL)) one or two days before use. These plates were incubated at 37°C rotating at 200 rpm overnight then stored at 4°C. ECL plates were not used after more than 4 days stored at 4°C due to sensitivity of the strains, ECL strains showed lack of fitness and reduced viability in microscopy. These growth defects could be prevented by following the above protocol.

To prepare strains for experiments a single colony from a plate was picked using a sterile wooden stick and placed into 3ml LB medium with appropriate antibiotic in a glass test tube. This culture was grown overnight for 16 hours at 37°C rotating at 200 rpm. Overnight cultures were transferred at 1:100 ratio into 3ml fresh LB and grown for approximately 2.5 hours to exponential growth phase (OD_{600} of 0.4-0.8). For competition experiments dilutions were made in fresh LB, both strains were added at a 1:1 ratio and vortexed before pipetting onto agarose pads or agar plates.

For microscopy experiments bacteria were grown on agarose pads made with LB. Agarose pads were cast 16 hours before use and stored at 4°C. Agarose was prepared by adding 2% (w/v) agarose (Eurogentec) in LB medium and microwaving until fully melted (20% (w/v) arabinose at 1:100 or SYTOX Blue (Invitrogen) at 5mM were added after melting if necessary). 600μl of agarose was pipetted into a 25μl Gene Frame (Thermo Fisher Scientific) attached to a slide. A cover slip was immediately placed on the agarose and pressed to seal oround the edge of the Gene Frame. Before use agarose pads were equilibrated to 37°C in an incubator for 1-2 hours.

Population competitions.

Population competitions with ECL (LPS O-antigen serotype not known) and *E. coli* (LPS O-antigen negative) were carried out according to the method used by Beck et al. [82]. Overnight cultures were diluted to 1:50 in 50 ml LB with appropriate antibiotic and grown for 2 hours until mid log phase (OD600 0.4-0.6) in baffle flasks shaking at 200 rpm at 37°C. Cultures were spun down at 3100 x *g* for 8 minutes at 4°C then media was removed. The pellets were resuspended in 500μl 1X M9 salts and transferred to a micro-centrifuge tube. The OD_{600} of a 1:10 dilution was measured in order to calculate a total concentration of an OD_{600} of 17 per competition. Inhibitor and target cell were made up to an OD_{600} of 17 and mixed at a 1:1 ratio using 1X M9 salts to give a final volume of 100 μl per competition. 100 μl of mixed culture was spread onto pre-warmed agar plates using glass beads (number of beads used was consistent throughout the experiment). Plates were incubated at 37°C for 4 hours. To count the colony forming units at the start of the experiment, 100 μl of competition mixture was added to 900 μl 1X M9 salts and diluted to $1x10^{-8}$ and 100μl put onto antibiotic selection plates for each strain. After 4 hours competitions were resuspended in 1.5ml 1X M9 using a spreader to scrape off the bacterial lawn. Dilutions up to $1x10^{-8}$ were made and plated as before. Plates were incubated at 37°C and counted the next day. To calculate competitive index (CI) the start and end CFU are calculated from counts: start CFU = dilution * count/volume (100 μl) and end CFU = 1.5(dilution * count/volume (100 μ)). End CFU is multiplied by 1.5 because of the volume used to resuspend cells. CI is then calculated as $\log[(I_{start}/T_{start})/(I_{end}/T_{end})]$.

Phase contrast microscopy.

A Zeiss LSM 510 META microscope with AxioCam HRm camera was set up with a large incubation chamber and heated to 37°C at least 16 hours before the start of the experiment to allow for thermal equilibrium of all components including the lens oil. The Köhler illumination of the scope was corrected before the start of the experiment to allow for accurate phase images. 63x phase oil objective was used. Samples were prepared on agarose pads as described in the microbial strains and growth conditions section. 1 μl of competition mixture was pipetted onto agarose pad squares and left to air dry next to the flame before covering with a cover slip. Slides were transferred to the microscope room using a heat box made with tubes containing warm water placed below the slides to avoid thermal shock. AxioVision was used to mark and find positions and run experimental time-lapses. Auto focus was used on the brightfield (PC) field. Brightfield was set to 100 ms, GFP to 300 ms (GFP filter) and SYTOX Blue to 100ms (CFP filter). 50% power of the X-Cite 120 mercury lamp was used (Excelitas technologies). The time-lapse was started 30 minutes after competitions were fixed onto slides. The time-lapse was run every 6 minutes for 4 hours. Autofocus only corrects up to 3 nm out of focus so manual refocus needed to be carried out several times through the acquisition due to drift. Files were saved in .zvi format and concatenated and converted to TIFF in ImageJ.

Single cell analysis.

Single cell analysis of images acquired in phase contrast microscopy was carried out in ImageJ (version 1.52a) [100]. To count cell divisions the cell counting plugin was used as follows: with target-inhibitor cell interactions present in the first frame of the time-lapse, target cells in contact with inhibitor cells were marked at each division to track the number of divisions achieved in 240 minutes of growth (40 frames with 6 minute intervals). Target cells were unmarked if they lost contact with inhibitor cells. The frequency of cells for each number of divisions were counted in the final frame (frame 40). For division analysis with SYTOX Blue target cells that made contact with inhibitor cells at any point in the 240 minute time-lapse were marked and number of divisions counted until SYTOX Blue was taken up into the cell. Division count data was manually input in to .csv files and plotted in R (version 4.0.0).

For cell length tracking, cell lengths were measured using the inbuilt measure function in ImageJ. Cells of interest (with less than 5 divisions and some with 5 divisions and more) were chosen from division analysis. Starting from frame 40 working backwards to frame 1, the lengths of these cells were measured in every frame. Measurements exported to .csv file were manually marked for cell number and lineage to be able to plot length/time.

To measure the killing time the counter tool in ImageJ was used. Target cells that made contact with inhibitor cells at any point in the 240 minute time-lapse were marked and number of frames until SYTOX Blue uptake was counted. Killing time analysis was carried out at the same time as division counts. SYTOX Blue uptake without contact was counted by recording at which frame any cell not in contact (target or inhibitor) took up SYTOX Blue.

Confocal microscopy.

A Zeiss 870 Multiphoton microscope was used for confocal imaging. The heat box was turned on and heated to 37°C at least 16 hours before the experiment to allow thermal equilibrium of all components. A 63x water lens was used. Zeiss Zen 2010 software was used to run experiments. An argon laser was used for 488nm GFP excitation. Cultures and slides were set up following the same methods as in phase contrast microscopy. Images were taken at the start of the experiment (T = 0) then once every hour for 4 hours. At the 4 hour end point, more images were taken of areas where cells fill the entire field of view. Image analysis was carried out in ImageJ (see fractal dimension method below).

Simulations.

Simulations were carried out using the CellModeller software [92]. The Gibson-Bruck algorithm developed by Bottery et al. [1] was used in CellModeller to add stochasticity to the inhibition reactions. This algorithm adds stochasticity to the reactions by calculating a reaction propensity based on inhibition rate which is then initiated though a priority queue.

Simulations to be compared to single cell microscopy data were set up as follows: 30 cells of each type were placed in a 300x300 μm area. To create a situation of contact from the start of the time-lapse, to have equivalent analysis to microscopy, one target cell and one inhibitor cell were placed in the same location. A counter in the simulation was used to verify that cells were in contact for 240 timesteps (equivalent to minutes in microscopy). This density of cells and area were chosen to gain many cell contacts in one simulation, with space for cells to expand as achieved in single cell microscopy. This allowed one experiment to be run for each parameter set.

Simulations to be compared to microcolony growth were set up as follows: cell seeding distribution was used from counting start cell number in microscopy. The mean cell counts equalled 46 with a standard deviation (SD) of 13. Values were picked from a normal distribution using the Python random number generator function: numpy.random.normal(46, 13). An area of 135x135 μm was used as equivalent to confocal image field size. 10 - 30 repeats of each experiment were used.

For both single cell simulations and microcolony simulations additional parameters used were as follows: base growth rate = 1.06 h^{-1}, intoxicated growth rate of target cells = 0-1.06 h^{-1}, contact rate = 100 h^{-1} $cell^{-1}$, inhibition rate = 0.001-10 h^{-1} $cell^{-1}$. Contact and inhibition rates were used in the Gibson-Bruck algorithm to create stochastic outcomes.

Fractal dimension analysis.

For spatial analysis using the fractal dimensions (Fd), images were converted to black and white in ImageJ. Macro's were written to convert either microscopy or simulation images to binary. Black was used for inhibitor cells and white for target cells. Methods differ slightly for simulation and microscopy image processing. For simulations images were imported using Bio-Formats importer. The Gaussian blur was set with sigma = 12, this is to remove features caused by gaps between cell. Make binary was then ran with a manual check to ensure target = white and the final binary images were saved as TIFF. For microscopy .lsm images were imported via Bio-Formats importer. The image was spilt into separate channels and the GFP channel was used for binarization. This method assumes that the field of view is fully confluent with cells so any space not filled by GFP expressing target cells contains inhibitor cells. Brightness and contrast was manually adjusted to be just before full saturation of the image. This was to adjust for variation in GFP brightness in images. A Gaussian blur of sigma = 5 was set and then made binary with a manual check for targets being white. Images were saved as TIFF. The Fd was calculated using a python script written by Bottery [101] (method development discussed in Chapter 4. The data was plotted in R.

Pair correlation function analysis.

Pair correlation analysis was carried out on simulations. This is a spatial statistical method to gain information on the distance between cell types by measuring all pairwise distance of all cell positions and plotting these correlations to give information on how the particles are packed together. Annuli of radius r are drawn round a focal point and the number of particles of each type were counted, in this context that would be target and inhibitor cells. The radius is increased incrementally and the process repeated. The number of particles is divided by the value given for random distribution to give a value on 1 if random distribution of particles is seen. $<$ 1 would mean particles are further away than random distribution and $>$ 1 would show particles are closer than random distribution [102]. Cell position data was gathered from the CellModeller data in the default .pickle file and output to .csv using a Python script. The spatstat package in R [103] was used to calculate and plot the pair correlation function. Firstly the position data was converted into a point pattern using the spatstat command ppp. Alltypes summary function was used to return an array of the summary statistic ‘k’. The pcf function was then carried out which returns a matrix of correlations for each pair of interactions (target:target, target:inhibitor, inhibitor:inhibitor). Pcf correlations were averaged for 100 simulation images with the 95% confidence interval plotted. Data manipulation, statistics and plotting were carried out in R.

Reagent and resource	**Source**	**Extra information**
Bacterial strains		
Escherichia coli K12 MG1655 attB::kan-gfp	Labratory collection	Lab identifier: MV1463
Escherichia coli K12 MG1655 attB::kan-gfp Nal^{R}	This study	Lab identifier: MV1743
Enterobacter cloacae ATCC 13047	Low and Hayes Labs, UBSC	Lab identifier: Pathogen 962
Enterobacter cloacae ΔVask1::kan	Low and Hayes Labs, UBSC	Lab identifier: Pathogen 985
Enterobacter cloacae spec::araC^{Eco}::cdiB ΔaraBAD ΔVask1::kan	Low and Hayes Labs, UBSC	Lab identifier: Pathogen 984
Enterobacter cloacae Δrhs1 rhs2 1161stop::kan ΔVask1::kan	Low and Hayes Labs, UBSC	Lab identifier: Pathogen 1066
Enterobacter cloacae Δrhs2 rhs1 1323stop::kan ΔVask1::kan	Low and Hayes Labs, UBSC	Lab identifier: Pathogen 1067
Enterobacter cloacae Δrhs2 rhs1 1330stop::kan ΔVask1::kan	Low and Hayes Labs, UBSC	Lab identifier: Pathogen 1047
Chemicals and reagents		
L-arabinose	Sigma	Catalogue number: A3256-100G
Agarose, molecular grade	Eurogentec	Catalogue number: EP-0010-05
Kanamycin	Sigma	Catalogue number: K1876-5G
Nalidixic acid	Sigma	Catalogue number: N8878-5G
SYTOX Blue	Invitrogen	Catalogue number: S1134
LB Broth Lennox	Fisher Scientific Ltd.	Catalogue number: BP1427-2
Gene Frames 65 μl	Fisher Scientific	Catalogue number: 11570294
Software and algorithms		
Python 2.7.16	Python Software Foundation	https://www.python.org/
R 3.5.2	The R Foundation	https://www.r-project.org/
ImageJ 1.52a	LOCI, University of Wisconsin	https://imagej.net/
CellModeller4	CellModeller Software	https://haseloflab.github.io/CellModeller/
Gibson-Bruck implimentation in CellModeller	Bottery et al. [1]	https://github.com/mbottery/CDI_cellmodeller

Table 2: Reagents and resources table.

3 Single Cell Microscopy for Model Parameterisation

3.1 Introduction

The standard way of assessing bacterial interactions such as competition is through population competitions. This is true for many published studies assessing inhibitory activity of CDI and T6SS, through competition assays that quantify the reduction of growth of a target strain by an inhibitor strain in liquid or on solid surfaces [67, 70, 83, 104]. These studies look at the colony forming units at the start and end of a competition which shows that one strain out competes the other but there is no detail on how individual cells are inhibited. A drawback of population studies is that they average out heterogeneity and phenotypic variation [95]. Heterogeneity and phenotypic variation have been shown to occur in isogenic populations (populations of genetically identical cells) using single cell analysis [94]. I therefore think that it is important to look at contact inhibition at a single cell level to be able to more accurately model the systems and ultimately gain insight into their population level functions.

Some single cell studies of CDI and T6SS have been carried out which indicate the two systems demonstrate different inhibition dynamics [1, 88, 89]. However, there is no direct T6SS and CDI comparison and comparing between studies is difficult as different setups and measurements are used. The main factor indicating that T6SS has a higher inhibition potency than CDI is that T6SS causes lysis of target cells but CDI does not [1, 88].

Single cell analysis of CDI by Bottery et al. [1] shows that there is a subtle effect of CDI inhibition in *E.coli* systems. Target cell growth is reduced in individual cells, but ubiquitous growth inhibition is not seen. T6SS has also been looked at with single cell microscopy, with both LeRoux et al. [88] and Brunet et al. [89] use lysing target cells as a readout for T6SS inhibition. LeRoux et al. [88] calculate efficiency of the system by calculating a population lysis rate of 5.5% h^{-1} for *Pseudomonas aeruginosa* attack of *Burkholderia thailandensis* and 0.44% h^{-1} for *P. aeruginosa* attack of *Salmonella enterica*. This rate uses single cell data, however it then averages it out to a population level value without looking at individual cell variability. They also measure the lysis events over time but these are cumulative results which do not show the time from contact to inhibition and how this measurement is distributed over the population. Brunet et al. [89] also measure accumulated cell lysis over time in competition with enteroaggregative *E. coli* attacking non-pathogenic *E. coli* strain W3110 with T6SS. Their results show 30% of the population is killed in four hours with a 10:1 inhibitor:target ratio. This again does not give details about single cell heterogeneity.

The aim in this chapter is to directly compare T6SS and CDI inhibition at a single cell level in order to characterise single cell variability within and between the two systems. *E. cloacae* is a perfect candidate as it contains both T6SS and CDI, which both inhibit *E. coli* [82] and neither system has so far been investigated at a single cell level. A number of facets of inhibition were analysed with single cell time-lapse microscopy, such as the extent to which target cells are inhibited: for example, whether cells stop growing completely or just reduce growth rate. The speed at which inhibition occurs can also be measured. From simulation results Bottery et al. [1] suggest speed is a dominant parameter that affects population structure. From single cell measurements the aim, in further chapters, was to parameterise simulations with the aim of understanding how changes in attributes of inhibition over a wide range of parameters can affect spatial structure.

3.2 Results

3.2.1 Population competitions validate T6SS and CDI inhibition with *E. cloacae*

E. cloacae carries both a T6SS and CDI system. Beck et al. [82] show the CDI system is not active under laboratory conditions, the specific condition of when the CDI system in ECL is active is not currently known. Using an inducible arabinose promotor upstream of the *cdi* operon Beck et al. [82] show that the CDI system can inhibit both ECL and *E. coli.* The strains used by Beck et al. [82] were obtained from the Low lab (see strain list in Chapter 2). Using these strains population competitions on plates, as described by Beck et al. [82] were carried out to confirm inhibition is taking place.

Population competitions can be carried out in liquid culture or on plates [83]. For ECL competitions Beck et al. [82] carried out competitions on plates so this was continued in this study. For all competitions *E. coli* MG1655 attB::gfp is used as a target strain (GFP strain is used as this was used for microscopy). Inhibitor strains made by Beck et al. [82] were used as follows: T6SS+: ECL wild-type (WT). WT can be used for T6SS as CDI is not functional in WT cells under laboratory conditions [82]. T6SS- control: ECL Δ*vask1.* Vask1 is an essential structural component of the T6SS and its deletion disrupts T6SS function [105]. CDI+: ECL araC$^{\mathrm{Eco}}$::cdiB Δ*araBAD* Δ*vask1.* The araC promotor from *E. coli* was placed upstream of the *E. cloacae cdi* locus to be able to induce the *cdi* genes with arabinose and the T6SS function was deleted via Δ*vask1* (*tssM*). CDI- control: ECL araC$^{\mathrm{Eco}}$::cdiB Δ*araBAD* Δ*vask1* not induced with arabinose.

Competitions were carried out on agar plates for four hours (T4) at 37°C, then start and end colony forming units were counted to calculate the competitive index (CI). The CI calculates log of the inhibitor:target ratio at the start (T0) compared to the end (T4). A CI of one shows that there is no difference in start:end ratio and therefore no inhibition. A value higher than one indicates the inhibitor cells outcompete the target cell population. T6SS shows 4-log inhibition, compared to 3-log with CDI (Figure 2). This demonstrates that both T6SS and CDI in ECL can inhibit *E. coli* at a population level.

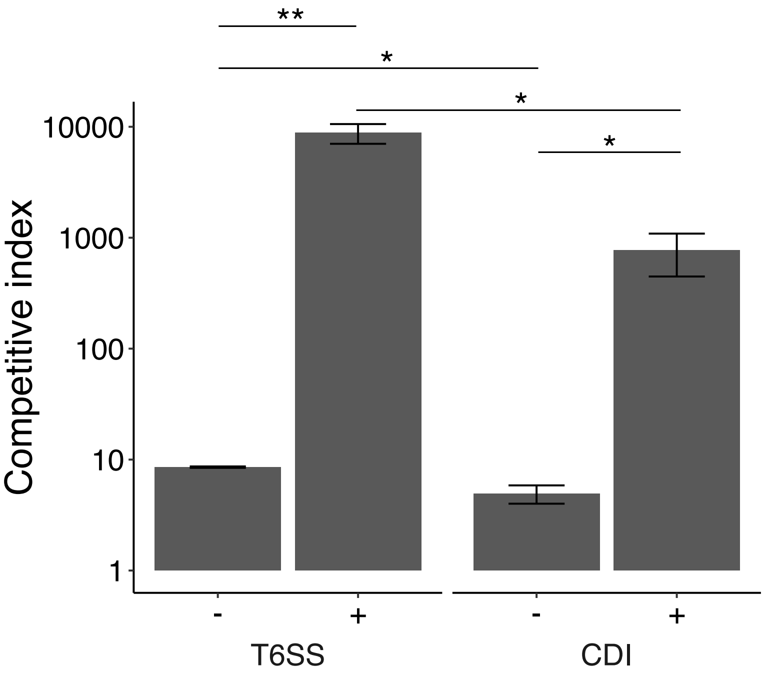

Figure 2: **Population competitions show *E. cloacae* can inhibit *E. coli* MG1655 with both T6SS and CDI.** Inhibition measured using the competitive index which is calculated from viable cell counts from plating on antibiotic selection plates. Competitive index (CI) = log10((Inhibitor$_{T0}$/Target$_{T0}$)/(Inhibitor$_{T4}$/Target$_{T4}$)). Error bars represent +/- SEM of three biological replicates. Significance levels from two-sample t-test **$p < 0.01$, *$p < 0.1$.

3.2.2 Using single cell microscopy to investigate contact-inhibition dynamics

The aim of looking at T6SS and CDI at a single cell level is to understand the dynamics of inhibition. Target and inhibitor strains were mixed at a 1:1 ratio and plated onto agarose pads. To standardise these measurements the following protocol was used: target and inhibitor cells were mixed, vortexed and then immediately spotted on agarose pads. The time-lapse was then started at 30 minutes post plating (T0). Cells were tracked over four hours with images taken at six minute intervals. Target cells were only included in the analysis if they were in contact at T0, meaning they made contact in the 30 minutes before starting the time-lapse (from T-0.5 to T0). Target cells must also maintain contact with inhibitor cells for the four hours of image acquisition to be included in analysis. With the target cells that fulfil these conditions the measurments used to analyse the single cell data include: 1) the number of divisions the cell underwent in the four hour time-lapse and 2) the length of cells over time. In these experiments T6SS+ and CDI+ inhibitor strains were used as outlined for population competitions.

For controls, target cells that do not come into contact with inhibitor cells were used. These target cells were taken from the same experiment (with T6SS+ or CDI + inhibitor cells) but cells were growing in separate colonies not in contact with inhibitor cells (example of target colony analysis for CDI in Figure 3).

3.2.2.1 Investigation of T6SS single cell dynamics

With T6SS there is a clear difference in the number of divisions of target cells in contact and not in contact with inhibitor cells (Figure 4b). More than 80% of target cells in contact with T6SS inhibitor cells do not divide in four hours. This can be seen in Figure 4a where all target cells (green) do not divide. Control target cells, not in contact with T6SS inhibitor cells but present in the same experiment, undergo a range of divisions averaging around seven, with only 5.6% of cells dividing less than five times.

3.2.2.2 Investigation of CDI single cell dynamics

With CDI inhibitor cells the effect on *E. coli* target cells is not as clearly visible as with T6SS. Target cells in sustained contact with inhibitor cells continued to divide and do not obviously stop elongating (Figure 5a). Looking at the number of divisions of target cells in contact with CDI inhibitor cells (Figure 5b) the distribution of cell divisions is similar to the distribution of target cells not in contact with inhibitor cells, with the majority undergoing 5-7 divisions. However, the number of target cells with abnormal growth (less that 5 divisions) is increased

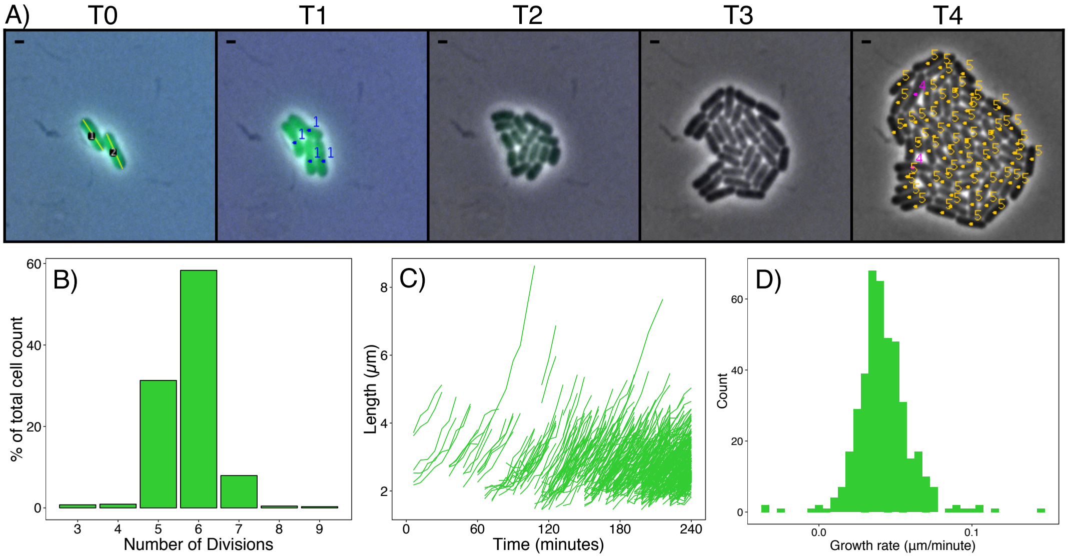

Figure 3: **Image analysis for time-lapse microscopy.** Analysis of control cells in CDI experiment. A) Snapshots of a control target cell colony every hour for four hours (T0-T4). Images were taken at six minute intervals (not all shown). T0 image shows measurement of cell length used for length over time plot (graphs C) and calculating growth rate (graph D). Images T1 and T4 show division counts used for graph B). Scale bars correspond to 1 μm. B) Plotting the number of cell divisions in four hours as a percentage of total cell count. 655 control cells were used for division counts from six colonies. C) Length over time plot to show growth of individual cells. D) Histogram of growth rates calculated from slope of linear regression fit to length over time plot. For growth rate calculations, cells with two or less time points were not included as the linear regression fit would not give an accurate growth rate. 422 cells were used from two colonies. There are more cells included in length analysis than division analysis, as divisions are only counted for cells that reach the end of the time-lapse, whereas length is counted for all cells.

when target cells are in contact with inhibitor cells, from 2% when not in contact to 12% in contact (Figure 5c). This suggests that there is some sporadic inhibition of target cells but the majority of cells do not show obvious growth inhibition.

By examining control cells from T6SS and CDI competitions (Figure 4b and 5b), I decided to define less than five divisions in four hours as abnormal growth. The effect of inhibition with CDI (Figure 5) differs from inhibition with T6SS (Figure 4) by fewer cells showing abnormal

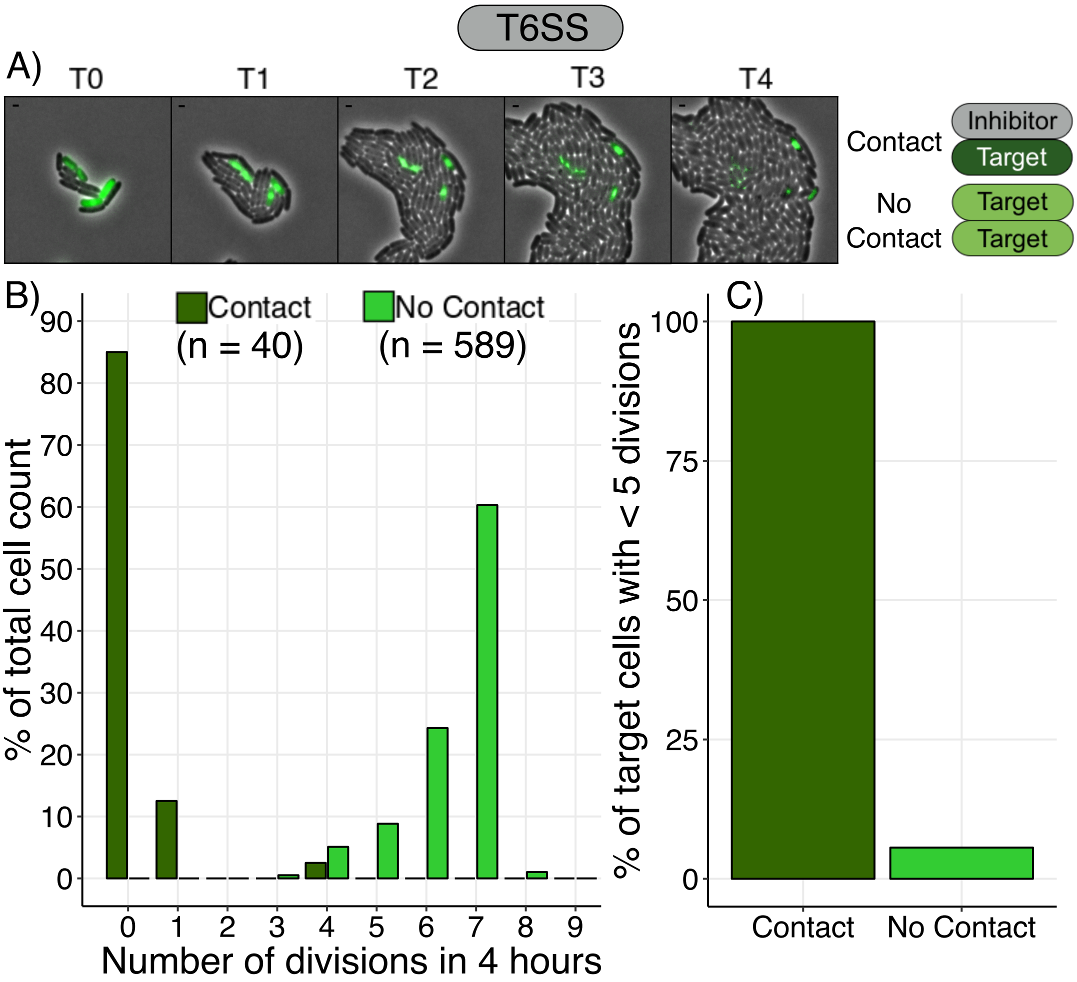

Figure 4: **Quantifying cell divisions with time-lapse microscopy shows potent inhibition with T6SS.** A) Time-lapse images from the start (T0) to four hours (T4) shows target cells (green) do not divide when in contact with T6SS inhibitor cells (grey). All target cells that were measured made contact with inhibitor cells in the 30 minutes from seeding (T-0.5) to the start of imaging (T0) and maintained contact for the four hours of imaging. Scale bars correspond to 1 μm. B) Quantification of target cell divisions with and without contact with T6SS expressing inhibitor cells. The number of divisions for contact or not in contact were plotted as a percentage of the total cells in that group (40 and 589 respectively). The number of target cells in contact with T6SS inhibitors are much lower than not in contact (or CDI in contact in Figure 5) due to the fact that these cells did not divide. C) Percentage of target cells with less than five divisions. This shows the fraction of cells that are considered to have inhibited growth. Data from one biological replicate.

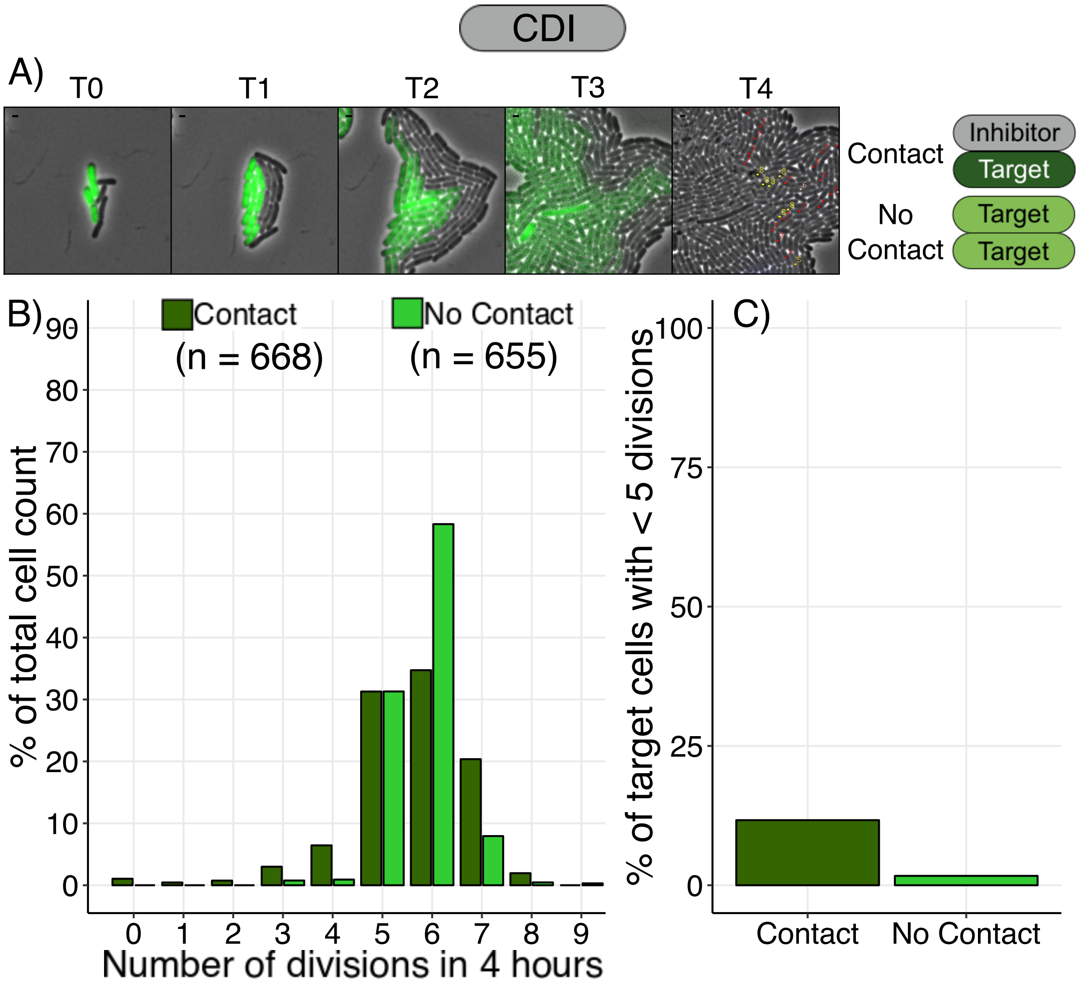

Figure 5: **Quantifying cell divisions with time-lapse microscopy shows subtle inhibition with CDI.** A) Time-lapse images from the start (T0) to four hours (T4) shows growth of target cells (green) when in contact with CDI inhibitor cells (grey). Number of cell divisions is displayed on the T4 image. All target cells that were measured made contact with inhibitor cells in the 30 minutes from seeding (T-0.5) to the start of imaging (T0) and maintained contact for the four hours of imaging. Scale bars correspond to 1 μm. B) Quantification of target cell divisions with and without contact with CDI expressing inhibitor cells. The number of divisions for contact or not in contact were plotted as a percentage of the total cells in that group (668 and 655 respectively). C) Percentage of target cells with less than five divisions. This shows the fraction of cells that are considered to have inhibited growth. Data from one biological replicate.

growth and also the extent of inhibition of the effected cells not being as potent.

To investigate the subtle inhibition seen with CDI further, the length of cells over time was measured. Cells that undergo less than five divisions and a subset of cells that undergo five or more divisions were tracked over time (cells measured with five or more divisions were randomly selected from the same microcolonies where cells underwent less than five divisions).

Looking at the growth of control target cells, which are growing in colonies not in contact with inhibitor cells, clear separation of cell cycles is seen (Figure 6b). All cells are elongating in an exponential manner and the cell lengths are reasonably consistent throughout the time-lapse. A few cells are an exception to this (four cells out of 422) and either grow longer or shorter than the average but these cells still maintain exponential growth.

With CDI there are a range of cell growth dynamics (Figure 6a). There is not a clear segregation of cell cycles as seen with control cells. Some cells do not divide or elongate from the start, whereas some show reduced elongation after three or four divisions. Splitting the data into the microcolony patches (not all target cell lengths of cells in contact were followed in each microcolony, just cells with less than five divisions and a subset of other cells) shows that within the same colony there are heterogenous affects on target cells and between colonies different dynamics are seen (Figure 7).

To describe these different dynamics the effects on target cells can be split into several groups: 1) Fast (within one cell division) and potent inhibition: when target cells do not divide at all and do not elongate. There are six target cells out of 325 cells analysed that do not divided after contact with inhibitor cells (Figure 7, positions 3,4,5,8,14,15). 2) Delayed and potent inhibition: cells that divide one to three times before growth inhibition, some of these cells maintain some elongation but drastically reduced from normal exponential growth (Figure 7, positions 1,2,10,11,12,13). 3) Gradual reduction in growth: cells continue to elongate and divide but at a slower rate (Figure 7, positions 8,9,13,14). 4) Normal exponential growth (Figure 7, some cells in each position).

In Figure 8 cells are split into cells which do not divide before the end of the time-lapse (Figure 8a) and cells which divide before the end of the time-lapse (Figure 8b). Divisions show how many times the mother cell has divided from the start of the time-lapse, showing that there are six cells that come into contact with CDI inhibitor cells and never divide. There are four cells that divide once and six that divide twice. All these cells clearly show inhibited growth by both not dividing and reduced elongation, although some cells do not completely stop elongating. Some cells that do continue to divide also show inhibited growth (Figure 8b) as characterised by cells growing for longer before dividing (visualised by age of cell) and the trajectory of elongation

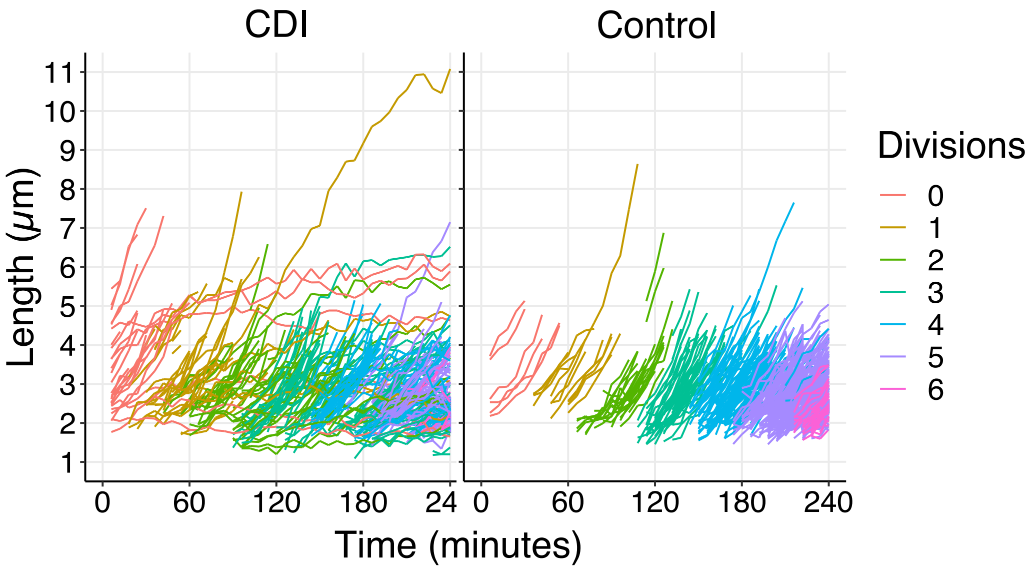

Figure 6: **Tracking target cell length over time shows that contact with CDI inhibitor cells cause a heterogeneous response.** All of the inhibitor-target interactions which have target cells that divided less than five times were included in this analysis. All the cells that divided less than five times were measured, plus a subset of cells that divided five or more times. All target cells were tracked from the start of the time-lapse (T0) for four hours. Only target cells that maintained contact with inhibitor cells throughout the time-lapse were measured. Control cells come from two target cell patches in the same CDI experiment that were not in contact with inhibitor cells. Each line represents the length of one cell over time, coloured by the number of divisions that cell has been through from T0. Data from one biological replicate.

not being exponential.

The growth rate of individual cells can be calculated to show that there is a reduction in rate of cell elongation in inhibited cells. This is calculated by fitting a linear regression line to the length/time plot of each cell with the slope giving the growth rate in μm/minute. In Figure 9 histograms of the growth rates have been split into the same categories as in Figure 8. Target cells in contact with inhibitor cells that divide 0-4 times in four hours (Figure 9a) have lower growth rates compared to both control cells (Figure 9c) and target cells in contact with inhibitor cells that will continue to divide (Figure 9b). Target cells in contact that divide five times also show reduced growth rate suggesting that these cells are also somewhat inhibited (Figure 9. divisions = 5). Target cells in contact that still continue to divide have growth rate distributions trending towards lower values in some plots (9b, divisions = 1 and 2), but overall they are not easily distinguished from the control growth rate distributions (Figure 9c). Plotting all control growth rates and CDI inhibited growth rates together (Figure 10) shows a bimodal distribution with a subset of CDI inhibited target cells that have lower growth rates than control cells.

Results from counting divisions and plotting length/time shows that CDI inhibition is heterogeneic, with some cells being strongly inhibited, others showing different dynamics of less potent inhibition and some not showing inhibited growth in the time period measured. To see if there is a certain interaction needed between target and inhibitor cells to give potent inhibition, the starting images for all contacts where cells divided less than five times and some contacts where cells divided five or more times were looked at (Figure 11). This shows that all target cells that did not divide had sustained lateral contact with inhibitor cells. However, many cells that divided 1-4 times have similar starting contact as well as target cells with more than five divisions. This could suggest that lateral contact is necessary, but not sufficient, to give potent inhibition. There could be several reasons for this including target cells needing hits with multiple toxins to be inhibited or due to localisation of CdiA on the inhibitor cell.

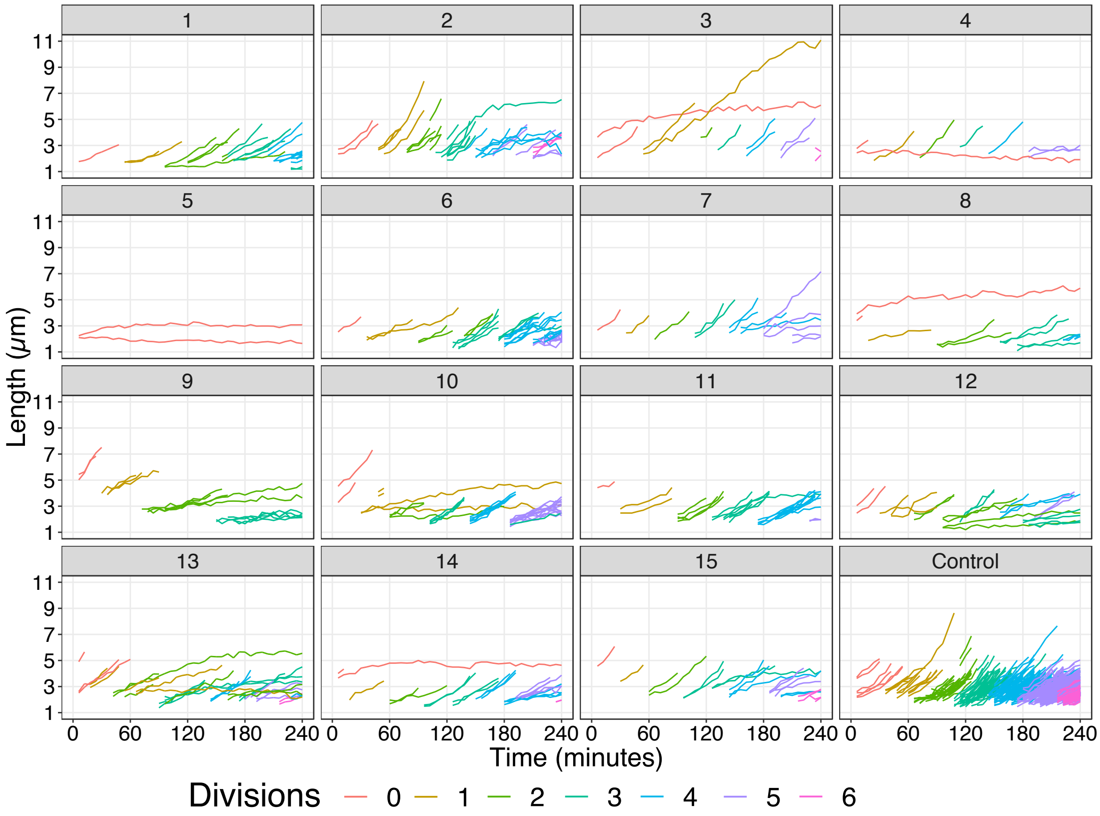

Figure 7: **Tracking length of target cells in contact with CDI inhibitor cells over time shows a range of inhibition dynamics.** Cells represented in this graph are the same as in Figure 6 but split by individual target-inhibitor interactions to show that a heterogeneous response is seen both between and within the same patch of cells. Colour represents number of divisions the cell has been through. Data from one biological replicate.

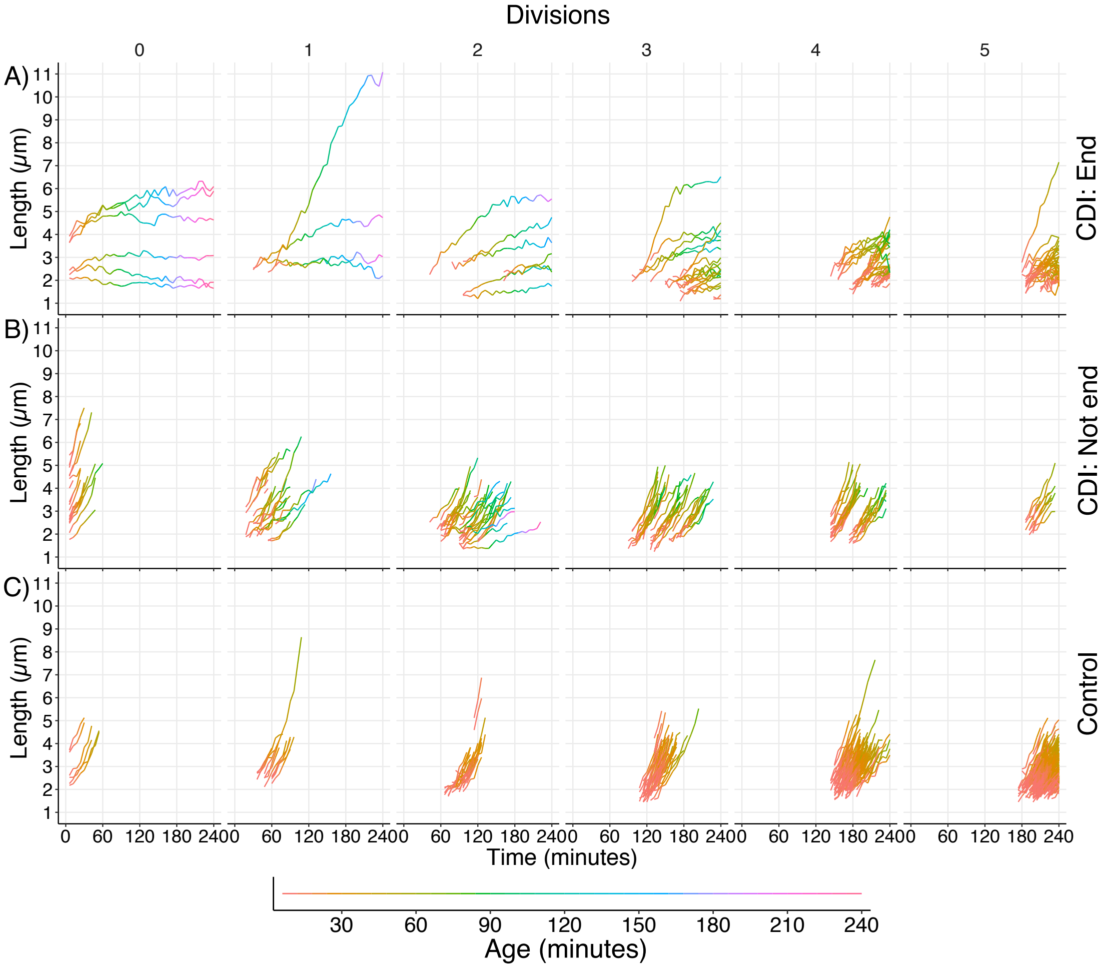

Figure 8: **Splitting cells into categories shows that target cells that continue to divide still show some inhibited growth.** Cells represented in this graph are the same as in Figure 6 but split by cells that do or do not reach the end of the time-lapse. A) Target cells in contact with inhibitor cells that reach the end of the time-lapse without dividing. Cells that divide 6 times have been removed from this figure as they only show a fraction of a cells growth. B) Target cells in contact with inhibitor cells that divide before the end of the time-lapse. C) Control target cells not in contact with inhibitor cells. Cells that divide 6 times are also removed from this graph for the same reason as in section A. Colour represents age of cells in minutes. Data from one biological replicate.

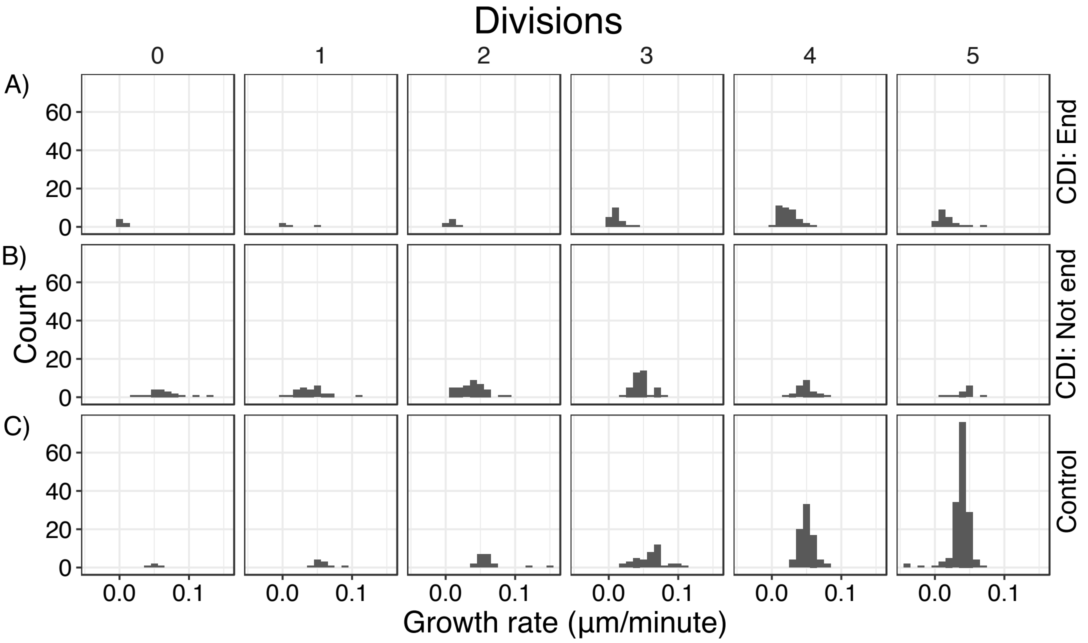

Figure 9: **Reduced growth rate is predominantly seen in target cells that stop dividing when in contact with CDI inhibitor cells.** Growth rate calculated as the slope of the linear regression fit of length/time plot for each cell. The data is split into the same groups as Figure 8. A) Target cells in contact with CDI inhibitor cells that reached the end of the time-lapse. B) Target cells in contact with CDI inhibitor cells that divide before the end of the time-lapse. C) Control target cells not in contact with inhibitor cells. Bins = 0.01 μm/minute. Data from one biological replicate.

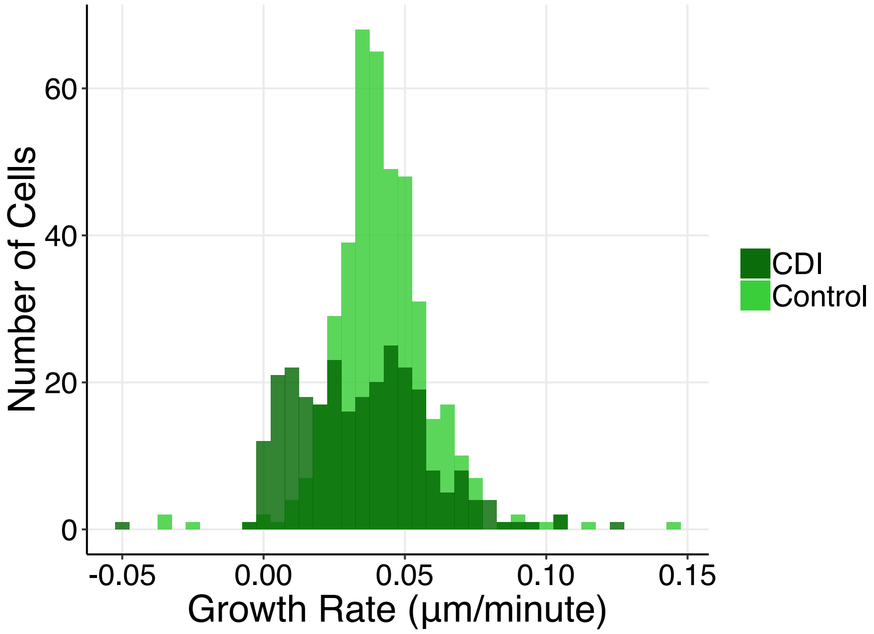

Figure 10: **Growth rate shows bimodal distribution with CDI inhibitor cells compared to control.** Growth rate measured as slope of linear regression fit on all cells presented in Figure 6. Bins = 0.005 μm/minute. Data from one biological replicate.

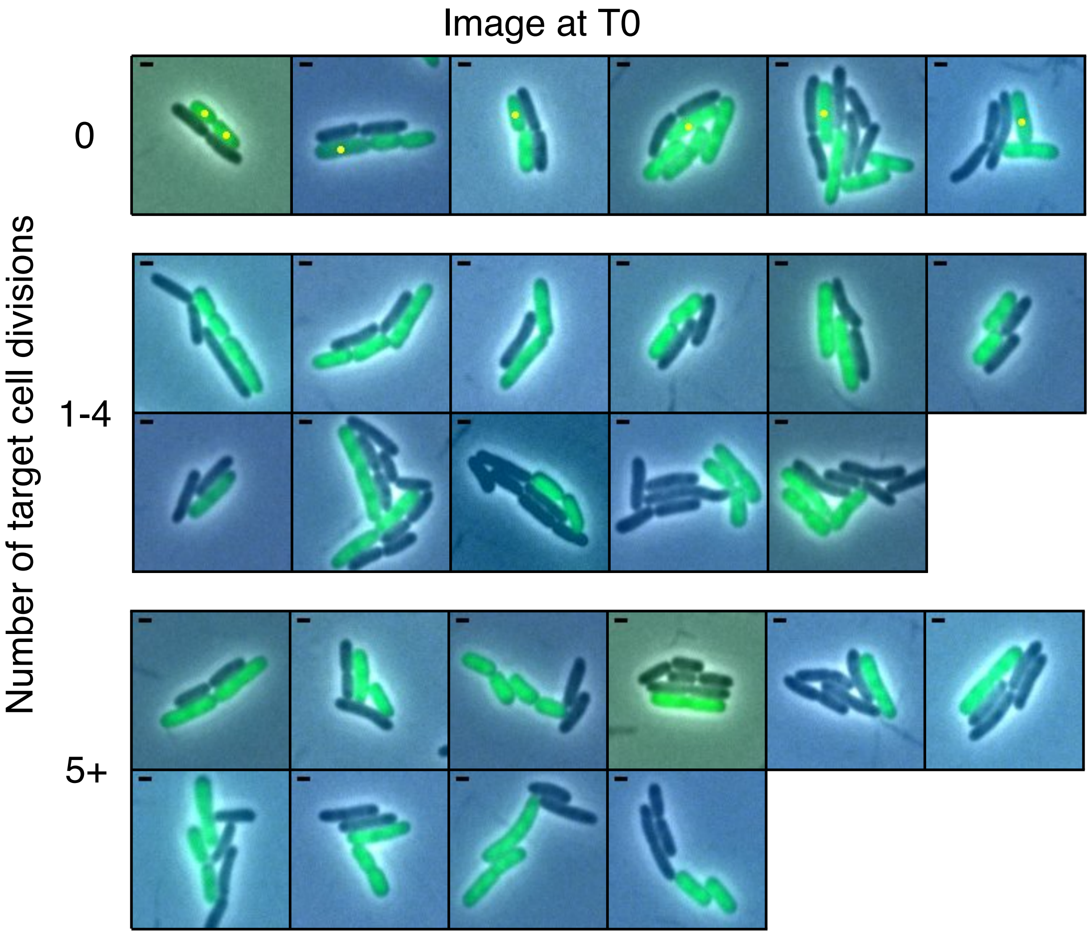

Figure 11: **Start images show there is no clear interaction that defines if a target cell will be inhibited.** Images show the starting configurations (T0) of target cells that have inhibited growth (0-4 divisions in four hours) and some cells that do not (more tha five divisions in four hours). Split into groups of zero divisions (yellow dots show cells that do not divide), 1-4 divisions and more than five divisions. Scale bars correspond to 1 μm.

3.3 Discussion

E. cloacae has both the T6SS and CDI systems making it an ideal model for looking at the differences in inhibition between the two systems. Both T6SS and CDI have previously been looked at the single cell level to some extent [1, 88, 89] but without following the same approach the results cannot easily be compared.

This chapter shows that there are differences in inhibition dynamics between T6SS and CDI. What was shown is that in population competitions fewer target cells survive with T6SS inhibitors than with CDI inhibitors. However, this does not give an understanding of how the target cell population numbers are reduced. Is a higher percentage of cells killed, or are all the cells that are inhibited being inhibited fast so there are less targets to expand the population? Is the CDI inhibition slow but still potent or are all cells being minorly inhibited to reduce growth rate? The single cell data shows that T6SS is a potent killing system with the majority of target cells that come into contact with inhibitor cells divide zero times. The speed of killing has not been directly measured here but as the target cells do not divide it is presumed that the inhibition is within one division (which is approximately 40 minute doubling time for control cells).

This work adds detail to the subtle inhibition seen with CDI by Bottery et al. [1]. They used division counts as a readout for showing reduced growth of target cells. In the two *E. coli* systems they looked at, they saw a subset of target cells with less than 5 divisions, which is what has also been seen with CDI in ECL here. More detail into these cells was looked at with reduced number of divisions by tracking cell length over time. This has shown that target cells have a variety of growth phenotypes that lead to less than 5 divisions in four hours. It can be concluded from this data that CDI inhibition is heterogeneic. Some target cells are inhibited potently and within one division, some take a few divisions to stop growing and some slowly decrease in growth rate.

Heterogeneity is a trait found in isogenic populations to carry out functions such as bet hedging, division of labour and persistence [94]. These are population level strategies that come about through individual cell heterogeneity which can be caused by noisy gene circuits, stochasticity at gene and protein level [106] or stochasticity in metabolic reactions [107]. In this instance the heterogeneity in the target population is formed potentially through a variety of variables in both the inhibitor and target cells, including: the number of toxins present on the surface of the inhibitor cell, the rate of re-establishing the CDI system once fired, the number of target cells in proximity that can be attacked, and the number of receptors on the target cell to recognise CdiA and uptake the toxins. All these possible factors lead to stochasticity of the outcome of competition. This gives good reason to model the system as a stochastic process, not a deterministic one as was done by Blanchard et al. [74] in their model of CDI inhibition. The incorporation of stochasticity in simulations will be discussed in subsequent chapters (Chapter 5).

A method that is used for looking at various single cell affects in microscopy data is cell length tracking. This has been used in bacteria to look at stochasticity of metabolism and growth [107] and to understand single cell growth statistics [108]. Cell tracking is an overall time-consuming process and it has taken some time to establish a viable method that works for our microscopy data. There are many pieces of software developed for tracking bacterial cells in time-lapse microscopy [109–112]. This includes SupperSegger which is a MATLAB-based package that uses machine learning algorithms to calculate cellular boundaries [111], Oufti which has an accessible graphical user interface that includes segmentation, image analysis and post-processing analysis on confluent cell samples [110] and older cell tracking packages such as TLM-tracker [109] and Schnitzcells [112]. Initially some of these cell tracking packages were tested on the time-lapses presented here. The software segments each frame of the time-lapse to identify cells then tracks them over the time-lapse to be able to follow cell lineages. Some drawbacks to the software were found including initial data not being high enough resolution and in focus consistently enough for all frames to be tracked. If one frame was out of focus it could not be used. After optimising the microscopy setup and sample preparation the acquisition improved but the quality was still not good enough for the automatic segmentation to be reliable.

SuperSegger [111] which runs through Matlab was prone to crashing, which could not be easily troubleshooted and fixed. Oufti [110] worked well in that any mistakes made in segmentation could easily be manually fixed but the segmentation was so error prone that most cells in most frames needed to be corrected manually and this was very time consuming. Others have found the same problems with cell growth in dense colonies and sought to develop their own analysis packages for example Balomenos et al. [113]. They claim that this software is able to deal with imperfect resolution and large packed colonies which would indeed solve some of the issues faced, but this software is not yet available.

In the end the method chosen was to manually measure cell length in ImageJ using the measure tool. Cells were then manually tracked and data saved as .csv files and plotted in R. This method gives small errors in length measurements, which can be seen in cells that do not exponentially grow, by fluctuations in length between frames. However, this does not detract from the fit of the regression line and trends can still clearly be seen even with the noise of measurement. Software is continually being developed so it may be possible to use another method in the future.

This chapter has identified remarkably different inhibition dynamics between attack from T6SS and CDI. This has not been previously shown and gives an understanding of the different scales the systems are working in. However, how these different inhibition levels affect population structure, if indeed at all, is still to be seen.

The analysis and data presented in this chapter can describe the inhibition for these discrete examples but putting together a full understanding of the range of inhibition characteristics can be done more effectively using simulations. The growth data from this chapter was used to parameterise simulations with which the output to the discrete situations of T6SS and CDI can be compared as validation. Simulations were then able to explore the parameter space of a wider range of inhibition dynamics. With this iterative approach, the effect of inhibition on spatial structure was then assessed in both simulation and microscopy (Chapter 5).

4 Fractal dimension method development

4.1 Introduction

To be able to compare the structures of bacterial microcolonies, a statistical metric that can be used on both microscopy and simulation images is needed. The features of the binary competitions in both microscopy and simulation are 2D surface growth, with interactions as the two cell types come into contact. Through physical forces such as pushing, and constraints such as space, the borders between cell types become featured [93]. These borders are affected by the interactions between the two species, which in this case is administration of toxins and subsequent growth inhibition. The fractal dimension (Fd) can be used as a statistical index of the complexity of a boundary [114]. Therefore, the Fd can be used to measure the patterns created by inhibtion in binary microcolonies, by giving a value to the features of the border between target and inhibitor strains. Rudge et al. [93] have used the Fd to quantitatively compare images produced in CellModeller simulation and microscopy images.

In this chapter a Fd method that works for the type of images output from simulations and microscopy was developed. There are several ways to calculate the Fd and these were analysed and tested on known fractals and on an example microcolony images. The aim of this analysis was to justify a method that will be used in subsequent chapters (Chapter 5 and Chapter 6) to quantitatively measure the differences in structures created by different levels of contact inhibition.

4.2 Methods

Methods specific to the Fd method development are outlined here. Methods for simulations and microscopy can be found in the main methods chapter (Chapter 2).

Image processing

Pre-processing of both microscopy and simulation images was carried out in ImageJ (version 1.52a). Images were converted to binary to be used for Fd analysis. The difference to the method for image binarization outlined in Chapter 2 was the Gaussian blur values that are used. The Gaussian blur is a filter that performs smoothing using a gaussian function. This smoothing was carried out in order to remove the gaps between cells, which would add unwanted features to the images. The sigma value (standard deviation of the Gaussian) defines the radius of decay. Sigma = 5.0 was used for microscopy images and sigma = 12.0 was used for simulation images.

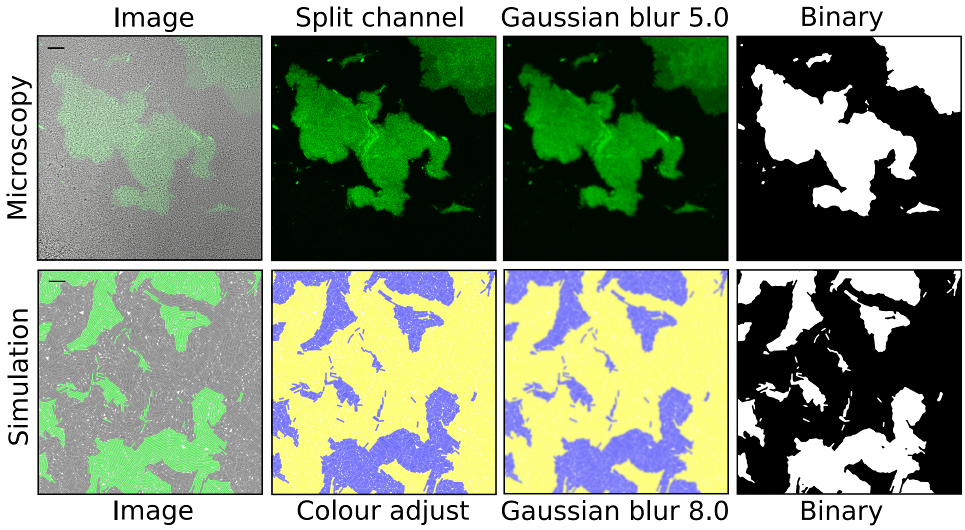

Figure 12: **Conversion of microscopy and simulation images to binary for image analysis.** Top row: For microscopy images the whole field must be confluent with cells, then the fluorescent channel can be used to binarize the image. Brightness/Contrast was used to threshold the image in the fluorescent channel to just before saturation. A Gaussian blur filter was used to remove the individual cell features as this detail adds noise to the black and white image. Bottom row: Simulation images with colours comparable to microscopy images were converted to colours that allowed thresholding. Target cells = green/white, inhibitor cells = grey/black. Scale bars correspond to 10 μm for both microscopy and simulation images.

Figure 12 shows the different processes used for microscopy and simulation images.

ImageJ box-counting tool

Images were converted to binary using the image processing methods above. Images were used as they are, or converted to outlines using the ImageJ outline function (Process>Binary>Outline). Box-counting tool was run in ImageJ (Analyze>Tools>Fractal Box Count). The default box sizes were used.

Python box-counting script

Images were converted to binary using the image processing methods above. The box-counting script was run in Python [101].

Euclidean distance matrix method

Images were converted to binary using the image processing methods above. The ImageJ plugin was used for the Euclidean distance matrix and regression plotted in R (version 4.0.0).

FracLac

Images were converted to binary using the image processing methods above. Binary images were converted to an outline using the outline function in ImageJ. The Fd scan was run through the FracLac GUI in ImageJ. The default parameters were used [115].

4.3 Results

There are several methods and many tools available for calculating the fractal dimension. Rudge et al. [93] used the Euclidean distance matrix (EDM) method described as the boundary fractal analysis with the highest precision and strongest reliability by Bérubé and Jébrak [116]. However the box-counting method is more commonly used and ImageJ includes a built in fractal box-counting tool. The ImageJ tool was tested as the image processing was already done in ImageJ.

Rudge et al. [93] used the Fd to measure the border of a single feature, however, for this data the Fd was calculated on the whole image. Inhibition has an effect on both the intricacy of the border and the quantity of the features in the image. Therefore, it is of interest to measure all the borders in an image as a whole.

4.3.1 Calculating the fractal dimension using ImageJ box-counting tool

To calculate the Fd, the box-counting method works by overlaying the image with a grid of a given box size. The boxes that cover the border between the foreground and background are counted. The box size is then systematically reduced and the count repeated. This is repeated for a range of box sizes. Movement of the initial grid position can affect the count so this can also be iteratively moved. From this the Fd can be defined as the negative coefficient of the linear relationship between box counts and box size (Figure 13).

Images from microscopy and simulations were be used to test Fd methods. These images are similar to the experiments that were used in Chapter 5 to assess inhibition with T6SS and CDI.

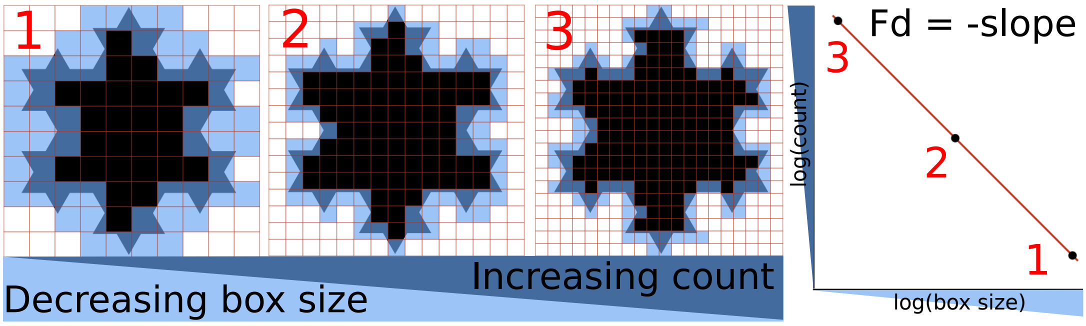

Figure 13: **Schematic of the box-counting method shows the inverse exponential relationship between box size and count.** Progressively smaller boxes are placed over the feature of interest and boxes with the border between background and foreground are counted. The exponential relationship between the box size and the count gives the Fd. This is calculated by plotting ln(size)-ln(count) and fitting a linear regression line. Blue boxes represent the boxes that are counted.

The fractal dimensions calculated using the ImageJ box-counting tool show that with T6SS in microscopy or T6SS-like simulations (high inhibition potency) the Fd is higher than the no inhibition controls (Figure 14d). The increase in Fd with high inhibition potency compared to the control is counter to the hypothesis arrived at by observations of the images. Observations of the images show that in the simulation images with high inhibition potency, the target cells form clusters (Figure 14c), compared to no inhibition control where the target and inhibitor cells are more dispersed (Figure 14a). This is in concordance with the body of evidence from both experiments and simulations that suggest T6SS causes cell type separation [76–78]. This leads to the prediction that with cell type clustering with high inhibition potency, the length of interaction surface between target and inhibitor cells will be reduced. Therefore, this leads to the hypothesis that the Fd with high inhibition potency will be lower than the control (no inhibition). This is counter to what is seen with the Fd calculated using the ImageJ box-counting tool which shows increase in Fd with high inhibition potency compared to the control in both simulations and microscopy images (Figure 14d).

When the foreground and background are switched in the binary images the trend of the Fd is inverted (Figure 15). With the black and white pixels inverted the Fd reduces as the inhibition increases. The box-counting tool does not count if a border is found in each box. It only counts boxes with foreground pixels. This is shown by the simple example in Figure 16. Increasing the area of the black rectangle increases the foreground area but the length of the border between the

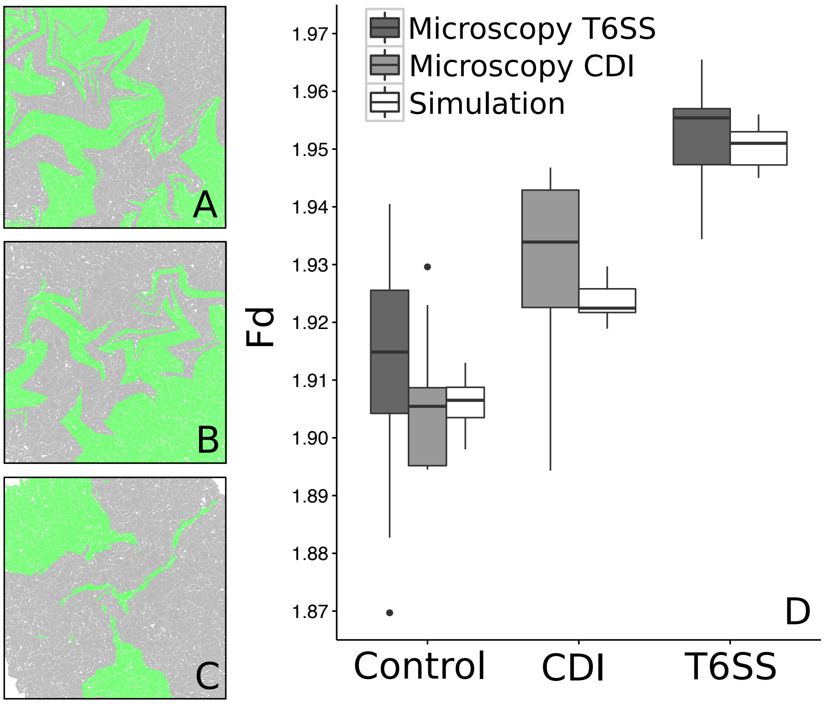

Figure 14: **Quantification of fractal boundaries in simulation and microscopy images using ImageJ box-counting tool shows increase in Fd with increased inhibition.** Simulation examples of: A) control: no inhibition; B) low inhibition potency: CDI-like; C) High inhibition potency: T6SS-like competitions. Target cells = green, inhibitor cells = grey. D) Fractal dimension measurements. Each box plot represents ten independent simulation images.

foreground and background should stay the same. If the Fd of this interaction border is being measured then the Fd would give the same value. However, the fractal dimension increases as the area of the foreground increases (Figure 16). This suggests that the Fd box-counting tool in ImageJ is counting each box that has foreground pixels and giving a Fd that is dependent on the area, not the border.

The ImageJ tool calculates the fractal dimension of the interaction border if used on an image with only an outline of the shape. Using an image with just an outline, the Fd value decreases with inhibition (Figure 17). Converting the binary image to an outline causes some loss of fine information, especially for microscopy images when the images are already hard to accurately threshold due to differences in fluorescent signal. Therefore a custom box-counting script was written in Python to calculate the Fd of the border [101].

4.3.2 Calculating the fractal dimension with a custom box-counting method

This box-counting method counts boxes if they have both black and white pixels in them. With this method the trends of the data are in agreement with the results from using an outline in the ImageJ tool. However, the Fd values are not the same for control images (Figure 17). A reason for this is that the range of box sizes and box positions can affect the Fd value [117] and these differ between methods. A way to mitigate this error is to test the optimal box range for specific images [117] and to sample from a range of starting positions for each box size [115].

4.3.2.1 Justification of the box range used for box-counting script

The variables that can affect the Fd value with the box-counting method include maximum box size, minimum box size and box position. An initial test was carried out to see how changing these parameters effect the Fd, using an example of a simulated control (no inhibition) colony from CellModeller. Box sizes are measured as a length in pixels and therefore the maximum and minimum box sizes are measured as a percentage of one side of the image (Example in Figure 19). The minimum box size was fixed at 3% of the image width as this is greater that the size of one cell. The maximum box size was varied from 5% to 50% of the image width. To reduce the error from the box positions a number of different grid translations were counted and the

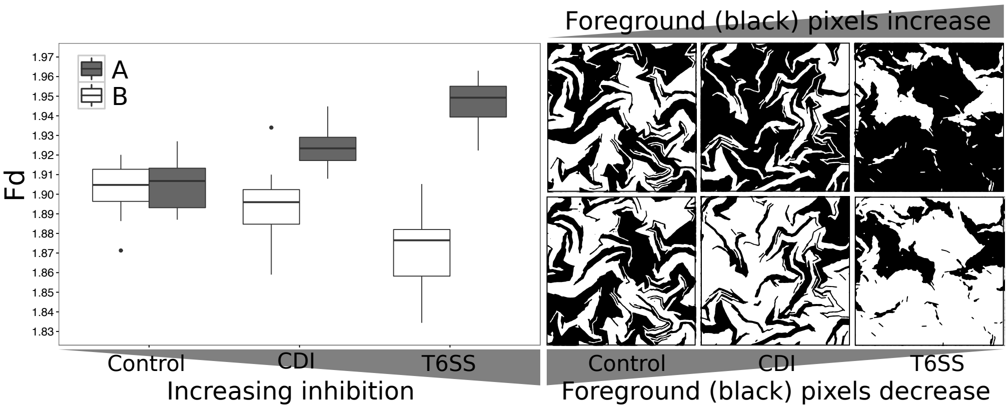

Figure 15: **Inversion of binary images changes the fractal dimension value.** If the inhibitor cells are black and used as foreground pixels the Fd increases as inhibition increases (A: Upper panel and grey bars in graph). If the binary image is inverted so target cells are now black and therefore the foreground, the Fd decreases as inhibition increases (B: Lower panel and white bars in graph).

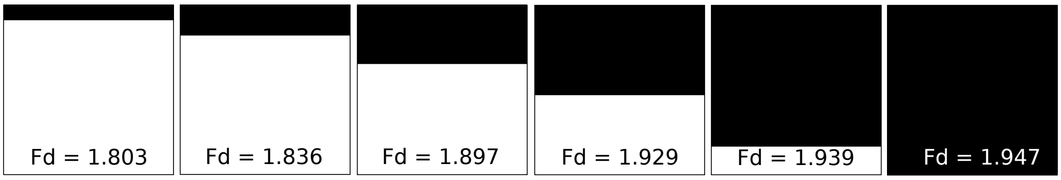

Figure 16: **As foreground (black) area increases the Fd increases.** In these images the black area increases and the white area decreases but the length of the border stays the same. If measuring the border between the two features the Fd should stay the same throughout the images. In these images the Fd increases as the black area increases, this shows that the ImageJ tool is counting the foreground pixels not the interface between foreground and background.

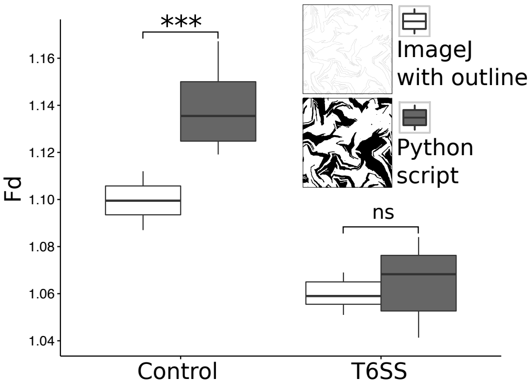

Figure 17: **Two methods that reverse the Fd trend.** A) Using the ImageJ tool with an outline image, the Fd decreases with increased inhibition. B) This trend can be repeated using the custom box-counting script, however the two methods give different values. Each box plot represents ten images. The image used is one example of a control image. Two-way ANOVA; *** = $p < 0.001$, ns = $p > 0.1$

average used to calculate the Fd. The number of starting positions was varied at the same time as maximum box size, from ten to fifty different start positions, in increments of ten. To move the grid start position a random number was generated within the box size for x and y coordinates. As the grid is moved this creates boxes that only partially cover the image. These boxes are still counted otherwise information would be lost. Figure 18a shows that as the max box size increases the Fd increases, suggesting that the Fd is dependent on the maximum box size.

The number of box translations has more of an influence on the Fd when the box range

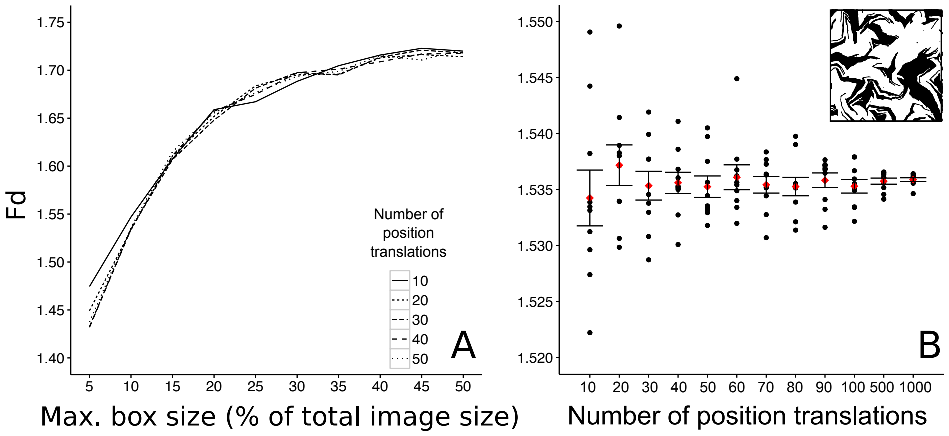

Figure 18: **The Fd is dependent on maximum box size and number of position translations.** A) As the maximum box size increases the Fd increase. Minimum box is fixed at 3% of image length. B) As the number of positions translations increase, the Fd becomes from within a range of 0.03 with ten positions to within a range of 0.003 by 500 translation positions. Minimum box size is 3% of image length, maximum box size is 10% of image length. Data from one control (no inhibition) CellModeller simulation image.

is smaller. This shows that the maximum box size influences the Fd and therefore needs to be optimised. Figure 18b shows that with ten position translations the Fd values are within a range of 0.03, this can be reduced to values within a range of less than 0.005 with 500 position translations. As increasing the number of position translations increases the run time, ten position translations was used whilst finding the minimum and maximum box sizes. This can later be changed dependent on the size of the error seen in images between replicate images.

To find the optimal range of box sizes that are best suited to calculating the Fd of these specific images, the method from Foroutan-pour et al. [117] was followed. To be able to define a method that can justify the range of box sizes to use, the method can be tested on known fractals to see if it can closely estimate the calculated value. This method can then be used on simulation and microscopy images.

For the maximum box size, Foroutan-pour et al. [117] suggest a box size of no larger than 25% of the shortest side as larger box sizes would lead to poor information. They suggest to use the maximum box size where the image covers 85% of the boxes if the structure is noisy or most of the area is covered with features. The microcolony images fit this criteria, so the maximum box size where the image covers 85% of the boxes were found. To find the smallest box size the aim is to find the break point at which the values move away from the linear regression fit. To find this break point, small box sizes were removed incrementally and the fit of the regression line evaluated for fitting the points (Figure 19). As ten positions were used there are several ways to evaluate against these ten points: to take the average, to evaluate within the standard deviation (SD) or to evaluate below the highest value. These three methods were tested using the Koch snowflake.

The maximum box size was found by starting with a box size of 25% of the image width and reducing the size until less than 85% of the boxes are covered by the feature of interest. The minimum box size was evaluated using either: 1) the average, 2) below the highest value or 3) the SD of the ten values collected from position translations. Figure 20 shows that all three methods give a systematic error from the calculated value. The SD was used as it gives on average the closest estimate and the variance covers the known Fd value. The range of values is larger than with the other two methods but only within the range of 0.06. The SD method was used to find the optimal box range for each image.

This method was then used on three other known fractals. Figure 21 shows the Fd prediction compared to the calculated value for the Koch snowfake, Sierpinski triangle, Sierpinski hexagon and the Apollonian gasket. Three other methods are also compared: EDM method and two other box-counting tools (ImageJ and FracLac). All methods show a systematic error from the calculated value, with at most an error of 0.1 from the calculated value. The Python script gives close estimates for three of the four fractals. The main advantage of using the Python script over the other methods is it allows the Fd to be calculated on binary images without converting to an outline.

To check that the accuracy of the Python script is high enough to show differences in simulation and microscopy images, a set of control and T6SS images were tested. These images are similar to the final experiments used in Chapter 5 but the exact parameters are not the same. This test aimed to see if the variation in Fd over repeat runs on the same image is lower than the variation between images of the same group. The accuracy of the Fd using more position translations was compared to the accuracy of the Fd when the average of more repeat Fd calculations of each image was used. Figure 22a shows there is no difference in Fd when the number of position translations are increased from ten to one hundred, or when the script is run ten times on each image and averaged. The range of Fd values for one image from ten repeat runs (with ten position translations) is less than 0.07 (Figure 22b). This error in the method is less than the error seen between ten simulation or microscopy images, which are within a range of

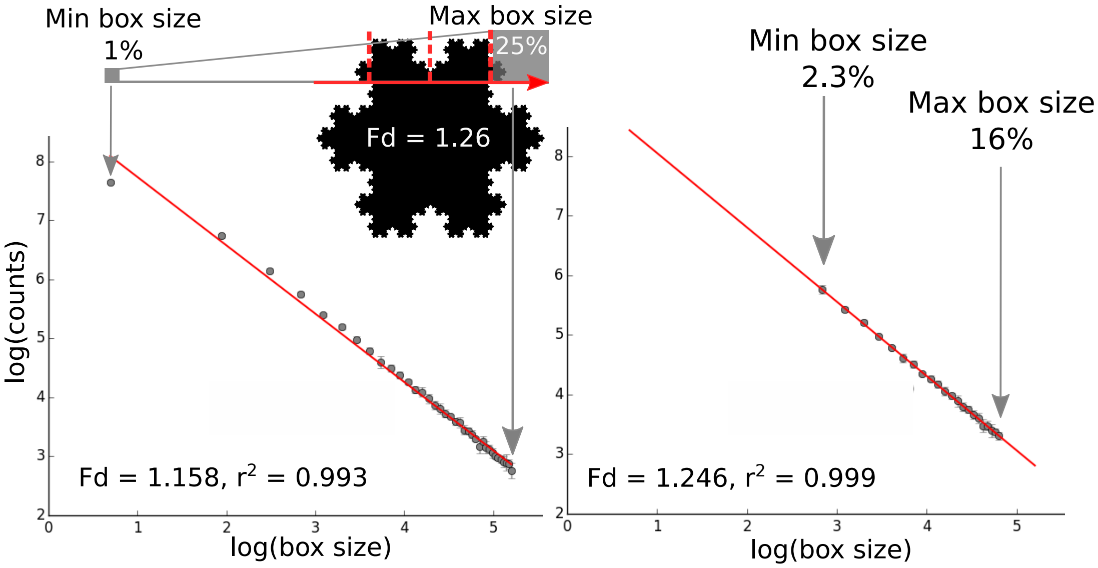

Figure 19: **Method for identifying optimal minimum and maximum box sizes.** Example given on Koch snowflake with a known Fd of 1.26. Minimum and maximum box sizes within the range of 1% to 25% of the length of the image. The maximum box size is found by calculating when less than 85% of boxes are covered by the feature of interest. The minimum box size was subsequently found by removing points until the regression line fits within one SD of average counts. With a minimum box size of 2.3% and maximum box size of 16% the fractal dimension is improved from 1.16 to 1.25. Ten grid position translations were used. The mean and SD were plotted.

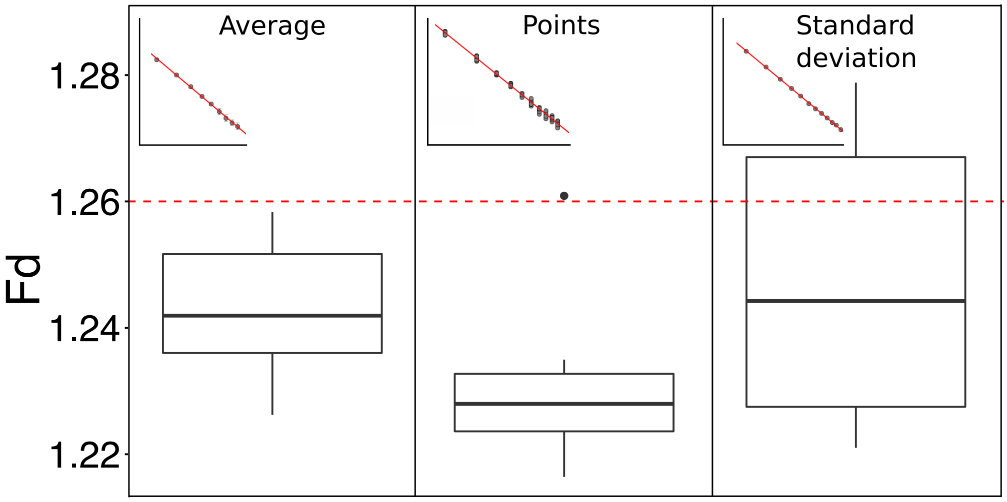

Figure 20: **Different methods for finding the minimum box size by evaluation of regression line fit show a range of Fd values.** Test done on Koch snowflake image. Each box plot represents ten images. Red dashed line shows the calculated Fd value for the Koch snowflake (1.26).

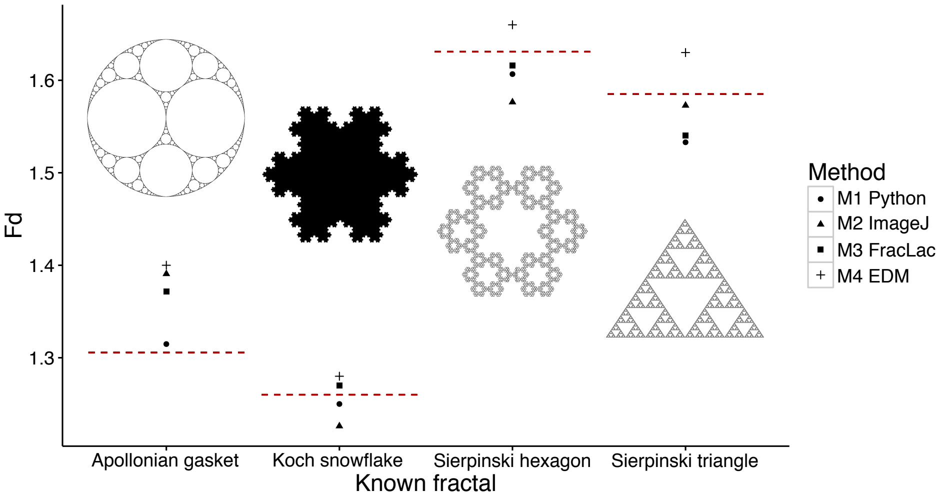

Figure 21: **All Fd methods show systematic error from the calculated value.** Red dashed line represents the calculated value and the points are the values from each method. M1 Python script uses an average of ten runs, M2-M4 use one run each. M1 and M4 use the original shape but for M2 and M3 the image converted to outlines is used.

0.1 to 0.3 (Figure 22c). Therefore although there is variation in Fd values in repeat runs of the script, this is smaller that the differences between images and will therefore not affect the overall results for comparisons between groups.

4.4 Discussion

The aim of this work was to identify a method for comparing the Fd of simulation and microscopy images. After identifying the pitfalls of the ImageJ box-counting tool in regards to the images that were analysed in subsequent chapters (Chapter 5 and Chapter 6), other methods were scrutinised and validated using known fractals and finally example images of the format that this method was subsequently used for. The issue identified with the ImageJ box-counting tool is that it does not make it clear that this method only works on outlines. This does not fit with the aims of a Fd method but can still be used on specific types of images. Figure 21 shows that all Fd methods tested give systematic error from the calculated value, when tested on known fractals. However, as this error applies to all the images it should not affect the comparison between images. The Python script developed for calculating the Fd of binary images gives close estimates for most of the known fractals (Figure 21). This method has a difference in Fd of up

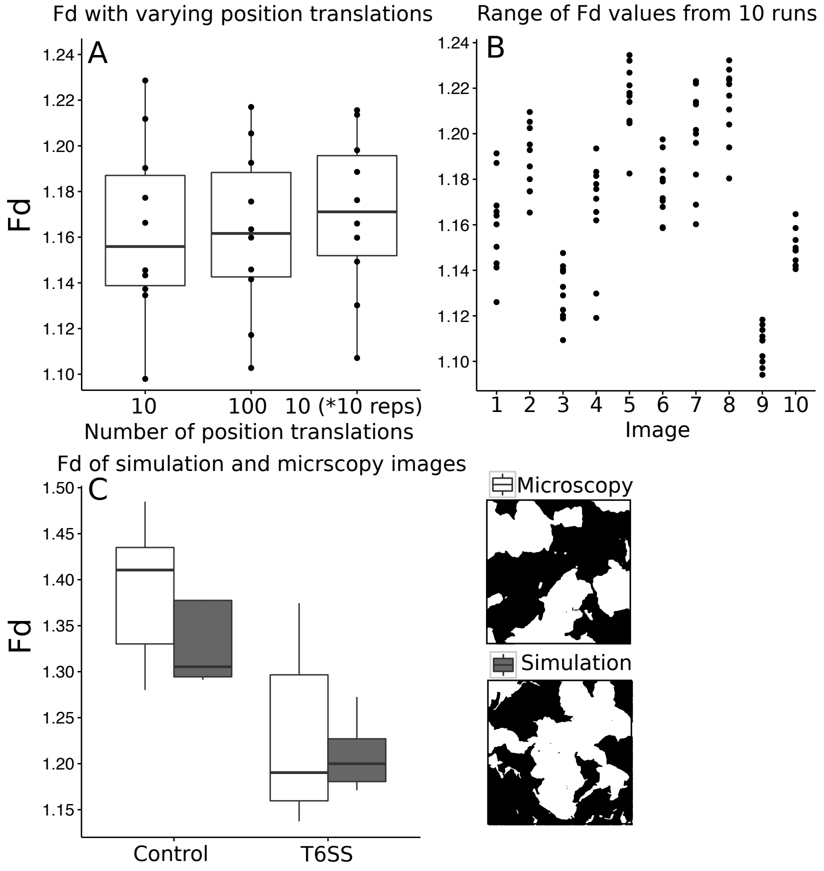

Figure 22: **Simulation and microscopy images show that the accuracy of the box-counting script is higher than the differences in repeat images.** A) Testing different numbers of position translations or averaging ten repeat runs of one image on ten T6SS microscopy images. B) The range of Fd values of the ten repeat runs of ten T6SS microscopy images. C) Fd of simulation and microscopy images for T6SS/T6SS-like and control images. Each box plot represents ten images; ten different field of view from one biological replicate for microscopy and ten independent simulations.

to 0.06 on microscopy images but this difference is less than that seen within repeated images so should not affect the averaged results. The advantage of using the Python script is that it can be used on the black and white images without having to convert to an outline. This will save accuracy especially in microscopy images which are harder to threshold accurately.

5 Modelling contact inhibition

5.1 Introduction

Modelling biological concepts is an increasingly popular way to use the power of computation to gain and interpret data faster and on a larger scale than what is possible experimentally [118]. This approach works best when done in conjunction with experimentation to both accurately parameterise the model according to the biology and to validate the model outputs [13]. This iterative process allows biological processes to be explored that would not be viable with experimentation only [13, 118].

Both mathematical and computational modelling have been used to model biological processes. Mathematical models such as systems of differential equations model deterministic processes which apply at the population level. Limitations of this approach are that they do not incorporate stochasticity and are not spatially explicit, however they can be advantageous for modelling large populations [119]. Computational modelling such as individual based modelling (IBM) uses agents to which attributes and rules can be set. Through adding stochasticity at different scales such as mechanistic detail or at a cellular level, population level outcomes can emerge [118, 120].

Contact inhibition has been computationally modelled previously with Blanchard et al. [74] using a mathematical model to investigate CDI and subsequent models using individual based models to look at T6SS using lattice based simulations (reviewed in more detail in the introduction: Chapter 1) [76–80]. Daly et al. [91] compare lattice based vs lattice free individual based simulations to show that coexistence is more predominantly maintained in lattice free simulations. This is due to spatial heterogeneity allowing spatial refuges to form. As contact inhibition is occurring at the interaction between cell types it would be more appropriate to not impede interaction of cell types by confinement to a lattice.

More recently work from our lab has also looked at CDI using both microscopy and IBM [1]. Bottery et al. [1]. looked at two *E. coli* CDI systems, using simulations to show different spatial patterning in range expansion with different toxins. They show the dominance of the inhibition rate on microcolony patterns through parameter exploriation in simulations. Working in parallel, several of the same methods as Bottery et al. [1] have been used in this study.

The aim of this chapter was to use single cell growth rates from Chapter 3 to parameterise an IBM of contact inhibition. This was then used to both explore the inhibition parameter space and compare results to T6SS and CDI single cell results. In both simulations and microscopy, the effects of different inhibition potencies on spatial structure can be explored using spatial statistics.

When investigating spatial structure it is common to only use visual validation of the differences [74, 77] or simple measures such as quantifying the ratio of target to inhibitor cells [76, 79, 121, 122]. When only looking at cell fractions it may be possible to show clear differences with extreme cases, but to look at a range of patterns and accurately determine differences and trends when using small parameter increments, statistical verification is needed.

Two methods that were used to analyse spatial structure for this data are: the fractal dimension (Fd) and the pair correlation function (pcf). The Fd can be used as a statistical measure of border complexity. As contact inhibition is acting at the border of target and inhibitor cell patches this could be a useful measure to see fine scale changes. The Fd has previously been used to look at CellModeller structures by Rudge et al. [93], showing that cell shape affects spatial fractal patterning. The pair correlation function was also used to look at how the patch formation of cell types is affected by inhibition. The pcf looks at the distance from cell to cell and calculates correlations to show the probability of finding like or not-like cells within a certain radius (See Chapter 2 for details on pcf). This method has been used to look at cell aggregation [97] and in agent based models to asses different cell interactions [98, 99].

5.2 Results

In this section the method for modelling contact inhibition will be defined. Single cell microscopy data from Chapter 3 was used to parameterise and validate the model.

5.2.1 Defining an individual based model for contact inhibition

To computationally model contact inhibition the CellModeller software was used [92]. This software models bacterial growth in 2D or 3D using a GPU architecture to simulate a large number of cells. This software allows you to model bacterial cell growth in a lattice free environment by incorporating biophysical properties of colony growth such as cell growth, division, shape and pushing. Bacterial cells are modelled as rigid capsules that expand exponentially from the poles. Once the cell reaches it's target length it divides to give two daughter cells. Orientations are adjusted to avoid overlap of cells using viscous drag to move cells proportional to the force applied to them [92]. Stochasticity can also be incorporated into the model. Results from single cell microscopy showing heterogeneity in the outcome of inhibition with CDI (Chapter 3) suggest this is an important feature.

To add stochasticity to the inhibition process, the Gibson-Bruck algorithm was used [123]. This method is an event-based scheme which determines when a reaction takes place by randomly selecting values from a probability distribution, leading to stochastic outcomes. The addition of this algorithm to CellModeller was developed by Bottery et al. [1]. This Gibson-Bruck algorithm is based on the Gillespie algorithm, which aims to numerically simulate the evolution of a system using a stochastic formulation [124]. Gillespie suggested two stochastic algorithms that both follow a single trajectory by picking which reaction will take place next, based on random selection from a Markovian exponential distribution. The two methods differ by when they calculate the propensity of a reaction. The Gibson-Bruck algorithm aims to make a more efficient stochastic algorithm using a priority queue [123]. The priority queue is a stacked data structure that uses the propensity of a reaction to determine when it will take place. This structure means only one random number is needed per cycle as the time step is also placed in the queue. In my model the Gibson-Bruck algorithm controls the probability of contact inhibition taking place. Stochasticity was also incorporated in to the model in other places including by randomly varying starting conditions and target volume of cells. The number of cells seeded at the start of the simulation was randomly generated from a normal distribution based on microscopy measurements (Figure 27) and the target volume was randomly generated from a log-normal distribution based on length measurements from microscopy data (Figure 24)

In the model overall inhibition potency was defined by two parameters: inhibition rate (β) and intoxicated growth rate of the inhibited target cell (μ_{Ti}) (Figure 23b). Contact inhibition was added to the model using two reactions: 1) contact, when a target cell came into contact with an inhibitor cell and 2) inhibition, reduction in the growth rate of the target cell that is in contact with an inhibitor cell. Contact was included in order to be used as a marker in analysis for the timescale of inhibition. To validate the model, equivalent analysis to the single cell data were output for comparison. Subsequently images of microcolony growth were then used to investigate the effect of inhibition potency on spatial structure.

5.2.1.1 Model parameterisation from single cell data

To define growth in the model two parameters were involved: 1) the growth rate which defined the expansion of cell volume and 2) the target volume of a cell which defined when a cell divided. To parameterise the growth rate in simulations, division data was used as this was a measure that could be carried out on a large group of cells from single cell microscopy. From microscopy data (Chapter 3), control cell divisions were counted from target cells not in contact with inhibitor cells and inhibitor cells. These are plotted in Figure 24a showing a distribution between three

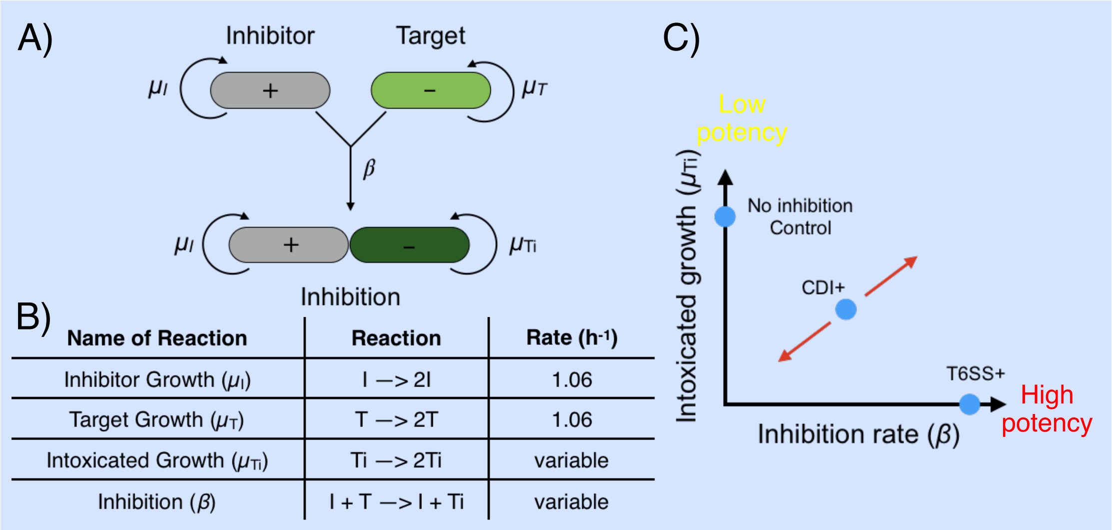

Name of Reaction	Reaction	Rate (h^{-1})
Inhibitor Growth (μ_I)	I —> 2I	1.06
Target Growth (μ_T)	T —> 2T	1.06
Intoxicated Growth (μ_{Ti})	Ti —> 2Ti	variable
Inhibition (β)	I + T —> I + Ti	variable

Figure 23: **Model framework for contact inhibition.** A) State diagram of inhibition. B) Cell state reactions. Reactions are included for growth of each cell type and inhibition. Growth rates come from measuments of single cell data (Figure 24). The intoxicated growth rate of target cells (μ_{Ti}) and inhibition rate (β) were varied in simulations. C) Parameter space diagram. Control inhibitor cells that show no inhibition have low inhibition potency via both low inhibition rate and high intoxicated growth rate (100% of base growth rate). T6SS has high inhibition potency by low intoxicated growth rate and potentially high inhibition rate. CDI has intermediate potency but the influence of intoxicated growth and inhibition rate parameters is not clear from experimental data only. To help in distinguishing between microscopy and simulations data from this point figures will be colour coded: yellow for microscopy and blue for simulations.

and nine divisions in four hours. From an average of this division data a doubling time could be calculated which was then used to calculate a base growth rate, using the formula: growth rate = ln(2)/doubling time. An average of 6.1 divisions in 4 hours gives a doubling time of 0.66. To put this into the growth rate formula; ln(2)/0.66 gives a base growth rate of 1.06 h^{-1} for cells without inhibition. Both inhibitor and target cells were grouped to calculate base growth as the division distributions were the same (data not shown).

To verify that using the base growth rate in simulations gives a similar distribution of cell divisions, the number of divisions of control target cells not in contact with inhibitor cells and also inhibitor cells from simulations, were plotted and compared to the single cell data (Figure 24b compared to 24a). This showed that simulations have a distribution that is slightly skewed to more divisions. There is also a tighter distribution suggesting slightly less stochasticity in the growth dynamics than in microscopy.

To parameterise the target volume, the cell lengths one frame before division in microscopy time-lapses were measured for control target cells not in contact with inhibitor cells and inhibitor cells (Figure 24c, data used from experiments in Chapter 3). The cell lengths fitted a log-normal distribution so a log-normal random number generator was used in the model to generate cell lengths within this distribution. The mean of 4 and standard deviation of 0.9 with 500 random numbers from this distribution were plotted (Figure 24d) to compare to the microscopy cell length data (Figure 24c). The simulation distribution was slightly broader but showed the same mean and standard deviation as microscopy data.

5.2.1.2 Validating simulations by comparison with single cell microscopy data

The base growth rate calculated from microscopy data was used as control growth in simulations. This was then systematically reduced to explore intoxicated growth rate of target cells between 1.06 h^{-1}, which is no growth inhibition to 0 h^{-1}, which is complete growth inhibition. At the same time inhibition rate was varied within the range of 0.001 to 10 insertions h^{-1} cell^{-1}. A wide range of inhibition rate values was chosen to see where the threshold of its affects were seen. The inhibition rate was used in the Gibson-Bruck algorithm to determine the reactions propensity to give stochasticity to the inhibition events. The aim was then to look at how the readout of divisions varied within this parameter space and see which parameters, if any, fit to target cell division distributions seen in microscopy with CDI or T6SS inhibition. Figure 25 shows the number of target cell divisions as a percentage of all cells in a given simulation.

With a high inhibition rate ($\beta = 10$ or 1 h^{-1} cell^{-1}) and low intoxicated growth ($\mu_{\mathrm{Ti}} = 0\%$ of base growth (0.0 h^{-1})) the number of target cell divisions was predominantly zero with a few cells dividing once (Figure 25). This is very similar to what is seen with T6SS in microscopy data; cells are inhibited within one cell division but some do divide if they were about to divide just before contact was made. The target cell divisions are the same for an inhibition rate of 1 and 10 h^{-1} because division data can only give a resolution of within one division. With reducing inhibition rate the trend is to shift to higher number of divisions as the chance of inhibition becomes lower. This is because the remaining target cells that are not inhibited divide as normal (left columns of Figure 25). At an inhibition rate of 0.1 h^{-1} cell^{-1} a bimodal distribution with half the population being inhibited and half not was seen, when intoxicated growth is also low (middle pannels on the two top rows of Figure 25). At a very low inhibition rate of 0.001 h^{-1} cell^{-1}, inhibition is an extremely rare event where it is only seen in a couple of cells. Therefore the target cell division distribution is close to control (Figure 24b), independent of changing the

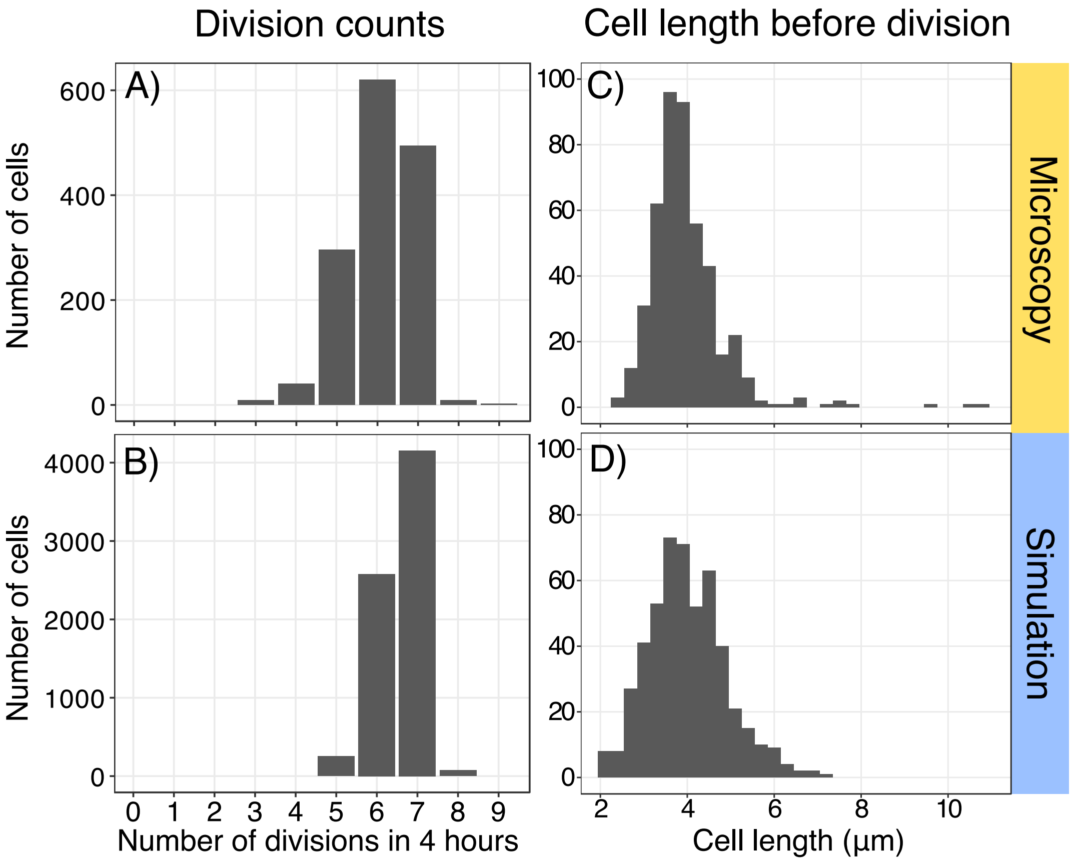
Division counts
Cell length before division
A)
B)
C)
D)
Number of cells
600
400
200
0
4000
3000
2000
1000
0
100
80
60
40
20
0
0 1 2 3 4 5 6 7 8 9
Number of divisions in 4 hours
2 4 6 8 10
Cell length (µm)
Microscopy
Simulation

intoxicated growth rate. As the intoxicated growth rate increases (looking down the rows in Figure 25 indicating less growth rate reduction) this trends the divisions toward higher numbers, as even cells that have been inhibited continue to grow and divide. With high intoxicated growth (μ_{Ti} = 80% of base growth (0.85 h^{-1}) the divisions are reaching a distribution close to control (Figure 24b) even with high inhibition rates.

Figure 26 shows single cell division results from microscopy and simulations that fit a similar distribution. T6SS simulations are very similar to microscopy with over 80% of target cells in contact with inhibitor cells undergoing no divisions (Figure 26a and 26b). For CDI the same trend is seen but the number of divisions is slightly higher in simulation for cells that are both inhibited and not inhibited (Figure 26c and 26d). However, these simulation parameters do show that a small subset of cells are inhibited to the same extent (less than five divisions) as seen in microscopy. The cells having slightly higher average growth rate fits with the parameterisation distribution (Figure 24a and 24b), where the cells division average is slightly higher in simulations than microscopy.

Figure 24 *(preceding page)*: **Single cell microscopy data used to calculate growth rate and target volume for simulation parameterisation.** a) Target cell division counts from microscopy including six target cell colonies from CDI experiments, four target cell colonies from T6SS experiments and two colonies of inhibitor cells (one from T6SS and one from CDI experiments). These values are all growth without contact or inhibition. An average of 6.1 divisions in 4 hours gives a doubling time of 0.66. Growth rate = ln(2)/doubling time -> ln(2)/0.66 = 1.06 h^{-1}. One biological replicate used per competition (CDI and T6SS). B) Number of divisions of target and inhibitor cells growing with no inhibition in CellModeller simulations (simulation parameters: μ_{Ti}= 1.06, β = 0.0). Simulations were run for four hours with no inhibition, then the number of divisions for all cells at the end point were counted. One simulation run used. C) Length of cells were measured one frame before division in microscopy time-lapses. Target and inhibitor cells measured from one biological replicate for each competition (CDI and T6SS). The cell lengths fit a log-normal distribution so a log-normal random number generator was used in the model to generate cell lengths within this distribution. To generate random numbers with a log-normal distribution using NumPy in Python, the mean (μ) and standard deviation (σ) of the normal distribution need to be calculated: mean = 4, SD = 0.9 -> μ = 1.36, σ = 0.22. D) 500 random numbers generated using np.random.log-normal(1.36,0.22,500). Mean = 4, SD = 0.9.

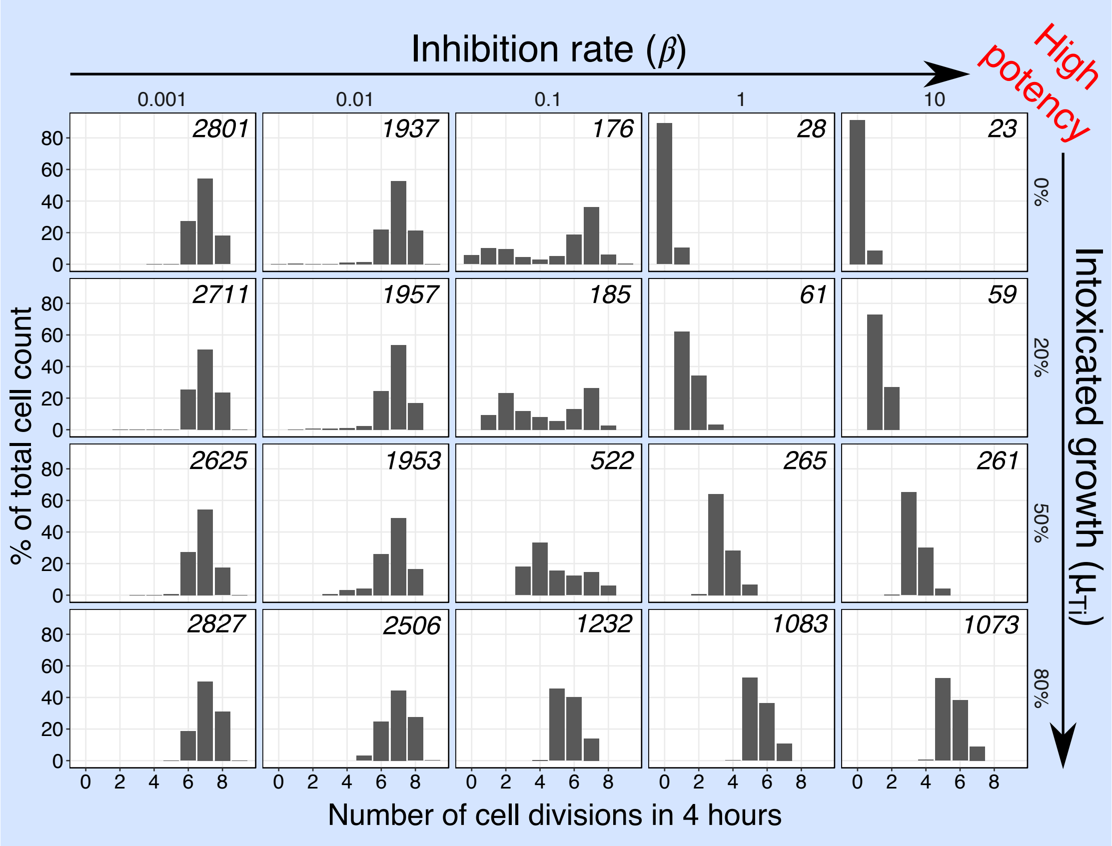

Figure 25: **The distribution of the number of divisions of target cells change as inhibition rate (β) and intoxicated growth ($\mu_{\mathbf{Ti}}$) are varied in simulations.** Number of divisions of target cells in contact with inhibitor cells. Target cells are tracked from the start of the simulation and only included if they stay in contact for four hours, to be in line with the microscopy data. Divisions are plotted as a percentage of the total cells counted in that simulation. Inhibition rate is varied from 0.001 to 10 insertions h^{-1} cell^{-1}. Intoxicated growth is given as a percentage of base growth (measured from not in contact target and inhibitor cells and calculated in Figure 24 as 1.06 h^{-1}) so 0% is a growth rate of 0 h^{-1} etc. Values in the top right indicate the number of target cells counted in that simulation. This varies considerably between simulations as high inhibition potency causes all target cells to be quickly inhibited and therefore the population cannot expand. With increased intoxicated growth the population continues to expand even with fast inhibition rates giving more target cells. One simulation used for each parameter set.

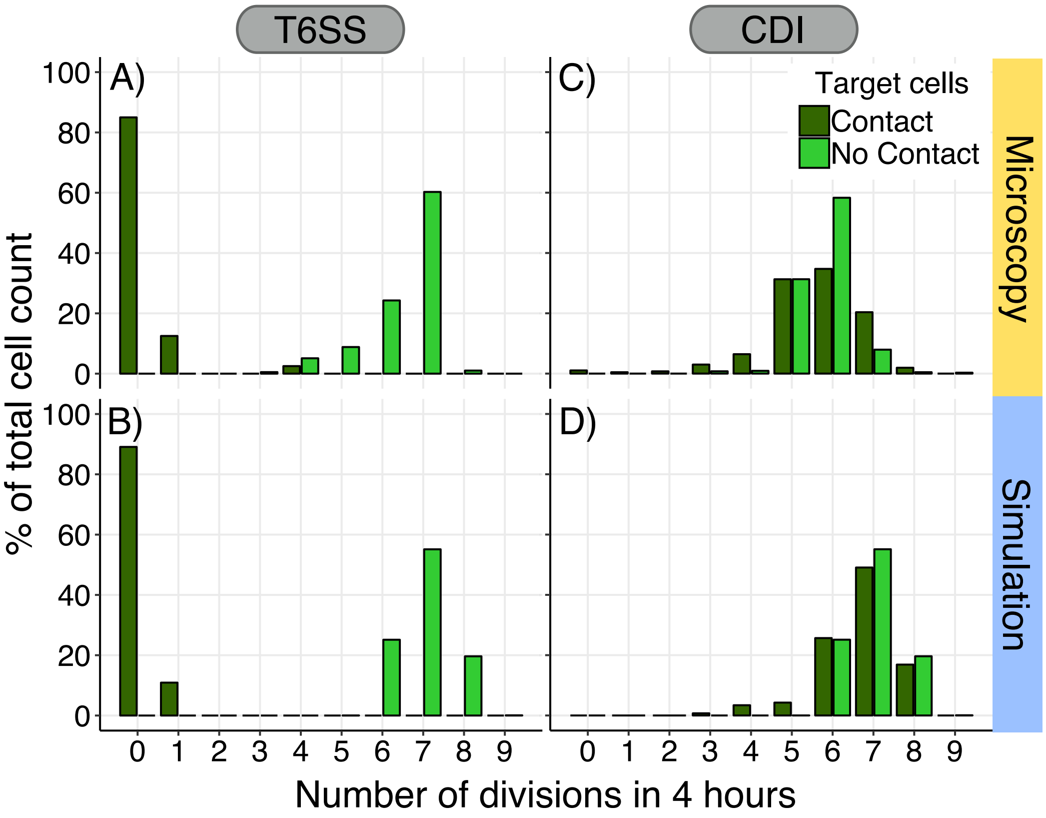

Figure 26: **Simulations with similar division dynamics to microscopy single cell division data.** Number of cell divisions of target cells in contact with inhibitor cells from the start of the time-lapse (T0) for four hours (dark green bars) and target cells not in contact with inhibitor cells (from separate microcolonies in the same experiment - light green bars) with: A) T6SS in microscopy: ECL WT; B) T6SS-like simulation: $\mu_{\mathrm{Ti}}= 0.0$ h^{-1} (0%), $\beta = 1.0$ insertions h^{-1} cell^{-1}; C) CDI in microscopy: ECL Δ*araBAD* Δ*Vask1*: D) CDI-like simulation: $\mu_{\mathrm{Ti}}= 0.53$ h^{-1} (50%), $\beta = 0.01$ insertions h^{-1} cell^{-1}. Microscopy target strains: MG1655::attB-gfp. Simulation control parameters: $\mu_{\mathrm{Ti}}= 1.06$ h^{-1} (100%), $\beta = 0.0$ insertions h^{-1} cell^{-1}. One biological replicate used per experimental competition and one simulation per competition type (CDI and T6SS).

In this section the aim was to parameterise and validate simulations based on microscopy single cell data. This was done using control cells to measure growth rate and cell length. Using these parameters two factors that contribute to overall inhibition potency: inhibition rate (β) and intoxicated growth (μ_{Ti}) could be explored in simulations. Using a wide range of parameters, the threshold of minimum and maximum rates needed to affect the division distribution have been identified. Simulations have then been used to show that both inhibition rate (β) and intoxicated growth (μ_{Ti}) together lead to high inhibition potency. Experimental CDI and T6SS division data can be matched to simulation parameters, showing that a certain combination of these parameters can lead to the given outputs, this does not exclude other possible solutions. The next step is to understand how inhibition potency affects spatial structure in microcolony growth.

5.2.2 Investigating microcolony spatial structure in simulations and microscopy

To look at spatial structure, two species competitions (inhibitor and target) were set up to look at how their interactions affect the formation of the resultant microcolonies. To do this cells were seeded (in simulation or microscopy) at higher density than for single cell analysis, so the two species could interact within a short time scale. A fractal dimension (Fd) method was developed to analyse the spatial structure by looking at the interaction border between the two cell types. For the Fd analysis the setup for colonies where the full field of view is covered with cells is needed (Fd method development discussed in Chapter 4).

For simulations to be set up in a equivalent manner to microscopy, the number of cells at time = 0 (T0) were counted and the distribution used to seed simulations. Figure 27a shows the distribution of cell counts from twelve microscopy images, from one biological replicate. A normal distribution was used as the best approximation giving a distribution in simulations seen in Figure 27b. Images of microscopy and simulations show some slight difference (Figure 27). In microscopy clumping of cells is seen with both ECL inhibitor cells and *E. coli* target cells. These clumped cells were counted as one cell, as it was not possible to distinguish all cells and some cells had divided once by the time the image was taken (this differed between the first images taken and the last in the same data set). This clumping was not included in simulations.

5.2.2.1 Spatial structure in simulations

The range of simulation parameters that was used to look at single cell interactions (Figure 25) was used to look at the range of spatial structures that can be created. Figure 28 shows the structures with high inhibition potency (β = 10 h^{-1} cell^{-1}, μ_{Ti} = 0% (0 h^{-1})) trending to low potency (β = 0.001 h^{-1} cell^{-1}, μ_{Ti} = 80% (0.85 h^{-1})). Looking at just single images there are no clear-cut differences between high and low potency. However, with high potency there is more inhibitor dominance and at low potency a higher proportion of target cells are seen. Looking at one image alone is not sufficient for interpretation, as there is heterogeneity such as the seeding cell number, that could also influence the structure within the same parameter set. Statistical analysis of these structures is needed to quantify differences.

The fractal dimension was used to measure the interaction surface between the two cell types (target and inhibitors). Discussion of the Fd method development can be found in Chapter 5. Fractal dimension analysis was run on ten repeat microcolony images from simulations (images as seen in Figure 28). The general trend is that low potency ($\beta = 0.001$ h^{-1}, $\mu_{\mathrm{Ti}} = 80\%$ (0.85 h^{-1})) gives higher Fd and high potency ($\beta = 10$ h^{-1}, $\mu_{\mathrm{Ti}} = 0\%$ (0 h^{-1})) gives lower Fd (Figure 29). With

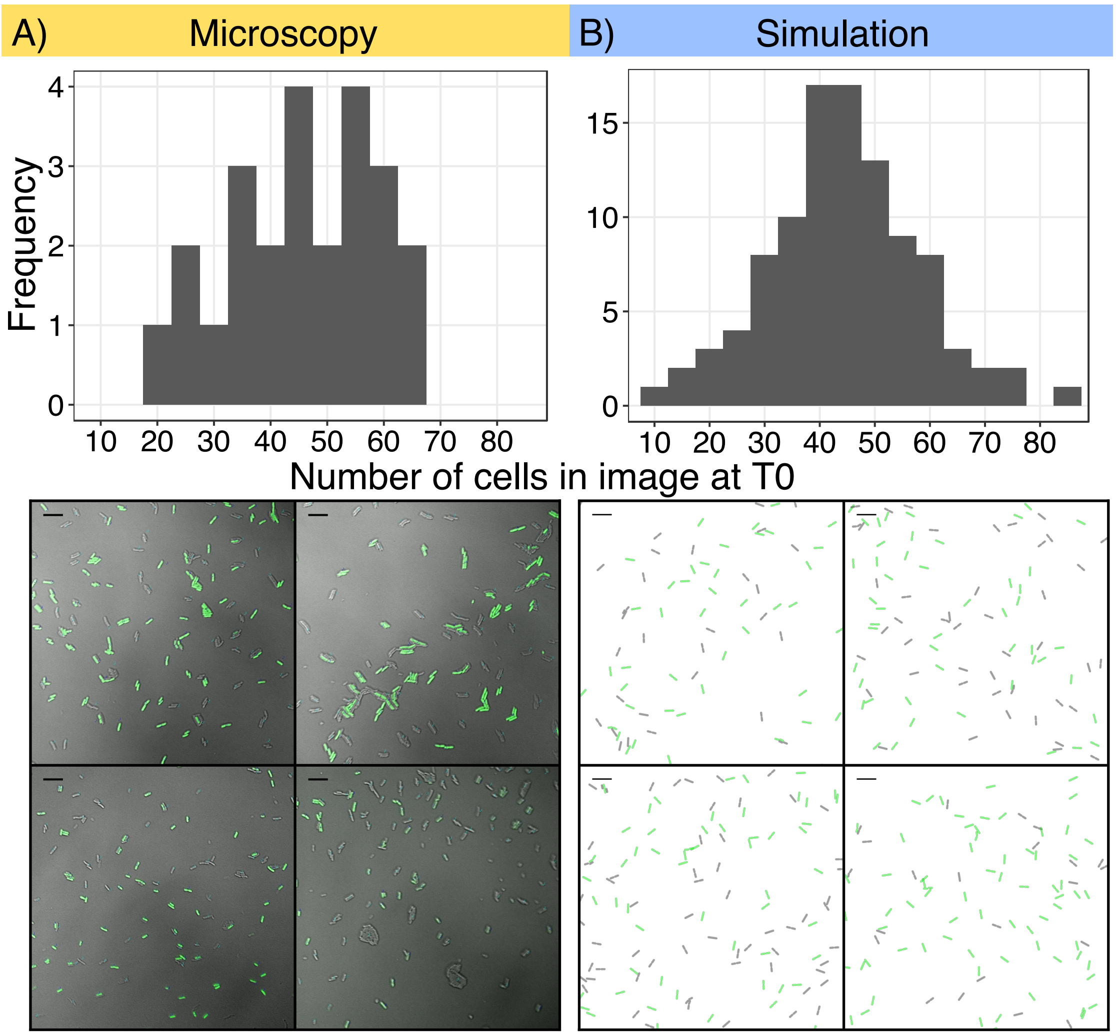

Figure 27: **Parameterisation of cell seeding numbers for microcolony growth.** A) Count of cell numbers at T0. n= 12 images from one biological replicate. The mean of 46 and standard deviation of 12.9 were used in simulations for generating number of cells to be seeded. Four example images of microscopy seeding at T0. Scale bars correspond to 10 μm. B) Generation of numbers using np.random.normal(46, 12.9, 100) to show the distribution start numbers that were chosen within simulations. Four example images of simulation seeding at T0. Scale bars correspond to 10 μm.

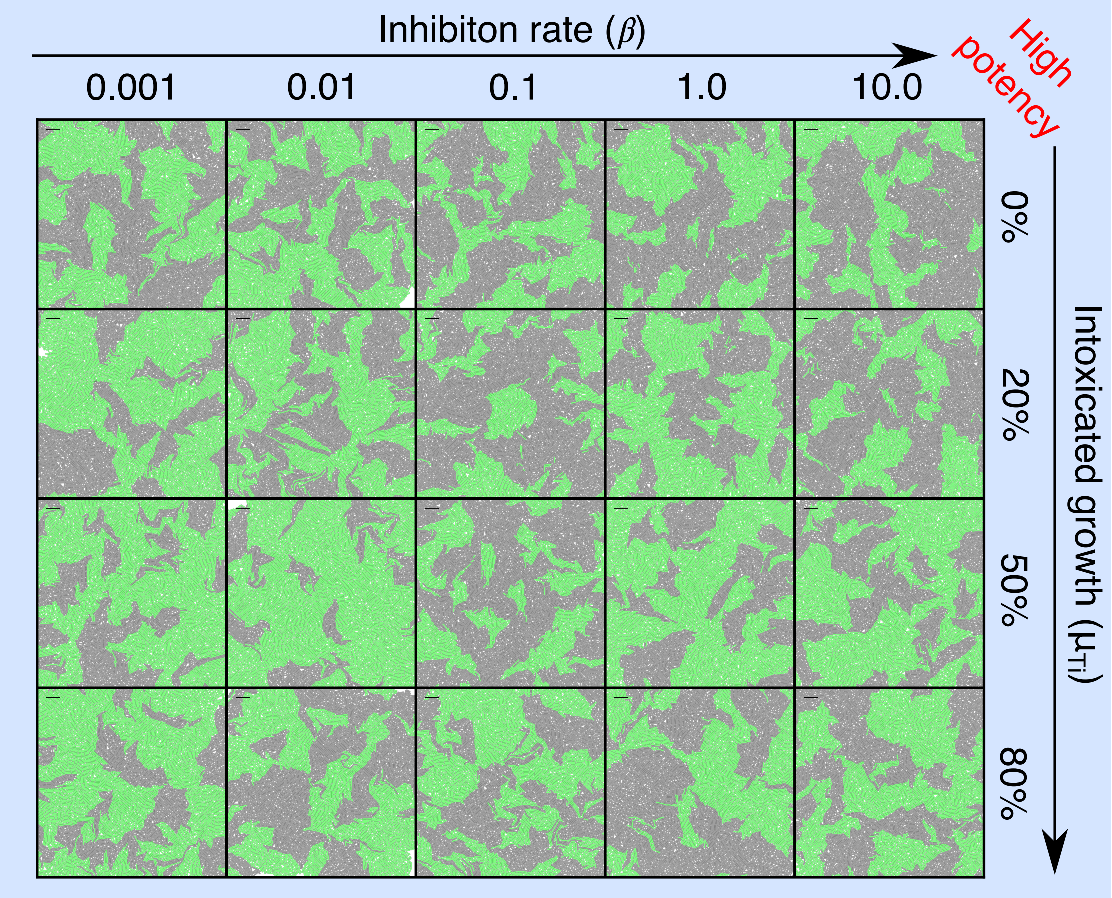

Figure 28: **Simulation images don't show clear difference in spatial structure with differing inhibition potency.** One example of 10 repeat simulations for each parameter set. Intoxicated growth is a percentage of base growth (1.06 h^{-1} = 100%) as calculated from control cells in microscopy (Figure 24a). Target cells = green, inhibitor cells = grey. Scale bars correspond to 10 μm.

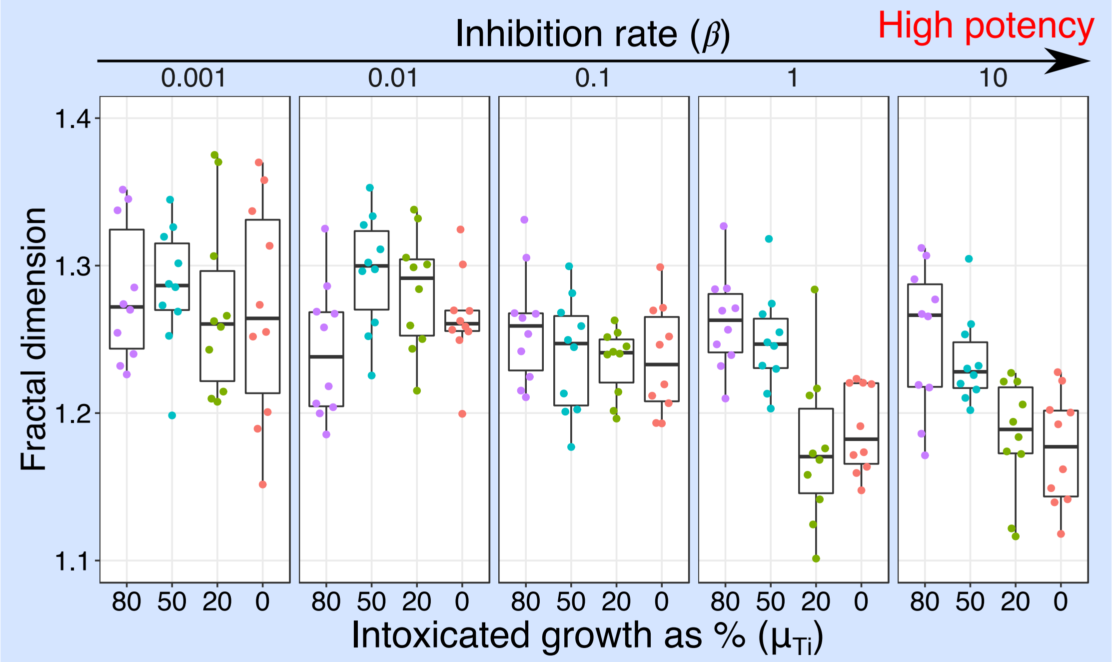

Figure 29: **Spatial analysis with the fractal dimension (Fd) shows a decrease in border complexity with increased inhibition rate and decrease in intoxicated growth rate in simulations.** Fd is measured on ten images per simulation (Figure 28 shows one example image for each parameter set). Coloured by intoxicated growth.

a low inhibition rate the Fd does not differ when intoxicated growth is varied. From an inhibition rate of 0.01 h^{-1} cell^{-1} and higher there starts to be a decrease in Fd. From an inhibition rate of 1 h^{-1} cell^{-1} and higher, the Fd decreases with the intoxicated growth becoming a more influential factor. This suggests that a combination of the two parameters leads to a stronger structural effect. A reduction in Fd shows that there is a reduction in interaction surface between the two cell types. This measure defines both the fractality of the border and also the total abundance of borders in the image. In control images the two cell types grow into each other which creates convoluted borders due to the pushing of cells against one another as they grow. With high inhibition potency, target and inhibitor cells disperse less into the other cell type, due to the growth rate reduction of target cells at the border. This Fd analysis (Figure 29) has been able to show fine scale differences in structure which are not obvious from just visual inspection (Figure 28).

5.2.2.2 Spatial structure in microscopy

To compare to simulations T6SS, CDI and control inhibitor cells were competed against *E. coli* target cells in conditions equivalent to those in simulations. Confocal microscopy was used to image these microcolony images and then the Fd was measured.

For all competitions *E. coli* MG1655 attB::gfp is used as a target strain (as was done in single cell microscopy in Chapter 3). Inhibitor strains made by Beck et al. [82] were used as follows: T6SS+: ECL WT. WT can be used for T6SS inhibition as CDI is not functional in WT cells under laboratory conditions [82]; CDI+: ECL araC$^{\mathrm{Eco}}$::cdiB Δ*araBAD* Δ*vask1.* The araC promotor from *E. coli* was placed upstream of the *E. cloacae cdi* locus to be able to induce the *cdi* genes with arabinose and the T6SS function was deleted via Δ*vask1*; T6SS-/CDI- control: ECL Δ*vask1.* Vask1 is an essential structural component of the T6SS and its deletion disrupts T6SS function [105].

Figure 30 shows an example of microscopy images compared to simulation images for T6SS, CDI and control inhibition. There are some features that can be compared with visual inspection: with T6SS more of the field is dominated by inhibitor cells, whereas with CDI and control the target cell population is more dominant, particularly in microscopy. Control and CDI inhibition show more intermixing of cell types than T6SS inhibition does. Comparison of the Fd shows CDI results are not significantly different between microscopy and simulation (Figure 30). The Fd for T6SS and control are significantly different between microscopy and simulation, however they still follow the same trend which can be seen in Figure 31.

For control inhibition the simulation Fd results are lower than microscopy, showing the complexity of the border or density of interaction surface is underrepresented in simulations. For T6SS inhibition the simulation Fd results are higher in simulations, showing an over representation of interaction border compared to microscopy. This could be due to more small patches being present in simulations. In simulation, inhibited small patches remained in the image even if they are not growing as the simulation runs in 2D. In contrast, in microscopy the colonies became 3D after extended growth meaning growing cells (inhibitor cells) were covered up by not growing cells (inhibited target cells). This can be seen in the comparison of microscopy and simulation images where there are very few small groups of target cells in the microscopy image, but there are small patches of target cells in the simulation (Figure 30).

As well as the difference in values, the simulations do not show such a wide range of Fd values, and therefore of structures as is seen in microscopy (Figure 30). Although there may be some aspect of inhibition not being fully represented in simulations, leading to differences in the Fd between microscopy and simulation images the data still follows the same trend of reduced Fd with increasing inhibition potency. Figure 31 shows that in both microscopy and simulations the Fd for T6SS inhibition is significantly lower than control, whereas the Fd with CDI inhibition is not.

5.2.2.3 Simulation spatial analysis with the pair correlation function

The Fd shows how the cell border interactions are changed with inhibition but it is still unclear to what extent the inhibition potency has an affect on the overall structure in terms of clustering of cell types. To look in more detail at differences in microcolony structure the pair correlation function (pcf) was used on simulation images to see if inhibition affects the cell types segregation. The pair correlation measures the distribution of cell to cell distances and produces a correlation for distance between cells of the same type and cells of the opposite type, to show the probability of finding like or not-like cells within a given radius.

In Figure 32 three examples of patterns have been used to show what correlations to expect using pcf analysis. Random distribution of points (Figure 32a) shows a similar correlation distribution for target:target, inhibitor:inhibitor and inhibitor:target pairs. When the two cell types are split into two patches covering half the field (Figure 32b), the correlation for the same cell type shows a high probability of being within a smaller radius which decreases as the radius increases. The target:inhibitor correlation shows the probability of finding the opposite cell type highest at a radius of ∼75 which is the middle of the field. A similar correlation distribution is seen with four patches as with two (Figure 32c compared to 32b) but an increased probability of cells being in a radius of 75 to 150 is seen with four patches of like:like correlations.

In simulations there is not a big difference between control, CDI-like and T6SS-like microcolonies with the pcf (Figure 33). This suggests that patch formation is not considerably changed by inhibition. This could mean that the inhibition is predominantly affecting the borders and not the whole population. This is very dependent on the simulation set up and how long the cells have to interact and expand. These experiments were run for four hours so it may not be long enough to have a significant effect on total population numbers. The density of seeding is also an important factor for this.

To investigate the effect of seeding density on spatial structure in simulations four different target:inhibitor ratios were tested: 10:10, 25:25, 50:50 and 100:100 cells per field. The parameters for control (μ_{Ti}= 1.06 h^{-1} (50%), $\beta = 0.0$ insertions h^{-1} cell^{-1}), CDI-like (μ_{Ti}= 0.53 h^{-1} (50%), $\beta = 0.01$ insertions h^{-1} cell^{-1}) and T6SS-like (μ_{Ti}= 0.0 h^{-1} (0%), $\beta = 1.0$ insertions h^{-1} cell^{-1}) simulations were examined (Figure 34).

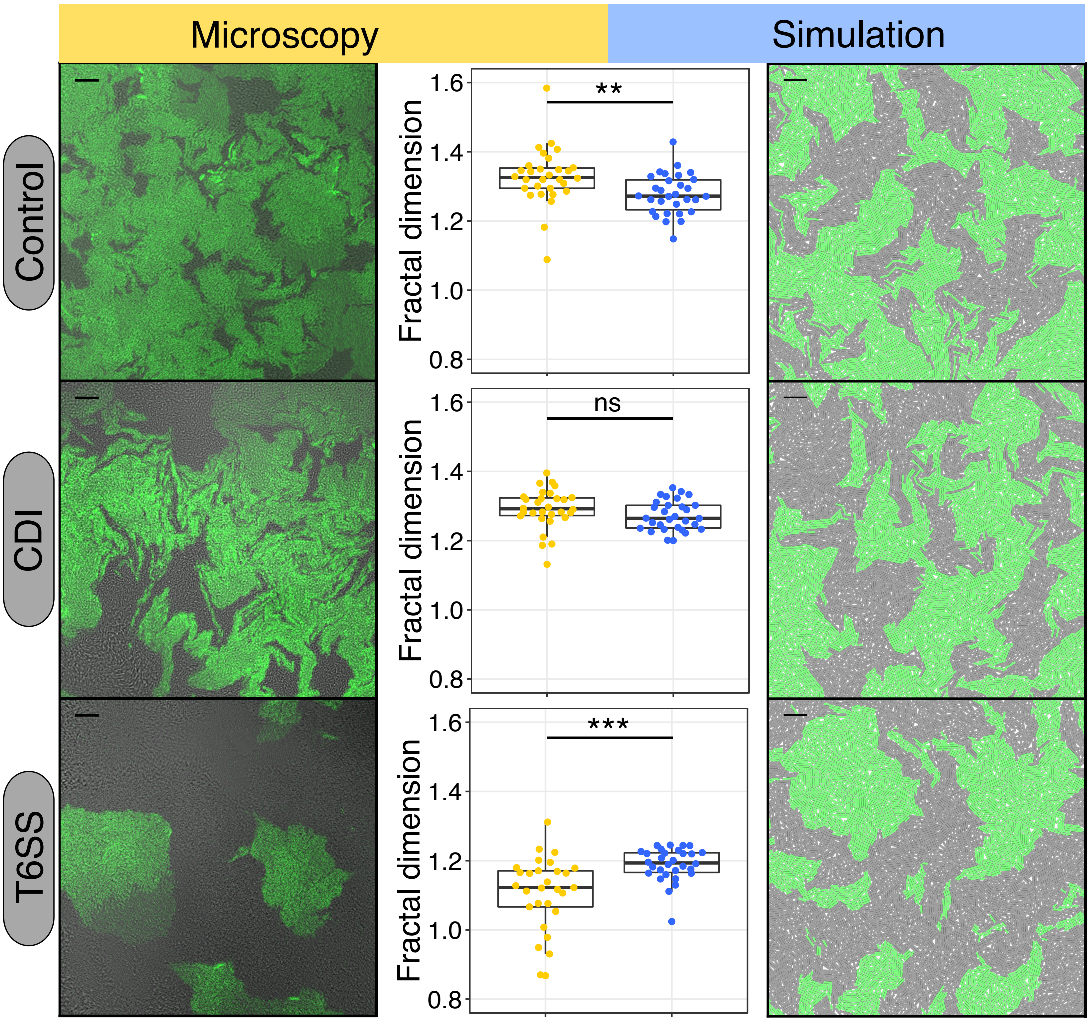

Figure 30: **Images from microscopy compared to simulations both show lower Fd with increased inhibition potency.** Microscopy is one example from 30 repeat images from three independent experiments. Simulations are one of 30 repeats. Graphs in the middle column show Fd dimension for the 30 repeat images from microscopy or simulation. Significance levels from one-way ANOVA: ***$p < 0.001$, **$p < 0.01$, ns < 1. Target = green, Inhibitor = grey in both simulations and microscopy. Scale bars correspond to 10 μm for both microscopy and simulation images.

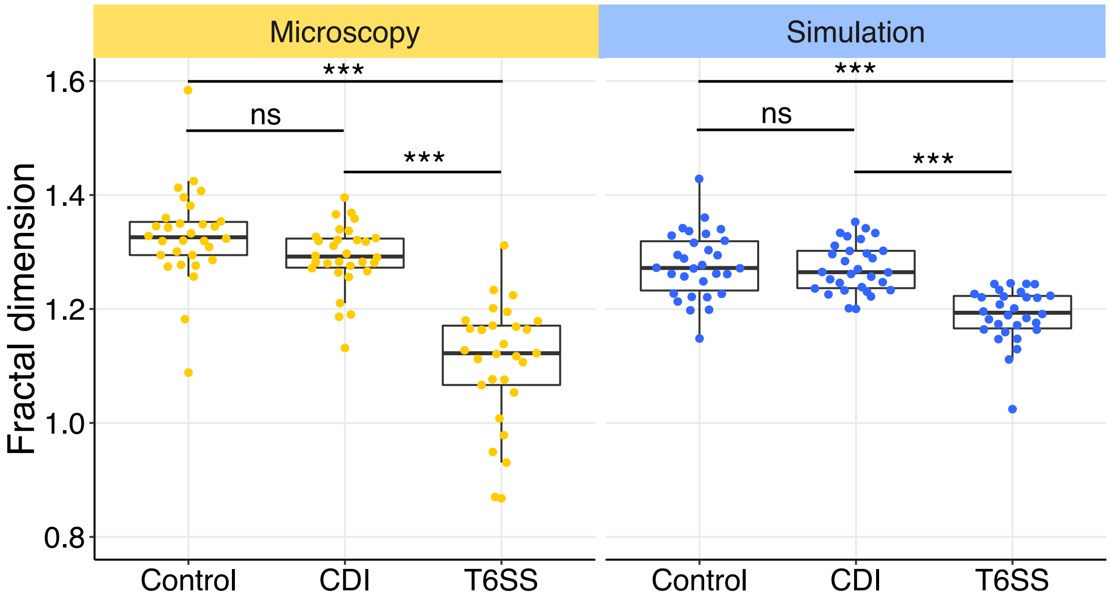

Figure 31: **T6SS shows significantly different structure to control in microscopy and simulation using the Fd but CDI does not.** The same data is used as in Figure 30. Fd results are from 30 microscopy images from three independent experiments and 30 simulations. Significance levels from one-way ANOVA and post-hoc Tukey HSD: ***p < 0.001, ns < 1.

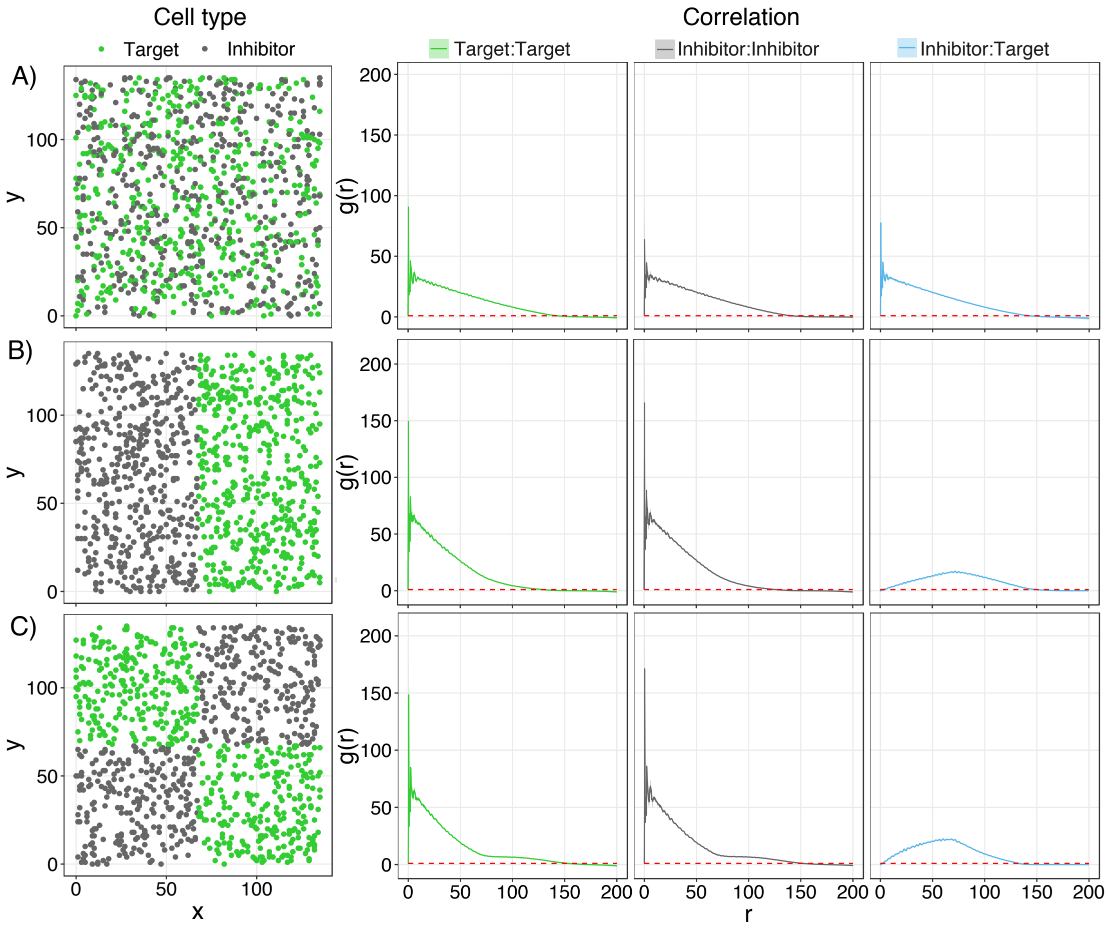

Figure 32: **Example random cell distributions to show pair correlation function outputs.** A) random distribution. B) 50/50 split of cell types into two large patches. C) Cells split into four patches. 500 cells per type for each example, r = radius in μm, g(r) is pair correlation function. Shaded area is 95% confidence interval of n=10. Cells placed in a 135x135 μm area.

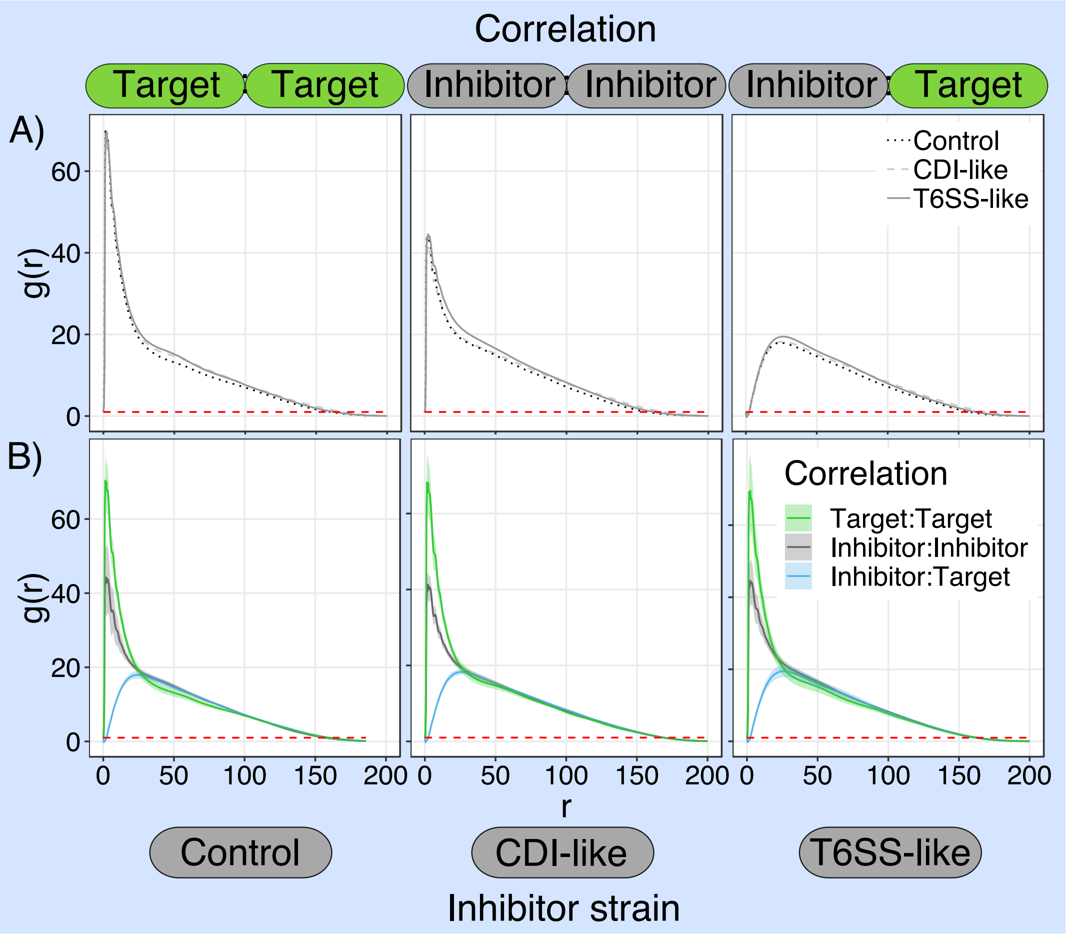

Figure 33: **Spatial analysis using the pair correlation function shows no difference in patch formation between control, CDI-like or T6SS-like simulations.** A) Comparing target:target, inhibitor:inhibitor and inhibitor:target pcf correlations between simulations. B) Comparing control, CDI-like or T6SS-like simulations between cell type correlations. Shaded area shows 95% confidence interval of n=30.

These simulations show that the spatial structures are density dependent. This is in line with results from Bottery et al. [1], who also show density dependent structural change with CDI in microscopy and simulations. This is also shown in other contact and not contact dependent toxin systems [26, 76]. Here the pcf shows that differences between simulations only begin to be seen when 50+ cells of each type are seeded in the 135x135 μm area. (Figure 34a). For low numbers of cells seeded (10:10) clonal cell patches expand and only rarely interact with the other cell type, therefore the effect of the interaction is not influential enough to be detected (Figure 34b). With 25:25 cells per field interactions at the borders of cell types starts to occur but this still does not have an effect on the domain size (Figure 34a 25:25 seeding ratio). With seeding ratios of 50:50 and 100:100 target:inhibitor cell there starts to be some differentiation between pcf target:target correlation. This can predominantly be seen to affect the target:target cell correlations (Figure 34a), where in T6SS-like inhibition there is a higher probability of finding other target cells with a smaller radius than with control or CDI-like inhibition. This shows that target cells are more likely to be clustered. The inhibitor:inhibitor and inhibitor:target correlations are not changed with differing inhibition potency when seeding density increases. This suggests that potent inhibition imposes structure on target cell populations. This goes along with a decreased target cell fraction (Figure 34c). With control and CDI-like inhibition the target cell fraction stays around 50% even as the seeding density increases. With T6SS-like inhibition there is an effect on the fraction of target cells even at a lower seeding density. At a higher seeding density, inhibition of target cells happens fast enough to reduce the number of cells that can expand the population.

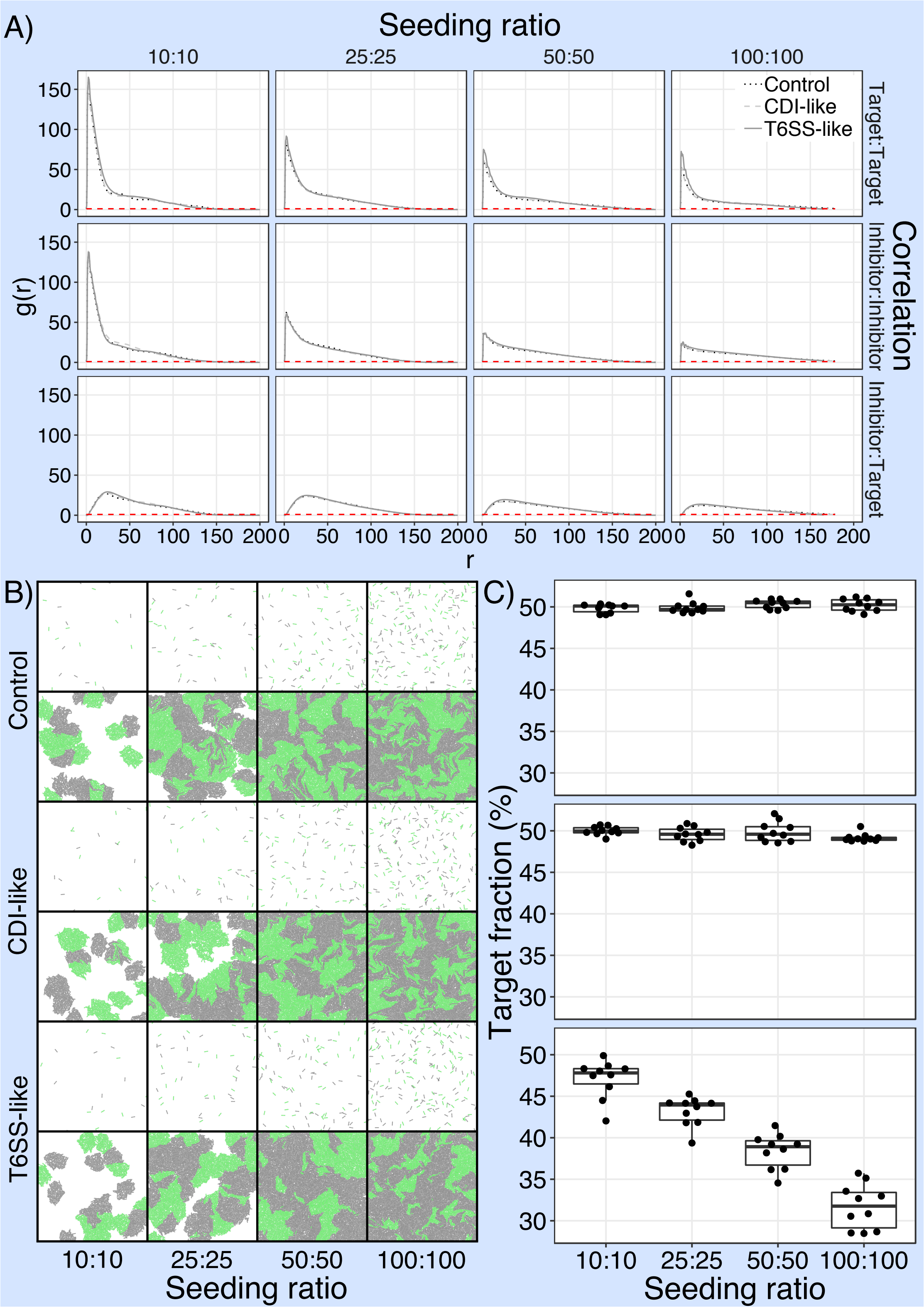
A)
Seeding ratio
10:10
25:25
50:50
100:100
Control
CDI-like
T6SS-like
g(r)
150
100
50
0
r
0
50
100
150
200
Target:Target
Inhibitor:Inhibitor
Inhibitor:Target
Correlation
B)
Control
CDI-like
T6SS-like
10:10
25:25
50:50
100:100
Seeding ratio
C)
Target fraction (%)
50
45
40
35
30
10:10
25:25
50:50
100:100
Seeding ratio

5.3 Discussion

The first part of this chapter includes work that aimed to parameterise an IBM of contact inhibition in the CellModeller software using single cell data (from Chapter 3). The approach chosen was to parameterise the model with control (no inhibition) growth rates and then use equivalent outputs from simulations to compare to single cell data for control, T6SS and CDI inhibition from microscopy. Using a stochastic algorithm (Gibson-Bruck) to control inhibition in the simulation allows the emergence of structure from the input of single cell detail. Inhibition rate is not accurately measured in single cell microscopy so simulations can help to understand this parameter.

The control simulations show a similar distribution to control microscopy division counts. However, the simulations show a slightly less heterogeneous distribution than microscopy (Figure 24a and 24b). This could be due to the averaging of the growth rate parameter. Overall growth of cells is defined by two factors: growth rate which controls cell length expansion over time, and the target volume of a cell which defines when a cell divides. The growth rate was parameterised as a single value taken from average division counts whereas the target volume value was randomly selected from a distribution. If the growth rate were also to be selected from a distribution this could add more stochasticity to the outcome. Another option to improve the parameterisation of growth rate would be by using cell length tracking. If a large number of cells can be measured and the growth rates determined by linear regression this could be a more accurate growth parameterisation. There is possibility for this with new software being developed, for example Balomenos et al. [113] claim that their software, which is currently not out, will be able to cope with segmentation of cells in overcrowded microcolonies.

By comparing simulation division data to microscopy, parameter distributions which fit T6SS and CDI division were identified. The T6SS parameters fit expectation, with the intoxicated

Figure 34 *(preceding page)*: **Simulations show seeding density dependent spatial phenotypes.** Simulations of control (μ_{Ti}= 1.06 h^{-1} (100%), β = 0.0 insertions h^{-1} cell^{-1}), CDI-like (μ_{Ti}= 0.53 h^{-1} (50%), β = 0.01 insertions h^{-1} cell^{-1}) and T6SS-like parameters (μ_{Ti}= 0.0 h^{-1} (0%), β = 1.0 insertions h^{-1} cell^{-1}) were run with differing seeding ratios: 10:10, 25:25, 50:50 and 100:100 target:inhibitor cells in 135x135 μm area (dimensions comparable to microscopy). A) Pair correlation analysis, n = 10. B) Images at T0 and T4 hours, one example of ten images per simulation. C) Fraction of target cell from T4 images, n = 10.

growth rate being 0 h^{-1} and the inhibition rate being within one division (the division data cannot give higher resolution for speed of inhibition). The exploration of the speed of inhibition will be discussed in the next chapter (Chapter 6). The T6SS in ECL studied here differs in comparison to T6SS in other species visualised at the single cell level in that it does not cause lysis of target cells [88, 89]. The T6SS toxins present in ECL have been described by Donato et al. [84], showing there is Rhs1 (a nuclease), Rhs2 (a DNase), Tae4 (an amidase), Tle1 (a lipase) and a currently unknown toxin. The lipase and amidase are the candidates most likely to be able to cause cell lysis. They are enzymes that break down phospholipids in the cell membrane [125, 126] or break down the peptidoglycan cell wall [127], respectively. Ringel et al. [128] investigate which specific T6SS toxins in *Acinetobacter baylyi* cause lysis, showing Tae1 causes a strong lysis phenotype and Tle1 cause intermediate levels of lysis against *E. coli* target strain. In ECL the effect of individual effectors has not been investigated hence these effectors could be less influential in causing inhibition in ECL, as lysis is not seen. However, lysis will be discussed in more detail in Chapter 6.

Single cell data with CDI showed that the inhibition effect was heterogeneic (Chapter 3, Figure 6). Some cells followed a high inhibition rate response but some cells have a slower inhibition rate yet still stop growing completely (low intoxicated growth). The simulation parameter set that shows a distribution of divisions close to what is seen with CDI in microscopy is with an inhibition rate of 0.01 insertions h^{-1} $cell^{-1}$ and an intoxicated growth at 50% of base growth (0.53 h^{-1}). This is consistent with the single cell data that shows target cells do not completely stop growing in some cases.

The second section aimed to look at how contact inhibition affects spatial structure using microscopy and simulations. To give credible comparisons of colony structure between microscopy and simulation, the number of cells seeded in the field of view were counted. The counts of cells seeded was close to a normal distribution so this was used. However, using a normal distribution to generate seeding numbers in simulations generates a greater number of higher and lower values that were not seen in microscopy. Another difference between microscopy and simulation seeding was that cells in microscopy were often clumped or cells had divided once before images were taken. This happened because the time taken to image all positions used in the experiment would take approximately 30 minutes in which time cells could have divided. For this reason, clumps of cells in microscopy were counted as one cell to normalise for the time difference of image acquisition. However, clumps of cells could also be due to cell aggregation, this was not taken into account in simulations. Cell clumping could have a considerable effect on structure as clonal growth would allow bigger patches to form. This could be incorporated into simulations by seeding several cells at a given point or running the simulation for a few time steps before starting the four hour experiment. Autoaggregation is common in bacteria and is mediated by self-recognising surface structures [129]. In terms of contact mediated killing, aggregation could be a strategy for both cells harbouring the inhibition systems to form cluster, as it has been shown that CDI systems are involved in cell-cell aggregation [47], but there is also potential for it to be strategy for susceptible strains to use clumping as protection from contact inhibition.

Spatial analysis was carried out to compare microcolony structures. In previous analyses of bacterial microcolonies different methods have been used to look at spatial structure, ranging from simple methods such as looking at the fraction of cell types [76, 79, 121, 122] or looking at colony sectoring [1]. However, with different models being used it is often necessary to use analysis specific to that data. McNally et al. [78] modelled the T6SS in agent based models showing the occurrence of phase separation. They used assortment to analyse the spatial structures of colonies. Assortment is a measure used in evolutionary biology which assesses the frequency of a competitor strain at increasing distance from a focal strain compared to random assortment. This analysis was considered as similar images were being assessed. Assortment analysis (carried out using scripts from McNally et al. [78]) did not show a great deal of information in regards to small changes in structure. The reason this analysis is more applicable for the simulations from McNally et al. [78] is that they worked in a no net growth matrix, where each position was a cell and cells could divide or attack but they did not have any packing arrangements mediated by cell pushing, this means that they were more interested in patch size and not small scale structures.

The Fd and the pcf were chosen for this data as the Fd has been used on CellModeller data [93] and pcf has also been used as a method to assess cell aggregation [97]. Nadell et al. [130] use a segregation index to look at the structures created in agent based simulations when looking to species interactions via a cooperative trait. This method is very similar to the pcf where they are looking at which cell phenotypes are within a given radius of a focal cell.

When comparing the Fd in microscopy and simulations there is a wider range of structures in microscopy compared to simulations (even though the seeding variation is wider in simulations), this is quite prominent for T6SS data. One reason for this could be that small clusters of cells are grown over in microscopy so some images could end up with very few patches of target cells giving lower Fd values. In simulation as they are only run in 2D these small patches are still present and increase the Fd values. Overall the trends with the Fd are similar between microscopy and simulations.

The aim with pcf analysis was to see if the effect of inhibition could be seen on the greater population than just at the boundaries of cell types. There was not a clear difference seen between control, CDI and T6SS, showing that at this scale of colony growth there is not a considerable effect on the total population growth. This is likely due to the duration of the simulations and seeding conditions where the cell-cell interactions do not happen fast enough to have a large effect on clustering. This is backed up by the experiments where increasing seeding density leads to a change in T6SS (high inhibition potency) structure compared to control. This means with high density the cell-cell interactions occur fast enough to reduce clonal expansion and reduce patch size of target cell populations. This is in line with the hypothesis from Borenstein et al. [76] that with large enough populations target cells can survive T6SS assault, and Bottery et al. [1] who show density dependence affects spatial patterns. My data adds to the growing body of knowledge that suggests spatial segregation is needed for coexistence. Further suggesting inhibition systems like T6SS are methods to maintain segregation and not just extinction of competitors.

Due to the subtle inhibition seen at single cell level with CDI it is hard to see a clear spatial effect. In this setup of spatial analysis, measurable effect of low potency inhibition have on spatial structure have not been shown. However, when looking over a large range in inhibition potency with simulations, a continuous change in fine scale structure from the Fd measurement can be seen. To see a structural effect with low inhibition potency (such as CDI), longer times for growth expansion may be needed, as seen by Bottery et al. [1]. Range expansion competition allow the competition in the centre to show a larger effect at the edge of expanding colonies due to genetic drift [131].

In this section modelling has been used to investigate how inhibition affects spatial structure in 2D colony growth. It can be seen that there is a continuous change in structure with increasing inhibition. With high potency inhibition the interaction border between cell types is reduced which reduces intermixing of the strains. This segregation at the fine scale has implications in survival and stability in polymicrobial communities.

6 Using T6SS effector mutants to explore the effects of intermediate inhibition potency of bacterial contact inhibition on microcolony spatial structure

6.1 Introduction

The type VI secretion system displays a strong inhibitory phenotype by inserting multiple effectors simultaneously into the target cell [132]. The presence of multiple effectors gives the potential for manipulating the potency of inhibition by deleting one or more of the T6SS effectors (Figure 35). If effector mutants display reduced inhibition in single cell growth, the microcolony structure can be compared to the reduced inhibition levels explored in simulations (Chapter 5). In simulations the inhibition levels were varied by systematically changing both the inhibition rate (β) and the intoxicated target growth rate (μ_{Ti}) (see Figure 23 in Chapter 5). This continuous change in inhibition potency cannot be easily recreated experimentally. Simulations can therefore be powerful to explore the parameter space and trends in structural changes seen with changes in inhibition. The aim in this chapter was to use T6SS effector mutants as an experimental data point that shows intermediate inhibition that will fit somewhere within the range of simulated parameters to potentially validate the trends predicted in simulations.

Donato et al. [84] identified five T6SS effectors in ECL (four of the toxins are of known function). Single effector deletions show a minimal reduction in inhibition in population competitions on plates [84]. There is at most a 10-fold reduction in competitive index for a single effector deletion compared to WT (Δrhs1 (Figure 36b)). Deletion of Rhs1 and Rhs2 show the biggest reduction, however deletion of both Rhs effector proteins stops T6SS assembly and firing [84]. This may be due to the N-terminal PAAR domain in Rhs toxins which functions as the tip of the T6SS [133]. Figure 36 shows a range of Rhs1 and Rhs2 deletion mutants where one toxin is deleted and the other is truncated. For the truncated protein, the C-terminal with the toxin activity is removed, but the N-terminal which has a role in T6SS function is still present. Figure 36a shows the level of T6SS firing by western blot quantification of the Hcp protein, which is the inner tube of the T6SS machinery. The Hcp protein is released into the supernatant upon T6SS firing [134]. Mutants with the biggest reduction in competitive index compared to WT have lower levels of Hcp secretion, for example the strain Δrhs1 rhs2 1161::stop (Figure 36).

With the aim of using ECL T6SS effector mutant strains to assess reduced inhibition levels compared to WT (T6SS+), strains of interest were first assessed in population competitions

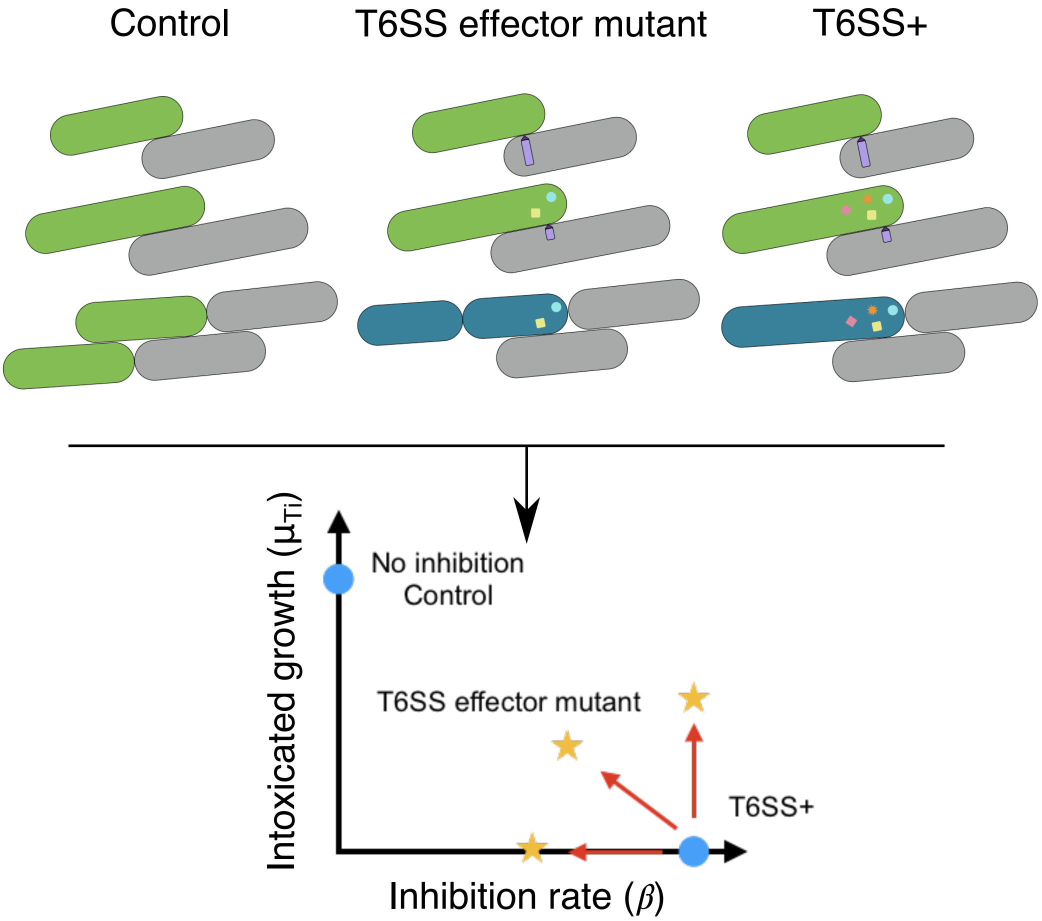

Figure 35: **Schematic of strategy to reduce inhibition potency using T6SS effector mutants.** Reducing the number of T6SS effectors could decrease the inhibitory effect on target cells. This could give a strain with reduced inhibition potency but whether it alters the single cell dynamics of inhibition, as represented by intoxicated growth or inhibition rate in the model, will need to be explored. Green cells = target, grey cells = inhibitor, blue cells = inhibited target cells.

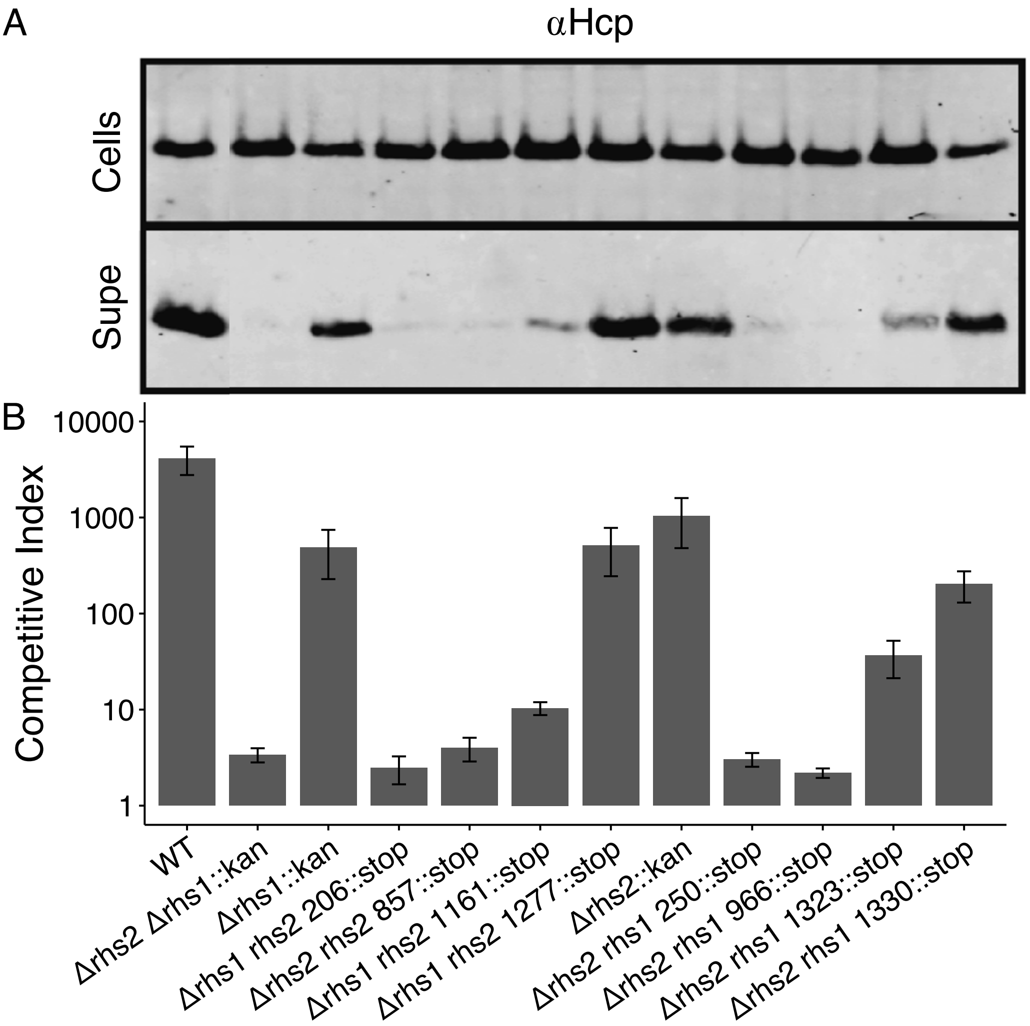

Figure 36: **ECL T6SS effector mutants show a reduction in competitive index compared to ECL WT.** A) Western blot with antibodies to Hcp protein shows levels of Hcp in the supernatant. If Hcp is not present in the supernatant this shows there is no T6SS firing in this strain. Deletion of both Rhs1 and Rhs2 stops T6SS firing but removal of only the C-terminal toxin of either Rhs1 or Rhs2 and leaving the N-terminal of one of these effectors preserves T6SS function. B) Competitive index shows relative growth of target and inhibitor cells, with a higher CI showing stronger inhibition of the target strain. There is reduction in inhibition of effector mutants compared to WT. Four hour competitions carried out on agar plates. n = 3. Error bars show SEM. Data presented in this figure from Donato et al. [84].

using the *E. coli* MG1655 targets previously used in this work. The growth of the target cells was then measured in single cell competition to show the effector deletion strain has a reduced inhibitory effect compared to WT. Subsequently the effector deletion strain showing intermediate inhibition was used in microcolony competitions to look at spatial structure in comparison to simulated microcolonies.

6.2 Results

In this chapter the methods developed in Chapters 3, 4 and 5 were used as a complete workflow to analyse a new strain at single cell and microcolony level and compare these results with simulations.

6.2.1 Population competitions to identify T6SS effector deletion strain with intermediate inhibition phenotype

Population level competitions were used to validate inhibition levels of inhibitor strains in order to decide which strain to use for further analysis. To be consistent with the previous work in this study, *E. coli* MG1655 was used as the target strain for population competitions on agar plates. Population competitions were carried out to see if the results were consistent with previous work where a different target strain, *E. coli* X90, was used [84]. Three ECL T6SS effector deletion strains which had the biggest reduction in competitive index (CI) compared to WT were tested: Δrhs2 rhs1 1323::stop, Δrhs2 rhs1 1330::stop, Δrhs1 rhs2 1161::stop.

In competition with MG1655, the inhibitor strain with the biggest reduction in competitive index was Δrhs2 rhs1 1323::stop (Figure 37a). This strain shows a 10-fold reduction in CI compared to WT. The same strain (Δrhs2 rhs1 1323::stop) shows a 100-fold reduction in CI with X90 [84] (Figure 36). The difference in the CI between my experiments and that of Donato et al. [84] could be due to the different target strain used. To see if this is the case, the competition was repeated with Δrhs2 rhs1 1323::stop against X90 as a target. In this competition with X90 there was a less than 10-fold reduction in CI compared to WT (Figure 37b), which is less than when competed against the MG1655 target (Figure 37a). Although there was a more than 10-fold difference in competitve index with the T6SS effector mutants between my experiments and that of Donato et al. [84], the CI values with WT inhibitor were still comparable in all competitions independent of target strain or who performed the experiment.

It is not clear what the reason is for the competitive index results between my experiments and the results from Donato et al. [84] being different. The same protocol was used, where competitions take place on agar plates for four hours, but the consistency between the exact reagents used and exact growth and plating methods could be different and these factors cannot be verified as experiments were carried out in different labs at different times. However, the WT strain gave a reproducible CI in all experiments (Figure 36b and 37), this suggests that the Δrhs2 rhs1 1323::stop strain was responsible for the difference in CI results. A speculative hypothesis could be that as there is a reduction in T6SS firing in Δrhs2 rhs1 1323::stop compared to WT, as shown by Hcp secretion in the supernatant (Figure 36a), this could cause more variable inhibition dependent subtle differences in growth conditions in different experiments. Although the differences in CI results between experiments are not fully understood, Δrhs2 rhs1 1323::stop was used for further experiments. This strain was chosen as it has the greatest reduction in CI compared to WT with MG1655, which is the target strain that was used for further experiments. Δrhs2 rhs1 1323::stop was used to see if differences in inhibition levels can be picked up in single cell microscopy and in microcolony growth compared to WT. Δrhs2 rhs1 1323::stop will subsequently be abbreviated to Δrhs2 rhs1$^{\text{tr}}$.

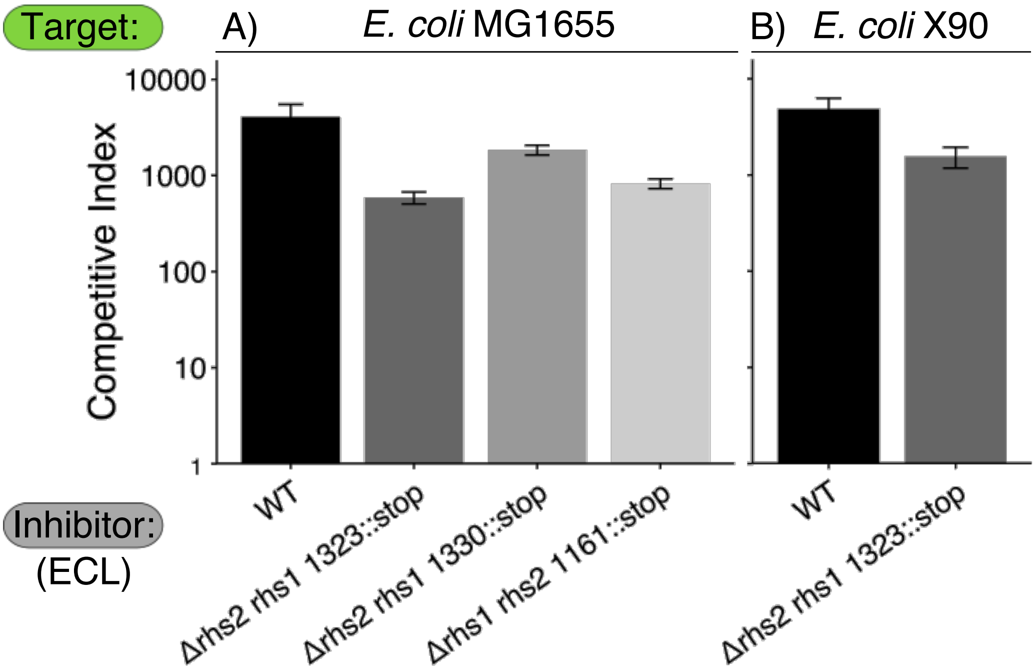

Figure 37: **Rhs effector mutants show reduced CI compared to ECL WT with *E. coli* MG1655 as a target.** A) Using *E. coli* MG1655 as in previous competitions, three strains with the biggest reduction in CI [84] (Figure 36) were tested. WT CI is comparable to results from Donato et al. [84]. Δrhs2 rhs1 1323::stop, Δrhs2 rhs1 1330::stop and Δrhs1 rhs2 1661::stop have a reduction in CI compared to WT but the reduction is not as strong as seen by Donato et al. [84] (Figure 36). n = 4-6. B) Δrhs2 rhs1 1323::stop was competed against *E. coli* X90 (strain used by Donato et al. [84]). These competitions did not show the same reduction in CI as seen by Donato et al. [84]. n = 3. Error bars show SEM.

6.2.2 Using single cell microscopy to measure differences in inhibition rate

Imaging the cells at high magnification throughout a time-lapse allows single cells to be tracked as they come into contact, allowing growth rate of target cells upon contact with inhibitor cells to be measured. In previous analysis (Chapter 3) the inhibition was looked at by tracking the number of divisions of target cells after contact with inhibitor cells in a given time frame using only contacts that were made before the start of acquisition. This showed a clear reduction in the number of divisions of target cells after contact with T6SS inhibitor cells. More information on the rate of inhibition can be gained by defining when cells stop growing, allowing a time to be measured from contact to growth arrest. Using a DNA stain, SYTOX Blue, cell membrane permeabalisation can be visualised [128]. The uptake of SYTOX Blue can be used to show when cells stop growing which can indicate cell growth arrest. However, this is not to rule out that growth arrest could occur without SYTOX Blue uptake, depending on the type of toxins present. Using time-lapse microscopy and SYTOX Blue staining, the T6SS activity of Δrhs2 rhs1^{tr} (T6SS effector mutant) and WT (T6SS+) inhibitor strains was compared.

Two measurements were taken to show the effect of the toxins on target cells: 1) The number of cell divisions of the target cell after contact with the inhibitor before SYTOX Blue uptake (Figure 38a): 2) The killing time (KT), defined as the time from target cell contact with inhibitor to SYTOX Blue uptake by the target cell (Figure 38b). SYTOX Blue was used as this nucleic acid stain has been previously used in similar T6SS killing experiments with no adverse effects on cell growth reported [128].

In single cell microscopy experiments, some target and inhibitor contacts were made before the start of the time-lapse. This means the contact was made in the 30 minutes between inoculating the agarose pad with the competition mixture and the start of imaging. Due to this, the KT of these contacts cannot be used, but the divisions can be counted if it is clear that the cell in contact has not divided. It cannot be proven that the target and inhibitor cells did not make contact in the solution before plating on the agarose pad, however all cells are subject to that possibility.

With WT the majority of target cells did not divide after contact with inhibitor cells, with only 22.6% of target cells dividing once or more after contact (Figure 38a). Cells that did divide did so soon after contact, as seen in Figure 39. In comparison, 72.4% of target cells in contact with Δrhs2 rhs1^{tr} inhibitor cells divided and underwent up to six cell divisions between contact and SYTOX Blue uptake (Figure 38a). Figure 40 shows target cells that continue to divide even after early contact with inhibitor cells. More target cells continue to divide once in contact with Δrhs2 rhs1^{tr} inhibitors cells than once in contact with WT inhibitor cells, which suggests that the toxin activity is slower to take effect or that the cell's growth once intoxicated is higher in Δrhs2 rhs1^{tr} compared to WT. The KT can give infomation on how fast it takes for the toxins to take effect.

There is a significant difference between the target cell KT with WT compared to Δrhs2 rhs1^{tr} inhibitor cells (Figure 38b). The KT for WT is faster with an average of 37 minutes compared to an average of 76 minutes with Δrhs2 rhs1^{tr}. The range of KTs is larger for Δrhs2 rhs1^{tr} than for WT.

To investigate the reason for the higher variability in KT with Δrhs2 rhs1^{tr}, the data points were split by when in the time-lapse the contact was made. The time that contact was made was split into three phases: early (contact made in 0-90 minutes), mid (96-180 minutes) and late (186-270 minutes). The group of target cells that have a slower killing time, with Δrhs2 rhs1^{tr} inhibitor, made contact in the early phase of the time-lapse (Figure 38b). Late phase contacts with Δrhs2 rhs1^{tr} inhibitors kill target cells faster with the maximum KT for later contacts being 78 minutes (just above the average KT). WT does not show a difference in KT dependent on time of contact. This faster KT later in the time-lapse could be due to environmental stresses on the target cell, such as reduction in nutrients and O_2.

To see if environmental factors are a reason for faster KT, the times of cell deaths for target cells not in contact with inhibitor cells and inhibitor cells were plotted (Figure 41). From 60 minutes, some cells start to take up SYTOX Blue or lyse, with an increase in cell death without contact from 180 minutes (late phase). This increase in cell death later in the time-lapse suggests that the cells are subject to more environmental stress which may affect their sensitivity to toxin affects. Interestingly most cells that lysed without contact were inhibitor cells not target cells. A possible reason for this is that MG1655 is better adapted to laboratory growth conditions that ECL, which is in line with limited growth of ECL under the microscope in preliminary experiments (data not shown). These results do not mean this conclusion is invalid, but this data does not fully answer the question as to why Δrhs2 rhs1^{tr} inhibition is more affected by the time the contact is made than WT inhibition is.

Increased number of divisions after contact with inhibitor cells and increased KT suggest that Δrhs2 rhs1^{tr} has a reduced inhibition potency compared to ECL WT. Previous data shows that reduction in inhibition levels could be due to both reduction of T6SS firing and fewer effectors present [84]. Δrhs2 rhs1^{tr} shows reduced Hcp levels in the supernatant compared to WT which suggests reduced T6SS assembly and firing (Figure 36a). Deletion of Rhs1 and Rhs2 leaves the action of two known toxins, Tae4, an amidase, and Tle1, a lipase and a toxin of unknown activity. Together these factors reduce the system potency in Δrhs2 rhs1^{tr} but is this through reduced inhibition rate or reduced toxicity (intoxicated growth)?

It can be hypothesised, due to Δrhs2 rhs1^{tr} take up of SYTOX Blue, that the toxicity of the system once the toxin activity takes affect is the same as T6SS. This is suggesting that it is reduced inhibition rate that reduces inhibition potency. This hypothesis can be confirmed through cell length tracking. Cell length tracking shows Δrhs2 rhs1^{tr} cells continue to grow exponentially then stop division and length expansion abruptly (Figure 42c and 42d). This is in comparison to T6SS where all target cells in contact with inhibitor cells do not continue to lengthen or divide (except very shortly after contact) and take up SYTOX Blue (Figure 42a and

42b). Interestingly this analysis showed that some target cells in contact with Δrhs2 rhs1$^{\mathrm{tr}}$ do not elongate or divide but also do not take up SYTOX Blue (Figure 42d).

The effector mutant Δrhs2 rhs1$^{\mathrm{tr}}$ shows reduced inhibition activity in population competitions and in single cell experiments compared to WT. This strain can therefore be used as an experimental example of intermediate inhibition potency. This can be used to validate model results of the effect of inhibition potency on microcolony spatial structure.

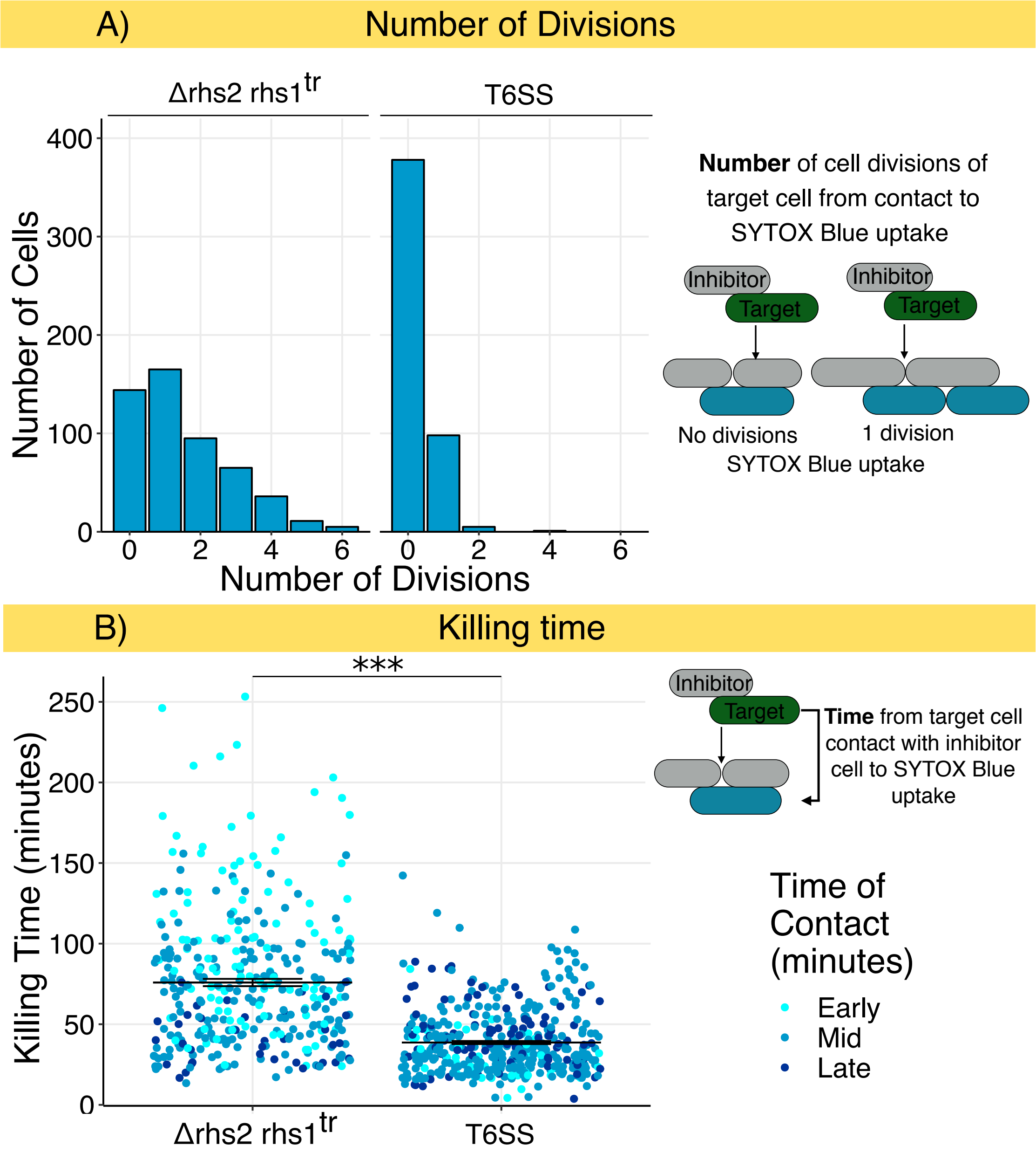

Figure 38: **Single cell microscopy shows the difference in inhibition between T6SS+ and T6SS effector mutant.** A) Number of target cell divisions from contact with an inhibitor cell to SYTOX Blue uptake. B) Killing time is the time from target cell contact with an inhibitor to target cell uptake of SYTOX Blue. The points are split by the phase of the time-lapse the contact is made: early = 1-90 minutes, mid = 96-180 minutes, late = 186-270 minutes. *** = $p < 0.001$ with one-way ANOVA. Data presented here for T6SS (WT) is the same data used in Chapter 5, Figure 26 but analysed taking into account SYTOX Blue uptake. Method outlined in Chapter 2.

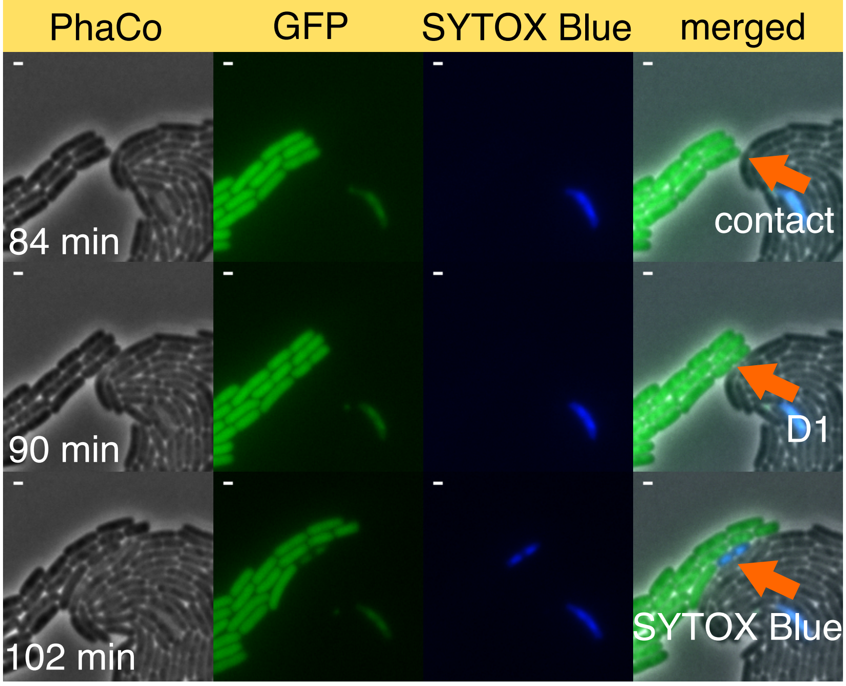

Figure 39: **Target contact with WT inhibitor that undergoes one division before inhibition with a killing time of 18 minutes.** Divisions are counted from when the target cell comes into contact with an inhibitor cell (top panel) to when the target cell takes up SYTOX Blue (lower panel). This cell that has taken up SYTOX Blue has gone through one division (middle panel). The time of contact (84 minutes) to the time of uptake of SYTOX Blue (102 minutes) gives a killing time of 18 minutes. As the contact is made at 84 minutes into the time-lapse this is in the early phase of the time-lapse. This is one example of 482 target cell contacts with WT inhibitor cells that take up SYTOX Blue. Scale bars correspond to 1 μm.

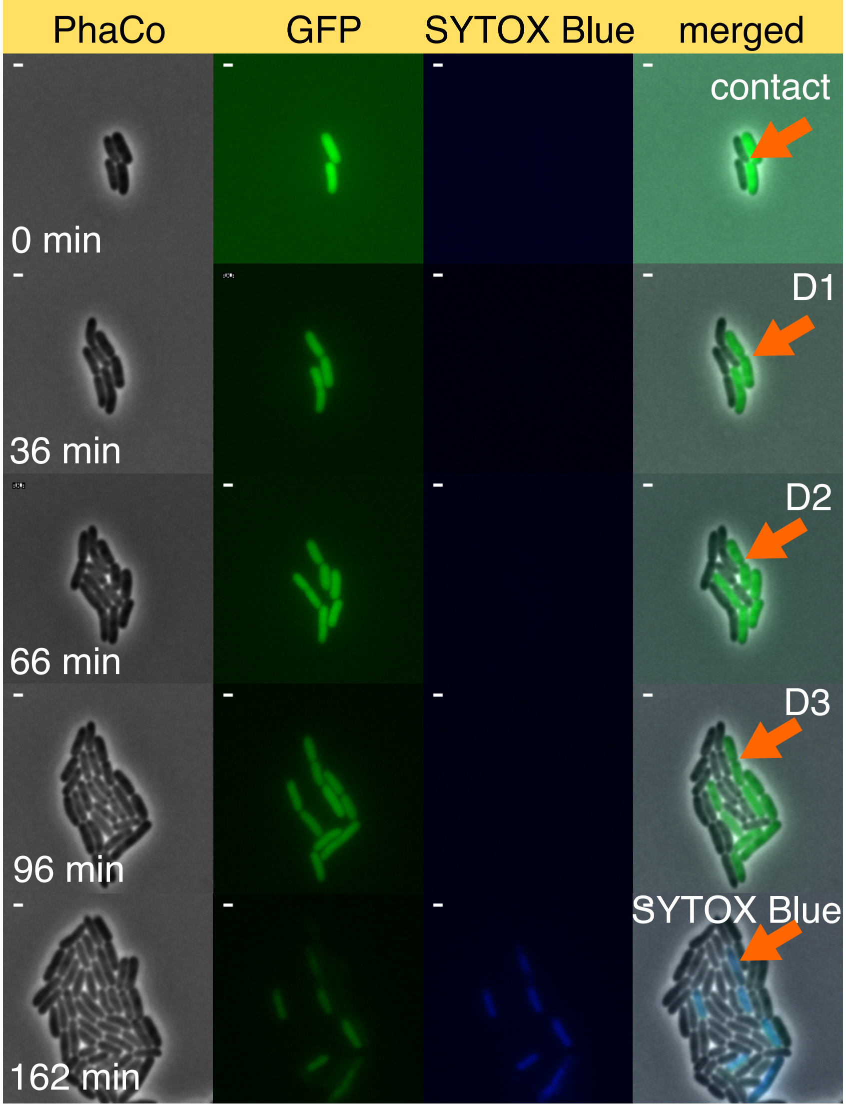

Figure 40: **Target contact with Δrhs2 rhs1^{tr} inhibitor that undergoes three cell divisions before SYTOX Blue uptake with a killing time of 162 minutes.** Divisions are counted from when the target cell comes into contact with an inhibitor cell (top panel) to when the target cell takes up SYTOX Blue (lower panel). This cell that has taken up SYTOX Blue has gone through three divisions (middle three panels). As the contact between target and inhibitor cell was made before the start of imaging, the killing time cannot be counted in the results but the number of divisions can. This is one example of 521 target cell contacts with Δrhs2 rhs1^{tr} inhibitor cells that take up SYTOX Blue. Scale bars correspond to 1 μm.

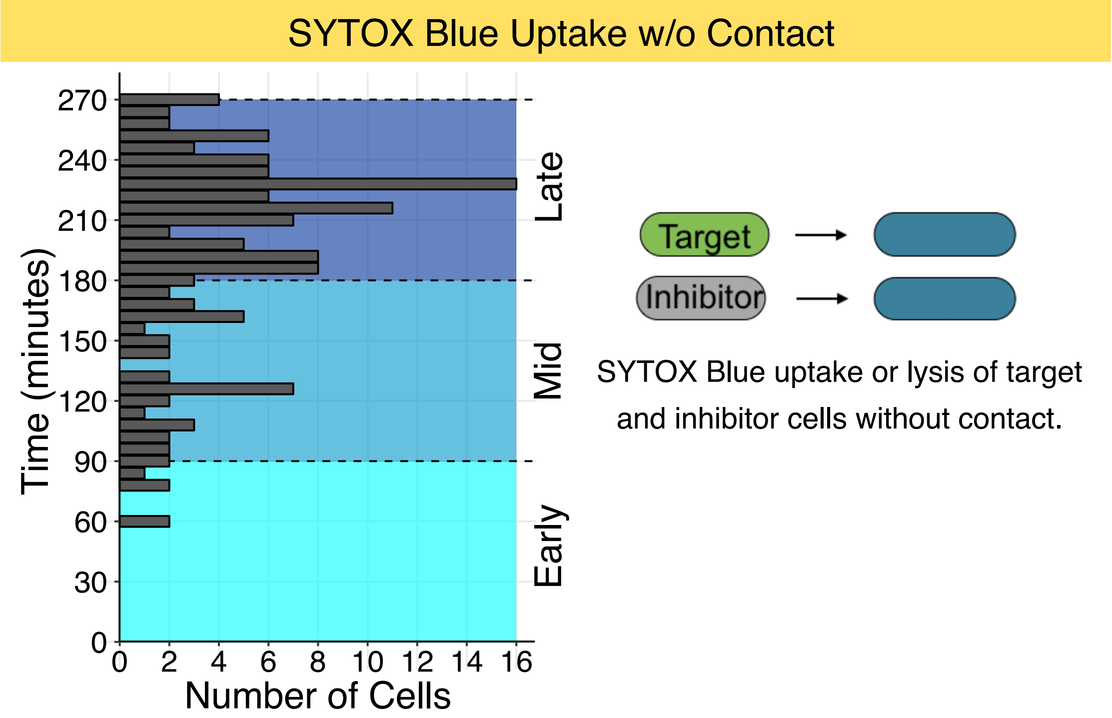

Figure 41: **Cells take up SYTOX Blue or lyse without inhibition from 90 minutes into the time-lapse.** Target and inhibitor cell microcolonies without contact with the other cell type were tracked over time and the frame in which SYTOX Blue stained the cells or the DNA released from lysing cells was stained, was counted. The results for target and inhibitor cells are combined in this graph. Shaded area shows the phases in which the cell takes up SYTOX Blue (early = 1-90 minutes, mid = 96-180 minutes, late = 186-270 minutes), with the majority are in the late phase (after 180 minutes).

6.2.3 Exploring inhibition potency in the individual based model

There are two parameters that were used to control inhibition in the model: the inhibition rate and the intoxicated growth rate of target cells. In single cell microscopy results just discussed, the reduced inhibition phenotype of Δrhs2 rhs1^{tr} shows a reduction in the speed of inhibition. This encompasses the rate of toxin insertion and toxin activity (Figure 38). The inhibited cells also stop growing, shown by cells that take up SYTOX Blue no longer dividing or elongating. This suggests that the Δrhs2 rhs1^{tr} has a reduced inhibition rate compared to WT, but like WT does not grow once intoxicated. This was also seen in cell length tracking analysis (Figure 42). These measurements cannot definitively conclude when the target cell becomes intoxicated and

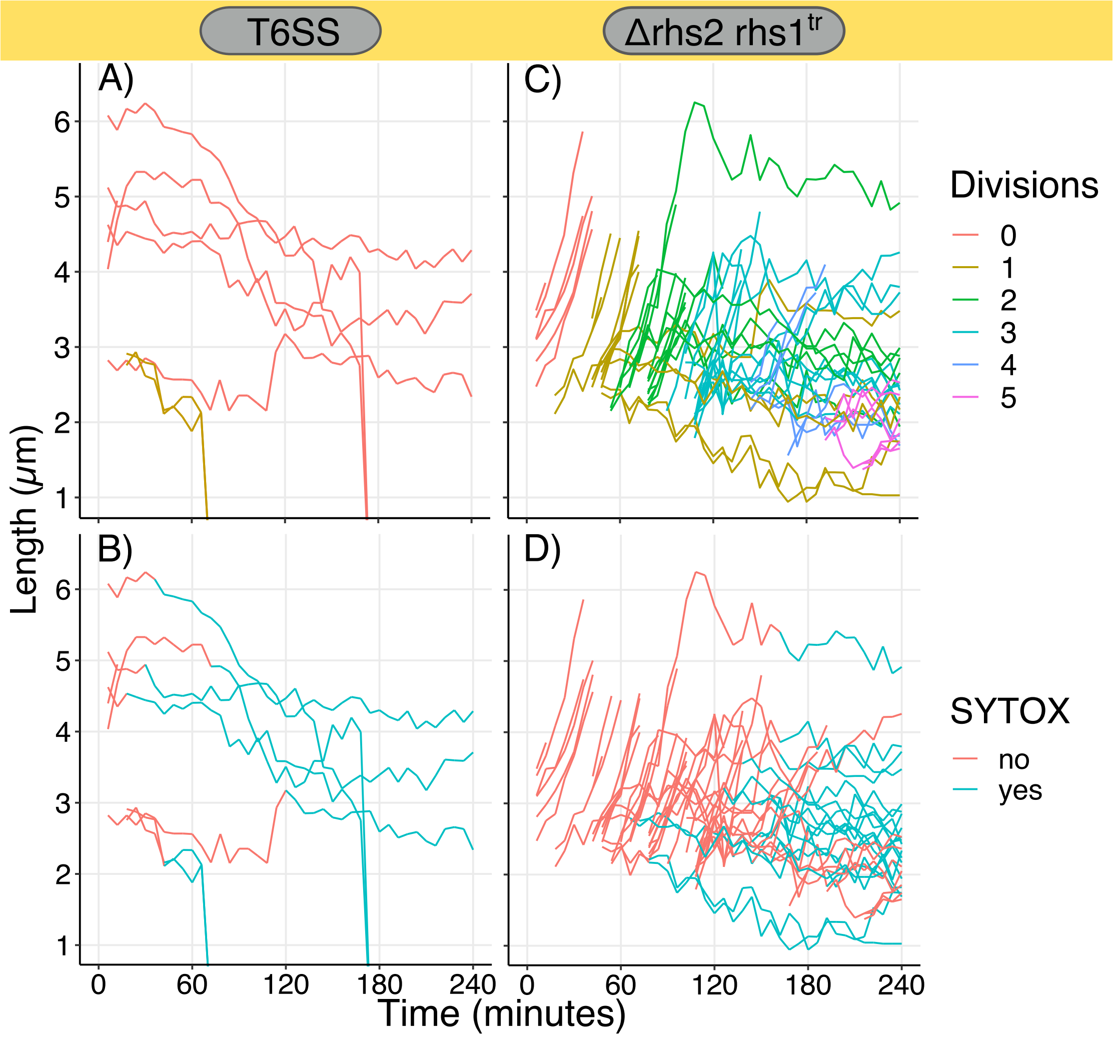

Figure 42: **Cell Length tracking shows high inhibition rate in both T6SS and Δrhs2 rhs1^{tr}.** Target cells in contact with inhibitor cells at the start of the time-lapse were tracked for four hours. Only target cells that maintained contact with inhibitor cells were included. A) T6SS (ECL WT) inhibition, graph coloured by number of divisions. B) The same data as A but coloured by when SYTOX Blue was taken up. C) Δrhs2 rhs1^{tr} inhibition, coloured by number of divisions. D) The same data as C but coloured by when SYTOX Blue was taken up. Three target-inhibitor interactions were tracked for each condition.

what the growth rate after intoxication is, but these predictions can be tested using simulation. Varying both inhibition rate and intoxicated growth rate of target cells can be used to investigate the dynamics of inhibition and how it lines up with single cell data.

The inhibition rate refers to the average number of toxin insertions per hour per cell (h^{-1} $cell^{-1}$). This is a propensity which is controlled in the model by the Gibson-Bruck algorithm [101]. Based on the results from simulations in Chapter 5, inhibition rates between 0.1 and 1 were used. The intoxicated growth rate refers to the rate of target cell growth after contact and inhibition, by inhibitor cells. The range of values used was 0% growth (0 h^{-1}) to 25% growth (0.27 h^{-1}) compared to base growth (1.06 h^{-1}). To compare outputs from the model to single cell data, the number of divisions of target cells in contact with inhibitor cells was counted, as well as the time from target cell contact with inhibitor cell to inhibition (killing time).

The full range of simulations (Figure 43) shows the effect of increasing inhibition rate and reducing intoxicated growth rate. With increased inhibition rate the distribution of divisions goes from spread out to clustered. With total inhibition of growth (intoxicated growth = 0%) the number of divisions of target cells is clustered around zero. With low inhibition rate some cells are inhibited fast and some are inhibited slower giving a spread of divisions, whereas with high inhibition all cells are inhibited quickly before they can divide. As cells are inhibited before they can divide and do not divide once inhibited, this also leads to fewer cells being counted with high inhibition rate and low intoxicated growth.

With WT (T6SS+) the majority of cells do not divide once in contact, with a few cells dividing more than zero times. An inhibition rate of 0.5 h^{-1} $cell^{-1}$ and intoxicated growth of 0% gives a distribution of cell divisions very close to that seen in the single cell data for WT (Figure 44 right panels). This backs up the data from Chapter 5, Figure 26, showing that with the T6SS the inhibition rate is fast and cells no longer grow once intoxicated.

Looking down the intoxicated growth axis, the distribution of divisions follows the same trend for each inhibition rate (spread for low inhibition rate and clustered for high inhibition rate) but the number of divisions shifts to higher numbers as the intoxicated growth increases. This is because cells that are still growing to some extent after inhibition will continue to divide, albeit at a slower rate.

Δrhs2 $rhs1^{tr}$ shows a distribution of divisions clustered around one with a tail off up to six divisions. This fits well to simulations with inhibition rate = 0.2 h^{-1} $cell^{-1}$ and intoxicated growth = 10% of base growth (0.11 h^{-1}) (Figure 44 left panels).

The killing time can also be compared between microscopy and simulations. However, killing time is only relevant with inhibition rate perturbations, not with intoxicated growth rate changes.

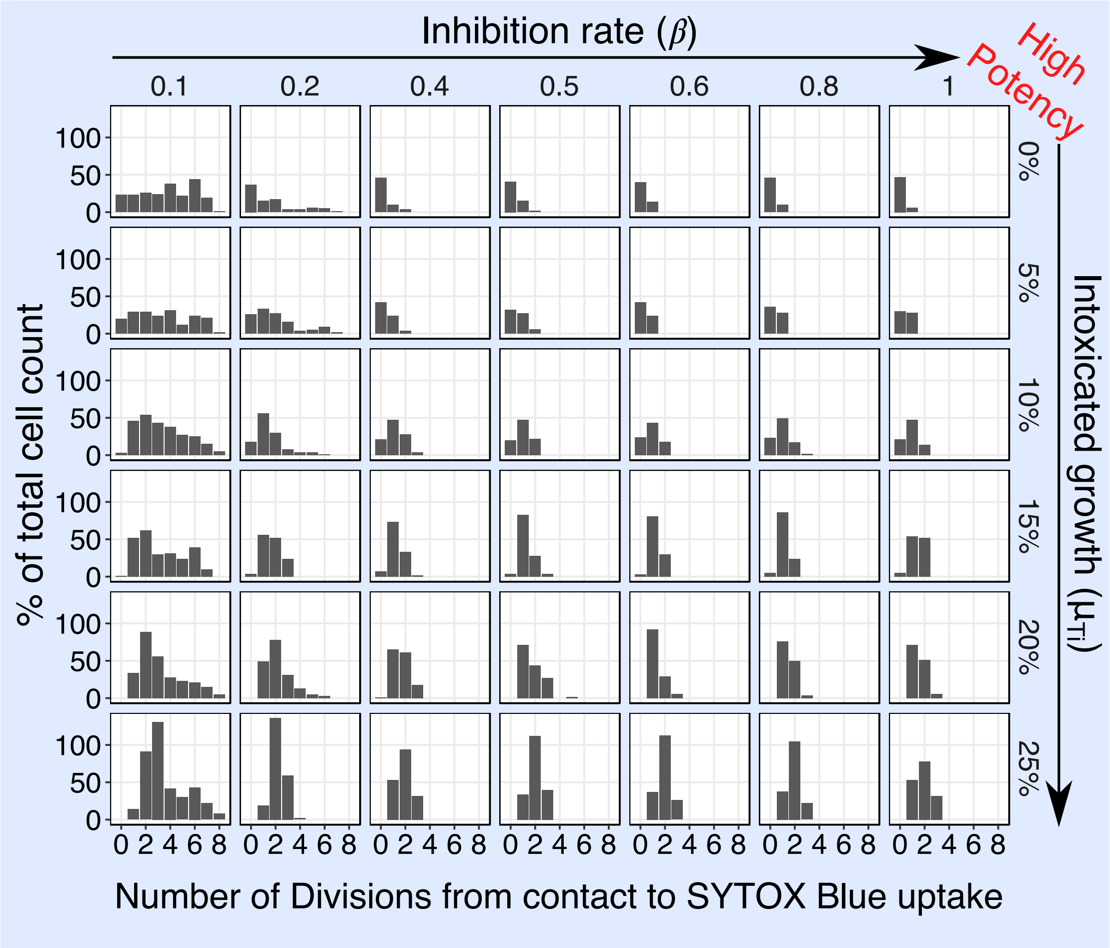

Figure 43: **Simulations show how the number of cell divisions of target cells change with small incremental inhibition rate and intoxicated growth rate perturbations.** The number of cell divisions of target cells that have stayed in contact with inhibitor cells and taken up SYTOX Blue. Contact was made at any point in the 240 minute time frame. This is the same protocol used in microscopy to measure divisions. Divisions are plotted as a percentage of the total cells counted in that simulation. Inhibition rate is varied from 0.1 to 1 insertions h^{-1} cell^{-1}. Intoxicated growth is given as a percentage of base growth (measured from not in contact target and inhibitor cells and calculated in Chapter 3, Figure 24 as 1.06 h^{-1}) so 0% is a growth rate of 0 h^{-1} etc.

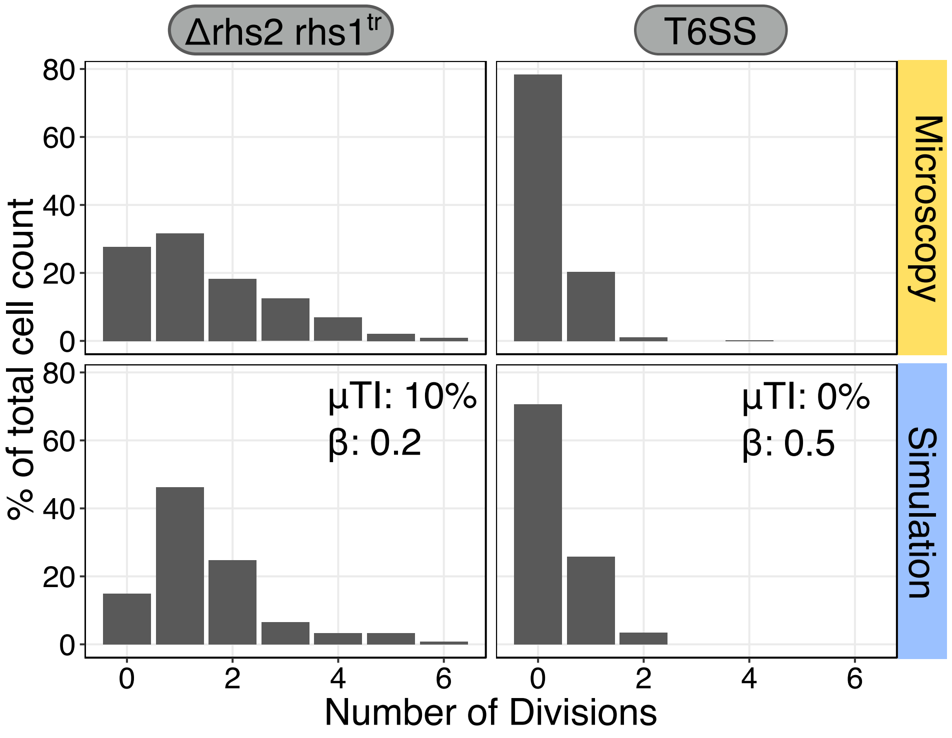

Figure 44: **Simulations show similar division dynamics to microscopy results for WT and Δrhs2 rhs1$^{\mathbf{tr}}$.** Top panel shows microscopy results for Δrhs2 rhs1^{tr} and WT (T6SS). Microscopy data presented here for T6SS (WT) is the same data used in Chapter 5, Figure 26 but analysed taking into account SYTOX Blue uptake. Method outlined in Chapter 2. Bottom panel shows simulations that are T6SS-like and Δrhs2 rhs1^{tr}-like. μTI = intoxicated growth as % of base growth (1.06 h^{-1}). β = inhibition rate h^{-1} cell^{-1}.

This is because the killing time measures the time from target cell contact with an inhibitor to SYTOX Blue uptake and was the same independent of what the growth rate of the intoxicated cell is (simulation data not shown). Therefore, only the killing time results from simulations with an intoxicated growth of 0% are presented here (Figure 45).

There is a large change in KT distribution between inhibition parameters of 0.1 and 1.0 toxin insertions h^{-1} $cell^{-1}$ (Figure 45). With an inhibition rate of 0.4 h^{-1} $cell^{-1}$ and higher, the average KT is less than 10 minutes. This is relatively fast, especially compared to microscopy results where it is faster than WT average killing times (Figure 38b). This seems to be a saturation point where faster inhibition gives similar average killing times. The average KT for an inhibition rate of 0.1 h^{-1} $cell^{-1}$ is 138 minutes but the distribution is very wide. This is also seen in microscopy data for Δrhs2 $rhs1^{tr}$ (Figure 38b). The killing time for Δrhs2 $rhs1^{tr}$ best fits again to a inhibition rate of 0.2 h^{-1} $cell^{-1}$, whereas the killing time for WT is not as fast as 0.4 h^{-1} $cell^{-1}$ and above.

To summarise the results from simulations, simulation data points that fit well to single cell microscopy data for Δrhs2 $rhs1^{tr}$ and WT can be found. The microscopy single cell data is compared to equivalent outputs from simulations run with a range of parameters. Based on cell division counts, the simulations that fit WT data best are an inhibition rate of 0.5 h^{-1} $cell^{-1}$ and intoxicated growth of 0%. This is in line with the observation that target cells no longer grow after contact with WT inhibitor cells. The KT data from simulations does not fit so well to WT single cell data with the simulations showing faster KT. For Δrhs2 $rhs1^{tr}$ the simulations that fit the single cell data best are inhibition rate of 0.2 and intoxicated growth of 10%. This is in line with predictions from single cell data that the inhibition rate for Δrhs2 $rhs1^{tr}$ is slower that for WT. However, it was not expected that the intoxicated growth for Δrhs2 $rhs1^{tr}$ would be higher than for WT. These parameters were used in microcolony simulations and compared to microscopy microcolonies using the fractal dimension.

6.2.4 Visualisation and quantification of microcolony spatial structure in microscopy and simulations

Single cell analysis has shown that simulations can imitate the inhibition dynamics of microscopy results for T6SS and the effector mutant strain Δrhs2 $rhs1^{tr}$. In this section the hypothesis that proposes, simulation microcolony structures can be statistically comparable to the microcolonies seen under the microscope with intermediate inhibition, was tested. This hypothesis was tested using the same parameters explored in single cell simulations. If microscopy and simulations give consistent results, this can validate the trends seen in simulations.

There is a significant difference in inhibition seen at a single cell level between ECL WT

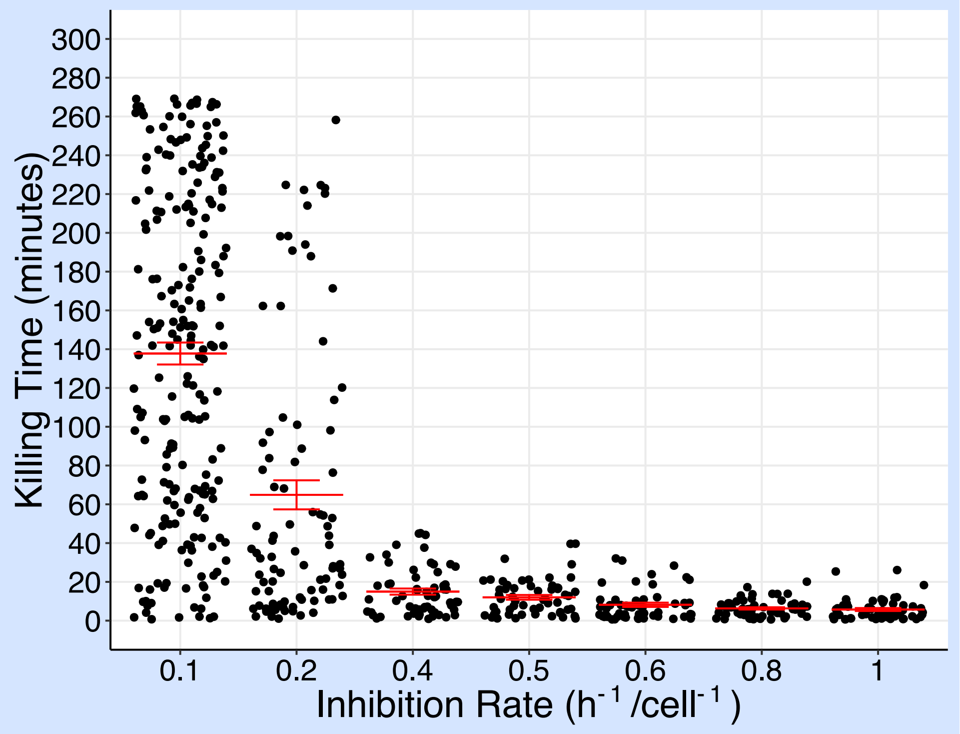

Figure 45: **Simulations show a large reduction in killing time within a small range of inhibition rates.** Points represent the KT of target cells, which is calculated from when they come into contact with an inhibitor cell to when they become inhibited. Simulations were ran for 240 timesteps, which is equivalent to four hour experiments. Intoxicated growth rate = 0%. Error bars show SEM.

and ECL Δrhs2 rhs1^{tr}. To see the effect of the reduced inhibition of Δrhs2 rhs1^{tr} on spatial structure, microcolony images were analysed. Competitions were imaged after four hours growth on agarose pads, when the field of view has become confluent with cells (135 μm^2 area). Figure 46 shows three examples of WT (T6SS+), Δrhs2 rhs1^{tr} (T6SSS effector mutant) and Δvask1 (T6SS-) colonies, each tracked over time. Differences in control and T6SS strains can be seen. In control images there are large areas of target cell growth, and target and inhibitor patches are well dispersed. With T6SS, target cells are clustered and inhibitor cells dominate the field. With Δrhs2 rhs1^{tr} some target cell clustering is seen but not as drastically as with T6SS. Figure 47 shows simulation images at T = 4 hours. There is no clear visual differences in simulation images between control and T6SS-like/Δrhs2 rhs1^{tr}-like microcolonies. Statistical analysis of the spatial patterns created can be used to measure subtle structural differences in microcolonies.

The fractal dimension (Fd) is calculated to measure the structural changes in microcolony images (Figure 48). The simulation Fd follows the same trend as the microscopy results: as inhibition potency increases the Fd decreases. With both control and Δrhs2 rhs1^{tr} the Fd is not significantly different between simulation and microscopy. However, the main difference is in T6SS-like simulations compared to T6SS microscopy microcolonies. The Fd values are higher for simulation images than microscopy images. This could be due to small clumps of inhibited target cells being lost to 3D growth in microscopy but still being present in simulations as the growth is in 2D (as discussed in Chapter 5). In microscopy four hours of growth is needed to get large areas of confluent cells, but some cell patches grow into 3D when there is a high density of cells in one area. For simulations the results are less spread out both across strains and within strains compared to microscopy. Microscopy images show a larger within group variation of Fd.

Varied structures within groups may be due to inoculum density differences. Previously density dependence in simulations has been shown (Chapter 5). The number of cells seeded at the start of imaging was counted from microscopy and used to parameterise the simulation. Figure 49 shows the start seeding of four repeats for both microscopy and simulations. The main difference is clumping of cell types in microscopy but not in simulations. When counting the number of cells, clusters were counted as one. This could be a difference that affects Fd variation. Clusters were counted as one so as to not overestimate the number of cells in microscopy. This could lead to larger patches being formed faster which could alter the overall structure, specifically reducing the Fd by creating larger patches which therefore can give reduced interaction surface between cell types.

In summary, in this chapter the T6SS effector mutant Δrhs2 rhs1^{tr} has been shown to experimentally exhibit intermediate inhibition. Inhibition with Δrhs2 rhs1^{tr} inhibitor cells shows

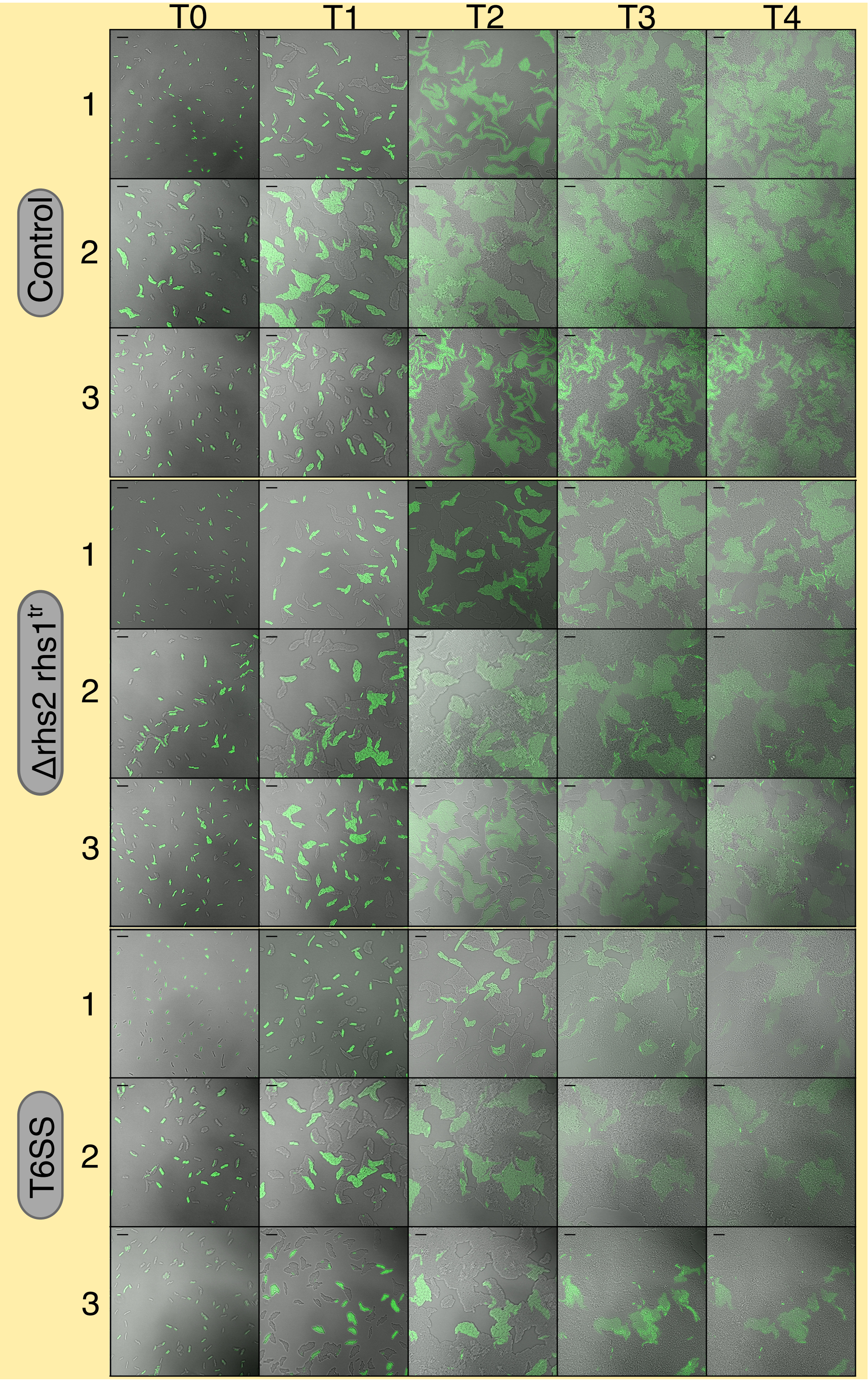
T0
T1
T2
T3
T4
Control
1
2
3
Δrhs2 rhs1tr
1
2
3
T6SS
1
2
3

lower Fd values than with control inhibitor cells which indicates it is reducing the interaction border between cell types. This finding validates the simulations results that show reduced Fd with increased inhibition (Chapter 5, Figure 29).

Figure 46 *(preceding page)*: **Confocal images show varied colony structure.** Three example of colonies for ΔT6SS control, WT (T6SS) and Δrhs2 rhs1^{tr} from three independent experiments. Snapshots were taken every hour for four hours (T0-T4 = 0 hours to 4 hours) to show the start seeding density for each end point. Target cells (green) = MG1655-gfp, inhibitor strains are untagged ECL (grey). Scale bars correspond to 1o μm.

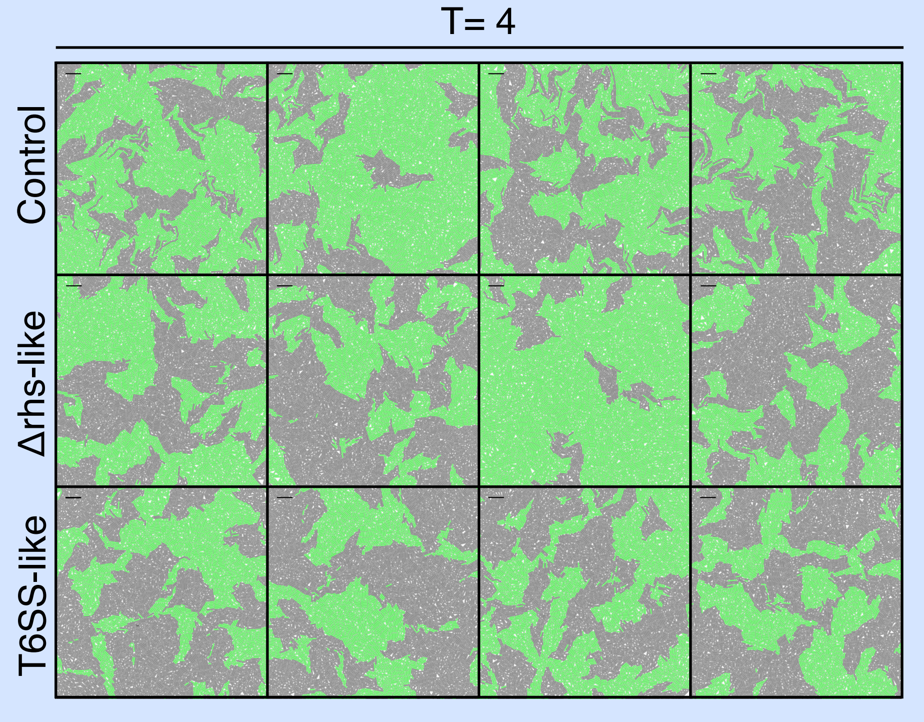

Figure 47: **Simulation colony structure between strains is not clear through visual observation only.** Four repeat simulations at time (T) = 4 hours for T6SS-like, Δrhs2 rhs1^{tr}-like and control. Target cells = green, inhibitor cells = grey. Scale bars correspond to 10 μm.

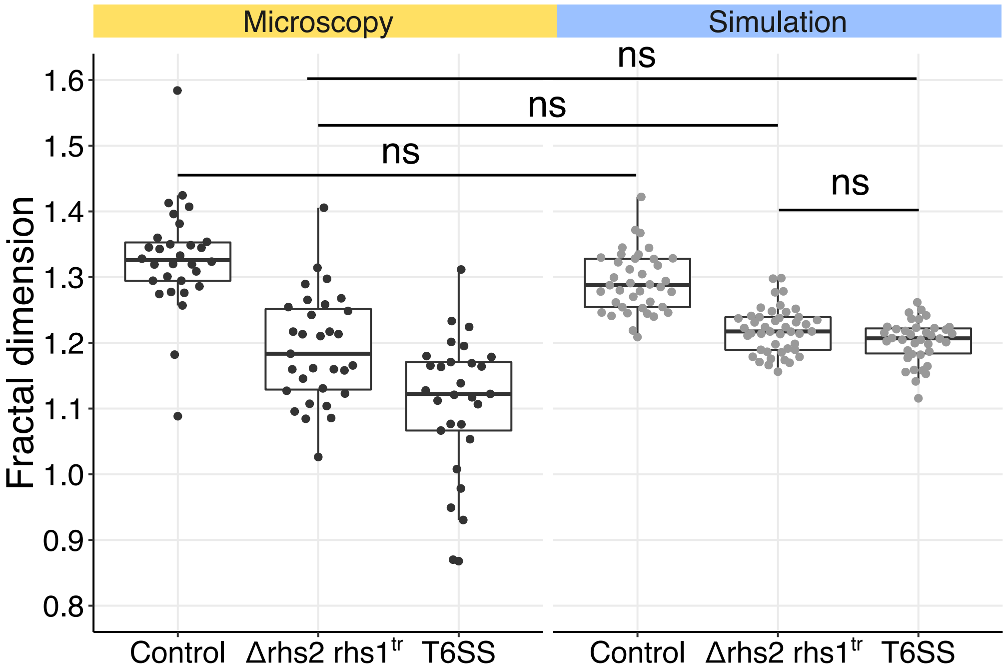

Figure 48: **Fd for simulation and microscopy microcolonies shows decrease as inhibition increases.** A) Fd for microscopy microcolonies. n = 30-40 images. Fd drops with WT compared to control. Δrhs2 rhs1^{tr} is significantly different from WT. B) Simulation shows reduction in Fd with increase in inhibition. Statistical analysis with one-way ANOVA and post-hoc Tukey's test. All pairwise tests not marked show ***p < 0.001 significance, ns = not significant. Data presented here for T6SS (WT) and control is the same data used in Chapter 5, Figure 30 and Figure 31.

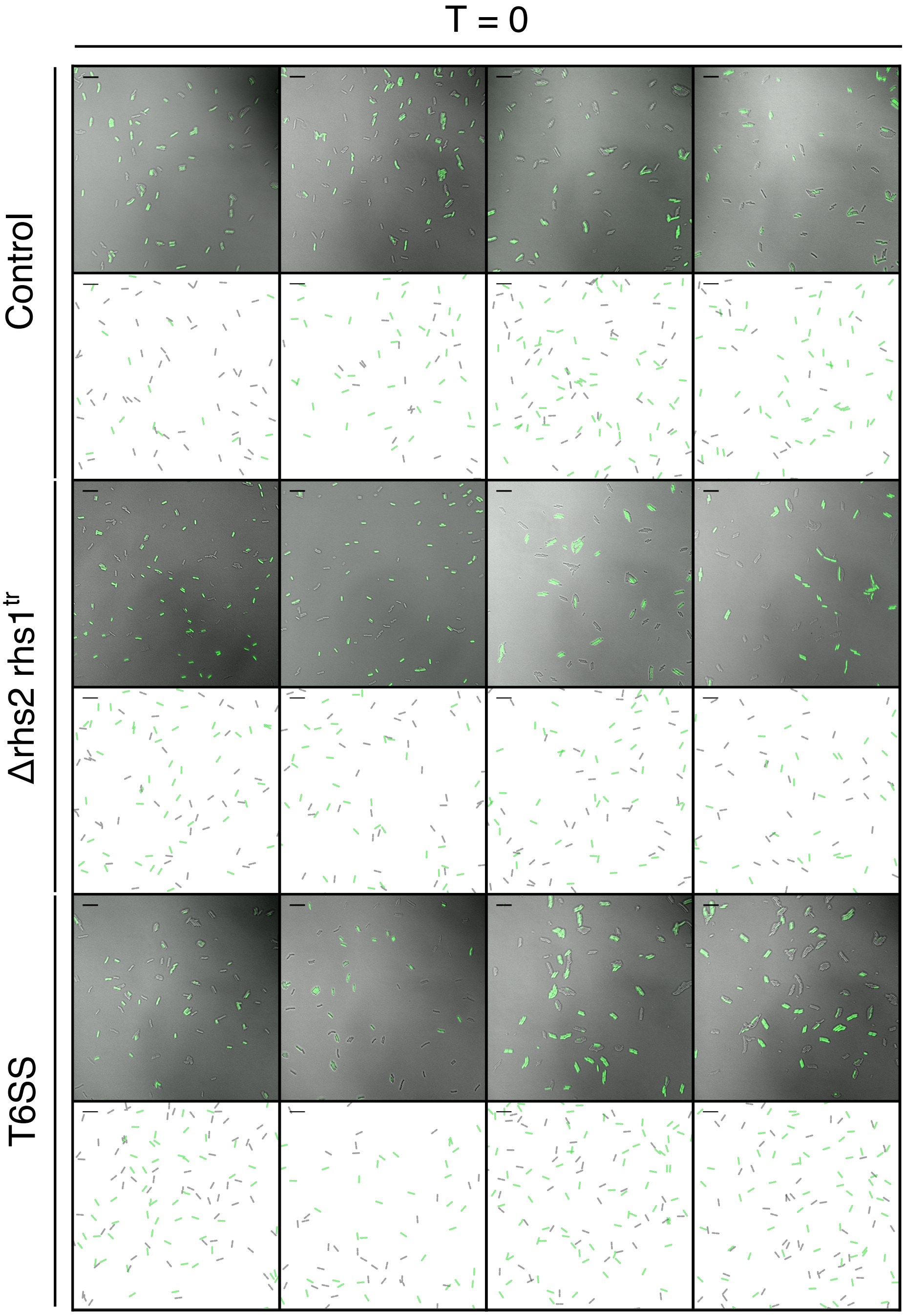
T = 0
Control
Δrhs2 rhs1^{tr}
T6SS

6.3 Discussion

The aim of this chapter was to validate findings on single cell dynamics and microcolony structure from simulations (Chapter 5) by identifying a T6SS effector deletion strain that shows intermediate inhibition potency. A strain was identified that shows lower inhibition than ECL WT in single cell analysis. The Fd was then used to compare experimental and simulated microcolony structure. Measuring the structural effects of inhibition at the border between cell types using the Fd shows no significant difference in microcolony structure between the microscopy and simulation data. These finding that show the structural findings in microscopy can be captured in simulations show the effectiveness of an experimental and simulation iterative approach. Using parameters from microscopy has allowed simulations to give greater information on details of inhibition that cannot be fully defined from experimental work.

To discuss how simulation results were successfully validated by an intermediate inhibition strain simulation results from Chapter 5 will be summarised. In simulations, inhibition potency (defined by two parameters, inhibition rate and intoxicated growth rate) was varied so that trends in inhibition and the effect on spatial structure could be identified. It was seen that decreasing inhibition potency decreased the Fd of the resulting microcolony growth when target and inhibitor cells were grown together. This reduced Fd shows that the interaction border of the target and inhibitor cells was decreased and this amounts to target cell clustering. To justify these trends from simulations, experimental data points that fit the extremes (high potency inhibition/no inhibition control) and an intermediate inhibition potency strain were used.

ECL WT was used as an example of high potency. Results in Chapter 3 showed inhibition with T6SS led to the majority of cells not dividing after contact, suggesting that the inhibition was both fast (high inhibition rate) and highly toxic (low intoxicated growth rate). This result was repeated with simulations in this chapter but using inhibition parameters with smaller increments being tested. This shows similar single cell dynamics to simulations with 0% intoxicated growth and an inhibition rate of 0.5 h^{-1} $cell^{-1}$. Previously, it has been shown that T6SS causes potent

---

Figure 49 *(preceding page)*: **Simulation and microscopy start images show similarity in numbers of cells but simulations are lacking the cell clumping seen in microscopy.** Four images for each strain and equivalent simulation at T = 0. Target cells (green) = MG1655-gfp. Inhibitor strains are untagged ECL (grey): control = ECLΔVask1, Δrhs2 rhs1^{tr}, T6SS = ECL WT. Scale bars correspond to 10 μm for both microscopy and simulation images.

killing of target cells [88, 89, 128]. In these studies lysis has been used for quantification but other facets such as speed of killing have not been quantified. Ringel et al. [128] showed in *Acinetobacter baylyi* the speed of toxin action of certain effectors have a slower effect than others ranging from less than ten minutes to more than forty minutes. This suggests that deletion of certain effectors can reduce the overall inhibition rate more than others. The functions of deleted toxins in T6SS effector mutants used as intermediate inhibition strains should therefore be kept in mind, this is discussed below.

A T6SS effector mutant, Δrhs2 rhs1$^{\mathrm{tr}}$, had the biggest reduction in inhibition compared to WT in population competition with *E. coli* MG1655 as a target strain. Δrhs2 rhs1$^{\mathrm{tr}}$ has the function of two out of five identified ECL T6SS toxins deleted. The reduction in CI with Δrhs2 rhs1$^{\mathrm{tr}}$ was 10-fold lower than with WT (T6SS+). CI is a measure of overall inhibition in the population and does not give any detail on the dynamics of inhibition. Interestingly the CI with Δrhs2 rhs1$^{\mathrm{tr}}$ is similar to the CI seen with CDI (Chapter 3). However, the inhibition with Δrhs2 rhs1$^{\mathrm{tr}}$ is more potent than CDI at single cell level (discussed in main discussion: Chapter 6.3).

To be able to give more detailed analysis of inhibition potency in single cell microscopy two measurements: the number of divisions and killing time, have been developed in this chapter to quantify inhibition. These measurements can also be used on simulation outputs for comparison. For both these measurements the contact time and a measurement for when the toxin effect is seen is needed. In microscopy SYTOX Blue was used as a readout for cell permeabalisation, this can be linked to cell death [128] but it does not mean that all cells that die will take up SYTOX Blue, as was shown with Δrhs2 rhs1$^{\mathrm{tr}}$ in cell length tracking. The killing time is the rate at which the toxin effect is seen in the target cell to stop its growth. This can inform the rate of inhibition parameter in simulations as the speed at which killing is seen is dependent on the speed at which the inhibition takes place, even though there are many factors involved in this that cannot be measured e.g. rate of insertion, rate of toxin action etc. Counting the number of divisions of a target cell in contact with inhibitor cells could show both the rate of inhibition or the extent of growth rate reduction (intoxicated growth). It is not clear from just quantifying the number of divisions whether the target cell is slowly growing or taking longer to stop growing completely. Both use of simulations and looking at cell length change over time could give more information on this. Cell length tracking showed that target cells grew exponentially for one or two rounds of divisions then stopped dividing and elongating, this suggests a reduced inhibition rate. Results from simulations are described in the next paragraphs.

With single cell microscopy showing Δrhs2 rhs1$^{\mathrm{tr}}$ has reduced inhibition compared to WT, simulations can then be used to understand the parameters that define the reduced inhibition in Δrhs2 rhs1^{tr}. A range of simulations with smaller parameter increments than in Chapter 5 were explored, with the aim to find a better fit to experimental data. It is possible to calculate a rate of inhibition from the killing times measured, however the effect is on each target cell and this could be caused by contact with multiple inhibitor cells. In contrast, in simulations the inhibition rate was given as the probability of the inhibitor cell attacking. For the reason that KT measures the rate of target cells being attacked and the inhibition rate in simulations defined the rate of inhibitors attacking, the inhibition rate was varied and the outputs compared to microscopy results. Killing time in simulations shows that the inhibition rate does not directly correspond to the inhibition rate in simulations. There is a drastic change in KT within a small range of inhibition rates, with the KT plateauing around 0.4 h^{-1} cell^{-1}. This could be through accumulation of multiple hits by different inhibitor cells in simulations. This could lead to a bigger effect being seen with a higher inhibition rate.

Comparing the cell division dynamics of Δrhs2 rhs1^{tr} to simulations shows that parameters that give similar dynamics are with intoxicated growth of 10% of base growth rate and an inhibition rate of 0.2 h^{-1} cell^{-1}. This suggests that the inhibition rate is reduced compared to WT but there is also some increase in intoxicated growth rate, suggesting that the target cells are continuing to grow slightly after intoxication. Higher intoxicated growth than WT is not expected from initial observations that Δrhs2 rhs1^{tr} inhibited target cells took up SYTOX Blue. This may be due to the toxin activity of the removed/remaining toxins.

The remaining toxins in Δrhs2 rhs1^{tr} are, Tae4, an amidase that breaks down the peptidoglycan cell wall [127], Tle1, a lipase that shows phospholipase activity to break down the cell membrane [125, 126] and a toxin of unknown function. The toxins also present in WT that Δrhs2 rhs1^{tr} is missing are Rhs2, a DNase and Rhs1, a nuclease. It is not clear why loss of nucleases but presence of membrane and cell wall degrading enzymes could lead to slower inhibition. The other difference in Δrhs2 rhs1^{tr} compared to WT is the reduction in firing of the T6SS. Work by Donato et al. [84] suggests that the Rhs toxins have a role is T6SS assembly in ECL. This can be seen from the data in Figure 36 where double Rhs deletion leads to no Hcp in the supernatant and CI similar to control. The various Rhs toxin truncations also have different levels of Hcp secretion. Δrhs2 rhs1^{tr} has some reduction in Hcp secretion and therefore this strain could have reduced T6SS firing. Less toxins entering the target cell could lead to the possibility of the cell not being completely killed and therefore a higher intoxicated growth rate.

One observation, in single cell results, is that Δrhs2 rhs1^{tr} KT is affected by the time at which the contact is made whereas WT KT is not. This could indicate that the speed of killing by toxins present is attenuated by cell stresses such as nutrient and 0_2 limitation. With WT, which has two nuclease toxins that Δrhs2 rhs1^{tr} does not, the nucleases in combination with the other toxins could act fast enough for the effects of stress not to be seen. The implication that stress of cells is involved in this difference was backed up by the observation that some cell death unrelated to contact takes place in the mid phase, 90-180 minutes, with an increase in the late phase, 180-270 minutes. Although more inhibitor cells lysed than target cells, it is still a valid conclusion that target cells are affected by environmental stress. With accumulation of stress from nutrient or 0_2 limitation later in the time-lapse, the additional stress of toxins could lead to faster SYTOX Blue uptake in target cells. However, these results do show that inhibitor cells are more affected by environmental stress than target cells when the additional stress of toxins is not present.

Finally, the microcolony structure in simulations and microscopy were compared. Comparing the Fd values between microscopy and simulations, the same trends can be seen with the Fd values decreasing as inhibition potency increases. However, the range of values with simulations were not as large as with microscopy, both between the different inhibition potencies and within the experimental repeats for a given condition. It was hypothesised that this was due to the seeding density but this had been input into the simulation. However, the cell clumping seen in microscopy was not implemented in simulations. It is possible that this could be added to simulations to see if this has a greater effect on variation of colony structure measured with Fd. Despite the range of microcolony structures in simulations not varying as much as in microscopy, the average Fd of both the control and Δrhs2 rhs1^{tr} are not significantly different to simulations. This is good evidence that the simulation trends can be used to understand structural changes due to inhibition potency. In microscopy, the Fd for WT and Δrhs2 rhs1^{tr} inhibition were significantly different however this was not captured in simulations. This could be due to the loss of small cell patches in microscopy due to 3D growth that did not happen in simulations (discussed in Chapter 5).

This chapter shows that manipulating inhibition using strains with fewer toxins can give intermediate inhibition (lower inhibition potency than WT but higher than control with no toxins). With these intermediate inhibition strains the experimental results were shown to fit with simulation results in terms of single cell growth rates and structural measurements. These results validate the trends seen in simulations when inhibition potency is varied more than can be easily done experimentally. Furthermore, the simulations can also be used to understand the single cell dynamics of experimental strains in greater detail, for example if inhibition rate or toxicity is the dominant inhibition parameter.

7 Summary and future work

T6SS and CDI inhibition at a single cell level has previously been visualised but the quantitative differences and the impact on spatial structure has thus far not been explored. The hypothesis driving this work asserted that the extent of inhibition with different contact inhibition systems would change the fine scale spatial structure of microcolony growth. Different inhibition dynamics in two contact inhibition systems, T6SS and CDI, were identified. The hypothesis was confirmed by showing the system with the highest potency, T6SS, had a more influential effect on reducing the intermixing of target and inhibitor strains, and a T6SS effector mutant showed an intermediate structural phenotype. The understanding of the varying patterns with altered potency was advanced in simulation parameter space exploration. This showed that the interaction border complexity was reduced in simulated microcolonies as the potency of inhibition was increased along two axes: inhibition rate and intoxicated growth rate. The CDI system was shown here to be low potency via both reduced inhibition rate and reduced toxicity. Heterogenic single cell effects were seen in microscopy analysis but a significant difference in structure could not be seen compared to the control. However, with Δrhs2 rhs1$^{\mathrm{tr}}$, a T6SS mutant where the function of two of the five known effectors were deleted [84], there was reduced complexity at the interaction surface between cell types compared to the control. Overall this work has shown that spatial patterning can be altered by the different inhibition potencies of contact inhibition systems.

In this work, a greater understanding has been gained of the effects different inhibition systems and their inhibition potency can have on single cell growth and spatial structure. The impact of gaining a greater understanding of the direct effects of individual strains, systems or effectors on single cell growth is a greater understanding of the inhibition landscape and the use of these systems in modifying, manipulating and synthesising microbial communities.

The reduction in intermixing of strains shown here creates local structure. Segregation and local structure are beneficial to drive stability in multispecies communities. Structure in communities is ultimately formed by growth and death [135], with antagonism being a method that creates space for growth. Toxin systems can inhibit and lyse cells for gain of nutrients or to create space for clonal expansion. It can be hypothesised that the micro-scale domains created by contact inhibition that have been identified here can be effective in creating the segregation needed for stability in larger populations. Ecological theoretical work suggests that competition stabilises diverse microbial populations such as in the gut [19], whereas too much cooperation can destabilise it [136].

In Chapter 3 different inhibition dynamics between T6SS and CDI were visualised and quantified in single cell time-lapse microscopy, using ECL as a model system. The T6SS, although showing potent inhibition within one cell division and uptake of a cell permeabilisation marker SYTOX Blue, did not show the phenotype of cell lysis seen in other species [89, 128]. This shows a different, strain specific T6SS phenotype to those so far visualised at a single cell level. This could be down to regulation and effector specific variables. The toxins that have been identified in T6SS and were present in the ECL effector mutant have been shown to cause lysis in some strains. To understand this, further investigation is needed to see if it is due to the effects of the quantity of the toxin. A combination of single cell and simulation analysis could prove a useful tool in the understanding of the effects of individual effectors. The impact of individual effectors could be investigated using cell length tracking to understand the inhibition dynamics of each effector. There are a diverse range of T6SS effectors, including several new effector families showing different inhibition phenotypes [53, 81, 137]. Recently a new family of T6SS effectors has been identified that are not bacteriolytic [81], with growth inhibition but not lysis being detected in *Serratia marcescens* intra-species competitions. This shows there is need for more detailed single cell analysis, as shown here, rather than quantification of cell lysis as previously used. There is scope for understanding the action of a diverse range of toxins, through techniques presented here. More details of these inhibition dynamics could also be added more precisely to simulations. For example, a ratcheting effect of accumulation of toxins could be included. Accumulation of toxins could be dependent on factors such as time, number of inhibitor cells and orientation of contact, until a threshold is reached after which inhibition can occur. This could help to explore the effects of multiple toxin insertion versus high toxicity. Using the power of computation, a greater basic understanding of the effects of toxin systems can be gained, such as if individual toxin toxicity or the amount of toxin is the dominant factor in potent inhibition.

In contrast to potent killing with T6SS, with CDI subtle and heterogenic inhibition was quantified. Sporadic growth inhibition had been seen by Bottery et al. [1] but the use of cell length tracking in this work gave a more detailed understanding of the heterogenic outcomes of individual cell growth. This analysis gave insight into the understanding that there are many variables involved in the overall inhibitory effects of a system. Due to low levels of toxin insertion or low toxicity of the toxin, only a small variation would cause outcomes to fluctuate. This is in contrast to the T6SS and Δrhs2 rhs1$^{\mathrm{tr}}$, which both have more consistent inhibition dynamics shown by cell length tracking.

Variables that can affect the outcome of CDI inhibition include: the expression of the CDI system, the number of CdiA proteins on the cell surface, the reloading of toxin systems on the surface once a toxin has been exported, the number of receptors on the target cell and inner membrane receptors, the localisation of CdiA on the surface and the cell orientation, and the number of toxins inserted into a target cell. Variation in these variables could lead to different inhibition dynamics. Questions such as the CdiA abundance and localisation on the cell surface and reloading of CdiA toxins have not been investigated. Using high resolution microscopy and fluorescent antibodies to the exposed domains of CdiA, it may be possible to visualise their localisation on the cell surface. Using genetic manipulation to alter *cdi* operon expression and cell length tracking measure the single cell inhibition effects, a greater understanding of the limiting factors of inhibition could be investigated. One example would be to overexpress the CDI system by varying inducer levels in an inducible system. As well as understanding the facets that affect natural toxin systems, the manipulation of toxin potency could be investigated with these techniques. Potency can be adjusted to do this, for example in a CDI system Chen et al. [138] showed that the inhibition potency of the toxin can be improved by removing some residues.

Gaining a more detailed understanding of how inhibition works gets us closer to being able to use these systems to manipulate microbial communities, for example deploying targeted toxin systems via probiotics to displace pathogens in dysbiotic systems or by arming commensals to resist pathogens. These are reported uses of contact inhibition systems in natural environments [68, 139–141]. One example is that the pathogen, *Burkholderia dolosa*, which can cause disease in CF patient, contain three CDI systems, which may provide a competitive advantage in infections [141]. Understanding the in vivo uses of contact inhibition systems is key to strain or community engineering. To achieve this, along with a better understanding of the binary interactions, competitive interaction in larger ecological systems will need to be tested.

In Chapter 5, using the single cell growth rates measured in Chapter 3 to parameterise an IMB of contact inhibition showed that the model could replicate single cell microscopy outputs. Through varying both the inhibition rate and intoxicated growth rate parameters, outputs that matched up to T6SS and CDI single cell data were identified. This gave insight particularly into the CDI heterogenic inhibition, providing further evidence to single cell results, that it is not only the reduced inhibition rate but also the reduced toxicity of the CDI system that causes the low potency inhibition. Simulations also provided the possibility to systematically investigate changes in structure with continuous changes in parameters, which through the use of a spatial statistical method, the Fd, showed small structural changes at the border between cell types.

Small scale structural changes can be effective in helping to stabilise communities, as shown by Liu et al. [142] who show in a four species synthetic community that antagonistic and mutualistic interaction increase biomass compared to communities with fewer species.

Structural analysis with the pcf did not show differences in low density competitions due to the range of interactions being too small. However, when the initial cell density was increased, inhibition imposed structure on the target cell population. This finding of imposed structure on target populations, though subtle in this investigation, poses some interest for interpreting the use of low potency toxin systems. This could be linked with the idea that contact inhibition systems act as kin recognition [46]. The evolutionary theory of contact inhibition systems being an example of a greenbeard allele has previously been suggested [143]. The protective effect of inhibition as a cooperative trait is dependent on carrying the inhibition system allele only. This is relevant in the case of the fine scale structural effects on the border between cell types that have been identified in this study, as localised inhibition to reduce intermixing during clonal expansion allows kin cells to benefit from local nutrients or any secreted molecules. The use of local interactions allows the benefit to be gained from the attacking cell and its clonemates without the need for extensive killing.

Finally, in Chapter 6, it was possible to use a T6SS effector mutant to validate the trends seen in simulations. It was shown for Δrhs2 rhs1$^{\mathrm{tr}}$ in single cell growth that a lower inhibition rate, with a low growth rate after intoxication as with T6SS, allowed cells to divide more when in contact with inhibitor cells. This reduced level of inhibition compared to WT showed structural difference. Although the inhibition potency was reduced, with a small level of reduced toxicity suggested in simulation, the potency at a single cell level was much higher than CDI. This translated to a more significant structural change with Δrhs2 rhs1$^{\mathrm{tr}}$ than CDI compared to control. However, in population competitions both Δrhs2 rhs1$^{\mathrm{tr}}$ and CDI showed a similar level of CI reduction compared to WT (T6SS) inhibition (Chapter 3, Figure 2 compared to Chapter 6, Figure 37). One idea of how this could happen is that the CDI rRNase toxin [82] has low toxicity but in liquid culture there are enough transient contacts made to insert many toxins and reduce population growth. This is in contrast to Δrhs2 rhs1$^{\mathrm{tr}}$ which has been shown to have reduced T6SS firing as well as reduced number of effectors.

To summarise the main finding of this work, through the use of single cell microscopy a more detailed understanding of the heterogeneic inhibition seen with CDI has been gained, as well as quantification of a T6SS inhibition phenotype that differs from the ones so far explored at a single cell level. Simulations showed that the border between cell types decrease in complexity as inhibition increases, which suggests inhibition causes fine scale structural changes in microcolony growth. Analysing inhibition of a T6SS effector mutant showed that inhibition potency can be manipulated experimentally and model and experimental iteration can give insight into binary interactions. The work presented here adds detail to the understanding of the role of contact inhibition to create spatial segregation through border creation. This segregation and micro-localisation can help to stabilise polymicrobial communities. The impact of gaining a greater understanding of competitive interactions and how they stabilise microbial communities is to use these systems to our advantage in biotechnology. For example in health care competition can be used to engineer microbial communities to resist pathogens or using bacterial toxins in probiotic bacterial strains [144]. Other uses of bacterial competition in industrial and environmental processes include resisting plant pathogens and outcompeting strains that contaminate fermentation such as in cheese making [145]. Furthermore, the model and experimental framework developed here gives scope to further investigation of inhibition landscapes and other interbacterial interactions (Figure 50).

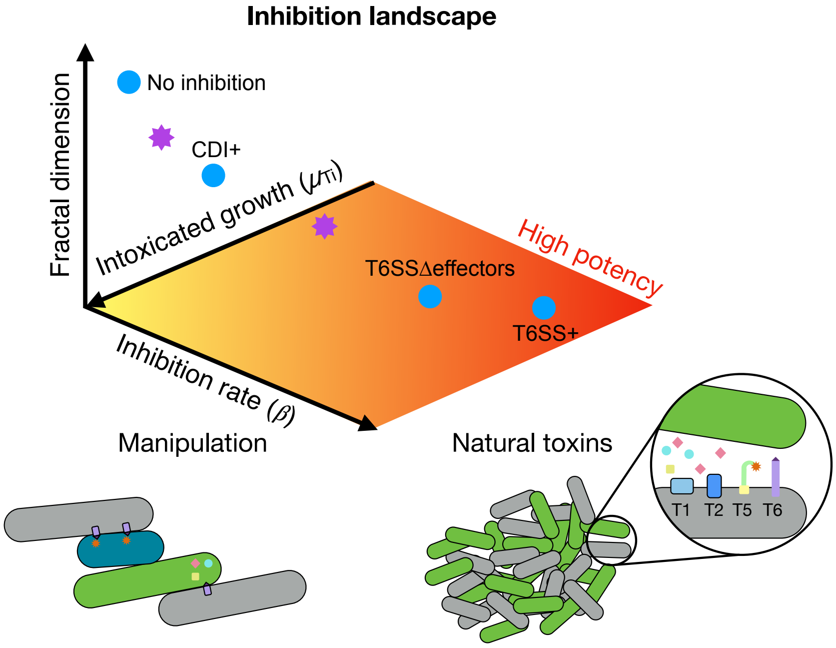

Figure 50: **Exploration of inhibition landscapes using toxins or strains from natural systems and manipulated systems.** Graph demonstrates the interplay between inhibition rate and intoxicated growth rate to change inhibition potency and how this affects structure formation, through changing the Fd values. Systems used in this study as well as prospectively looking at toxins and systems from natural environments and for manipulation of strains.

Abbreviations

BC	Baseplate complex
CDI	Contact dependent inhibition
CT	C-terminal
ECL	*Enterobacter cloacae*
Fd	Fractal dimension
IBM	Individual based model
IM	Inner membrane
KT	Killing time
LB	Lysogeny broth
MC	Membrane complex
OM	Outer membrane
pcf	pair correlation function
PG	Peptidoglycan
SD	Standard deviation
T6SS	Type VI secrection system

References

[1] Michael J. Bottery, Ioannis Passaris, Calvin Dytham, A. Jamie Wood, and Marjan W. van der Woude. Spatial Organization of Expanding Bacterial Colonies Is Affected by Contact-Dependent Growth Inhibition. *Current Biology*, 29(21):3622–3634, 2019.

[2] Thomas Cavalier-Smith, Martin Brasier, and T. Martin Embley. Introduction: How and when did microbes change the world? *Philosophical Transactions of the Royal Society B: Biological Sciences*, 361(1470):845–850, 2006.

[3] J. William Costerton, Zbigniew Lewandowski, Douglas E. Caldwell, Darren R. Korber, and Hilary M. Lappin-Scott. Microbial biofilms. *Annual Review of Microbiology*, 49(1): 711–745, 1995.

[4] Ricardo Cavicchioli, William J. Ripple, Kenneth N. Timmis, Farooq Azam, Lars R. Bakken, Matthew Baylis, Michael J. Behrenfeld, Antje Boetius, Philip W. Boyd, Aimée T. Classen, Thomas W. Crowther, Roberto Danovaro, Christine M. Foreman, Jef Huisman, David A. Hutchins, Janet K. Jansson, David M. Karl, Britt Koskella, David B. Mark Welch, Jennifer B. H. Martiny, Mary Ann Moran, Victoria J. Orphan, David S. Reay, Justin V. Remais, Virginia I. Rich, Brajesh K. Singh, Lisa Y. Stein, Frank J. Stewart, Matthew B. Sullivan, Madeleine J. H. van Oppen, Scott C. Weaver, Eric A. Webb, and Nicole S. Webster. Scientists' warning to humanity: Microorganisms and climate change. *Nature Reviews Microbiology*, 17(9):569–586, 2019.

[5] H. Tschäpe. The spread of plasmids as a function of bacterial adaptability. *FEMS Microbiology Ecology*, 15(1-2):23–31, 1994.

[6] P. Nannipieri, J. Ascher, M. T. Ceccherini, L. Landi, G. Pietramellara, and G. Renella. Microbial diversity and soil functions. *European Journal of Soil Science*, 54(4):655–670, 2003.

[7] Robert Duran and Cristiana Cravo-Laureau. Role of environmental factors and microorganisms in determining the fate of polycyclic aromatic hydrocarbons in the marine environment. *FEMS Microbiology Reviews*, 40(6):814–830, 2016.

[8] Kevin R. Arrigo. Marine microorganisms and global nutrient cycles. *Nature*, 437(7057): 349–355, 2005.

[9] N. DeLeon-Rodriguez, T. L. Lathem, L. M. Rodriguez-R, J. M. Barazesh, B. E. Anderson, A. J. Beyersdorf, L. D. Ziemba, M. Bergin, A. Nenes, and K. T. Konstantinidis. Microbiome of the upper troposphere: Species composition and prevalence, effects of tropical storms, and atmospheric implications. *Proceedings of the National Academy of Sciences*, 110(7): 2575–2580, 2013.

[10] Jian Xu and Jeffrey I. Gordon. Honor thy symbionts. *Proceedings of the National Academy of Sciences*, 100(18):10452–10459, 2003.

[11] Laura Wegener Parfrey, Corrie S. Moreau, and Jacob A. Russell. The host-associated microbiome: Pattern, process and function. *Molecular Ecology*, 27(8):1749–1765, 2018.

[12] Harry J. Flint, Sylvia H. Duncan, Karen P. Scott, and Petra Louis. Interactions and competition within the microbial community of the human colon: Links between diet and health. *Environmental Microbiology*, 9(5):1101–1111, 2007.

[13] Stefanie Widder, Rosalind J Allen, Thomas Pfeiffer, Thomas P Curtis, Carsten Wiuf, William T Sloan, Otto X Cordero, Sam P Brown, Babak Momeni, Wenying Shou, Helen Kettle, Harry J Flint, Andreas F Haas, Béatrice Laroche, Jan-Ulrich Kreft, Paul B Rainey, Shiri Freilich, Stefan Schuster, Kim Milferstedt, Jan R van der Meer, Tobias Grosskopf, Jef Huisman, Andrew Free, Cristian Picioreanu, Christopher Quince, Isaac Klapper, Simon Labarthe, Barth F Smets, Harris Wang, and Orkun S Soyer. Challenges in microbial ecology: Building predictive understanding of community function and dynamics. *The ISME Journal*, 10(11):2557–2568, 2016.

[14] Luanne Hall-Stoodley, J. William Costerton, and Paul Stoodley. Bacterial biofilms: From the Natural environment to infectious diseases. *Nature Reviews Microbiology*, 2(2):95–108, 2004.

[15] P. Stoodley, K. Sauer, D. G. Davies, and J. W. Costerton. Biofilms as Complex Differentiated Communities. *Annual Review of Microbiology*, 56(1):187–209, 2002.

[16] Hans-Curt Flemming, Jost Wingender, Ulrich Szewzyk, Peter Steinberg, Scott A. Rice, and Staffan Kjelleberg. Biofilms: An emergent form of bacterial life. *Nature Reviews Microbiology*, 14(9):563–575, 2016.

[17] Stuart A. West, Stephen P. Diggle, Angus Buckling, Andy Gardner, and Ashleigh S. Griffin. The Social Lives of Microbes. *Annual Review of Ecology, Evolution, and Systematics*, 38 (1):53–77, 2007.

[18] Pieter Moons, Chris W. Michiels, and Abram Aertsen. Bacterial interactions in biofilms. *Critical Reviews in Microbiology*, 35(3):157–168, 2009.

[19] Katharine Z. Coyte, Jonas Schluter, and Kevin R. Foster. The ecology of the microbiome: Networks, competition, and stability. *Science*, 350(6261):663–666, 2015.

[20] Melanie Ghoul and Sara Mitri. The Ecology and Evolution of Microbial Competition. *Trends in Microbiology*, 24(10):833–845, 2016.

[21] Elisa T. Granato, Thomas A. Meiller-Legrand, and Kevin R. Foster. The Evolution and Ecology of Bacterial Warfare. *Current Biology*, 29(11):521–537, 2019.

[22] Anne Jamet and Xavier Nassif. New Players in the Toxin Field: Polymorphic Toxin Systems in Bacteria. *mBio*, 6(3), 2015.

[23] Dapeng Zhang, Robson F de Souza, Vivek Anantharaman, Lakshminarayan M Iyer, and L Aravind. Polymorphic toxin systems: Comprehensive characterization of trafficking modes, processing, mechanisms of action, immunity and ecology using comparative genomics. *Biology Direct*, 7:18, 2012.

[24] Fernando Navarro-Garcia, Fernando Ruiz-Perez, Ángel Cataldi, and Mariano Larzábal. Type VI Secretion System in Pathogenic Escherichia coli: Structure, Role in Virulence, and Acquisition. *Frontiers in Microbiology*, 10, 2019.

[25] L Chao and B R Levin. Structured habitats and the evolution of anticompetitor toxins in bacteria. *Proceedings of the National Academy of Sciences of the United States of America*, 78(10):6324–6328, 1981.

[26] Rick Durrett and Simon Levin. Allelopathy in Spatially Distributed Populations. *Journal of Theoretical Biology*, 185(2):165–171, 1997.

[27] Benjamin Kerr, Margaret A. Riley, Marcus W. Feldman, and Brendan J. M. Bohannan. Local dispersal promotes biodiversity in a real-life game of rock–paper–scissors. *Nature*, 418(6894):171–174, 2002.

[28] Stephanie K. Aoki, Elie J. Diner, Claire t'Kint de Roodenbeke, Brandt R. Burgess, Stephen J. Poole, Bruce A. Braaten, Allison M. Jones, Julia S. Webb, Christopher S. Hayes, Peggy A. Cotter, and David A. Low. A widespread family of polymorphic contact-dependent toxin delivery systems in bacteria. *Nature*, 468(7322):439–442, 2010.

[29] Lewis EH Bingle, Christopher M Bailey, and Mark J Pallen. Type VI secretion: A beginner's guide. *Current Opinion in Microbiology*, 11(1):3–8, 2008.

[30] Stephanie K. Aoki, Rupinderjit Pamma, Aaron D. Hernday, Jessica E. Bickham, Bruce A. Braaten, and David A. Low. Contact-Dependent Inhibition of Growth in Escherichia coli. *Science*, 309(5738):1245–1248, 2005.

[31] Laura E. Holberger, Fernando Garza-Sánchez, James Lamoureux, David A. Low, and Christopher S. Hayes. A novel family of toxin/antitoxin proteins in Bacillus species. *Febs Letters*, 586(2):132–136, 2012.

[32] Jérémy Guérin Françoise Jacob-Dubuisson. Two-partner secretion: As simple as it sounds? *Research in microbiology*, 164(6), 2013.

[33] Catherine Baud, Jérémy Guérin, Emmanuelle Petit, Elodie Lesne, Elian Dupré, Camille Locht, and Françoise Jacob-Dubuisson. Translocation path of a substrate protein through its Omp85 transporter. *Nature Communications*, 5:5271, 2014.

[34] Zachary C. Ruhe, Josephine Y. Nguyen, Jing Xiong, Sanna Koskiniemi, Christina M. Beck, Basil R. Perkins, David A. Low, and Christopher S. Hayes. CdiA Effectors Use Modular Receptor-Binding Domains To Recognize Target Bacteria. *mBio*, 8(2):e00290–17, 2017.

[35] Andrey V. Kajava, Naiqian Cheng, Ryan Cleaver, Martin Kessel, Martha N. Simon, Eve Willery, Francoise Jacob-Dubuisson, Camille Locht, and Alasdair C. Steven. Beta-helix model for the filamentous haemagglutinin adhesin of Bordetella pertussis and related bacterial secretory proteins. *Molecular Microbiology*, 42(2):279–292, 2001.

[36] Zachary C. Ruhe, Poorna Subramanian, Kiho Song, Josephine Y. Nguyen, Taylor A. Stevens, David A. Low, Grant J. Jensen, and Christopher S. Hayes. Programmed Secretion Arrest and Receptor-Triggered Toxin Export during Antibacterial Contact-Dependent Growth Inhibition. *Cell*, 175(4):921–933.e14, 2018.

[37] Julia L. E. Willett, Grant C. Gucinski, Jackson P. Fatherree, David A. Low, and Christopher S. Hayes. Contact-dependent growth inhibition toxins exploit multiple independent cell-entry pathways. *Proceedings of the National Academy of Sciences of the United States of America*, 112(36):11341–11346, 2015.

[38] Stephanie K. Aoki, Juliana C. Malinverni, Kyle Jacoby, Benjamin Thomas, Rupinderjit Pamma, Brooke N. Trinh, Susan Remers, Julia Webb, Bruce A. Braaten, Thomas J. Silhavy, and David A. Low. Contact-dependent growth inhibition requires the essential outer

membrane protein BamA (YaeT) as the receptor and the inner membrane transport protein AcrB. *Molecular microbiology*, 70(2):323–340, 2008.

[39] Christina M. Beck, Julia L. E. Willett, David A. Cunningham, Jeff J. Kim, David A. Low, and Christopher S. Hayes. CdiA Effectors from Uropathogenic Escherichia coli Use Heterotrimeric Osmoporins as Receptors to Recognize Target Bacteria. *PLOS Pathog*, 12 (10):e1005925, 2016.

[40] Elie J. Diner, Christina M. Beck, Julia S. Webb, David A. Low, and Christopher S. Hayes. Identification of a target cell permissive factor required for contact-dependent growth inhibition (CDI). *Genes & Development*, 26(5):515–525, 2012.

[41] Parker M. Johnson, Christina M. Beck, Robert P. Morse, Fernando Garza-Sánchez, David A. Low, Christopher S. Hayes, and Celia W. Goulding. Unraveling the essential role of CysK in CDI toxin activation. *Proceedings of the National Academy of Sciences*, 113(35):9792–9797, 2016.

[42] Allison M. Jones, Fernando Garza-Sánchez, Jaime So, Christopher S. Hayes, and David A. Low. Activation of contact-dependent antibacterial tRNase toxins by translation elongation factors. *Proceedings of the National Academy of Sciences*, 114(10):E1951–E1957, 2017.

[43] Stephen J. Poole, Elie J. Diner, Stephanie K. Aoki, Bruce A. Braaten, Claire t'Kint de Roodenbeke, David A. Low, and Christopher S. Hayes. Identification of Functional Toxin/Immunity Genes Linked to Contact-Dependent Growth Inhibition (CDI) and Rearrangement Hotspot (Rhs) Systems. *PLoS Genetics*, 7(8), 2011.

[44] Zachary C. Ruhe, Josephine Y. Nguyen, Annette J. Chen, Nicole Y. Leung, Christopher S. Hayes, and David A. Low. CDI Systems Are Stably Maintained by a Cell-Contact Mediated Surveillance Mechanism. *PLOS Genet*, 12(6):e1006145, 2016.

[45] Erin C. Garcia, Melissa S. Anderson, Jon A. Hagar, and Peggy A. Cotter. Burkholderia BcpA mediates biofilm formation independently of interbacterial contact dependent growth inhibition. *Molecular microbiology*, 89(6):1213–1225, 2013.

[46] Melissa S. Anderson, Erin C. Garcia, and Peggy A. Cotter. Kind Discrimination and Competitive Exclusion Mediated by Contact-Dependent Growth Inhibition Systems Shape Biofilm Community Structure. *PLOS Pathog*, 10(4):e1004076, 2014.

[47] Zachary C. Ruhe, Loni Townsley, Adam B. Wallace, Andrew King, Marjan W. Van der Woude, David A. Low, Fitnat H. Yildiz, and Christopher S. Hayes. CdiA promotes receptor-independent intercellular adhesion. *Molecular Microbiology*, 98(1):175–192, 2015.

[48] Morgane Roussin, Sedera Rabarioelina, Laurence Cluzeau, Julien Cayron, Christian Lesterlin, Suzana P. Salcedo, and Sarah Bigot. Identification of a Contact-Dependent Growth Inhibition (CDI) System That Reduces Biofilm Formation and Host Cell Adhesion of Acinetobacter baumannii DSM30011 Strain. *Frontiers in Microbiology*, 10:2450, 2019.

[49] Anirban Ghosh, Özden Baltekin, Marcus Wäneskog, Dina Elkhalifa, Disa L. Hammarlöf, Johan Elf, and Sanna Koskiniemi. Contact-dependent growth inhibition induces high levels of antibiotic-tolerant persister cells in clonal bacterial populations. *The EMBO Journal*, 37(9):e98026, 2018.

[50] Erin C. Garcia, Andrew I. Perault, Sara A. Marlatt, and Peggy A. Cotter. Interbacterial signaling via Burkholderia contact-dependent growth inhibition system proteins. *Proceedings of the National Academy of Sciences*, 113(29):8296–8301, 2016.

[51] Stefan Pukatzki, Amy T. Ma, Derek Sturtevant, Bryan Krastins, David Sarracino, William C. Nelson, John F. Heidelberg, and John J. Mekalanos. Identification of a conserved bacterial protein secretion system in Vibrio cholerae using the Dictyostelium host model system. *Proceedings of the National Academy of Sciences of the United States of America*, 103(5):1528–1533, 2006.

[52] Alain Filloux, Abderrahman Hachani, and Sophie Bleves. The bacterial type VI secretion machine: Yet another player for protein transport across membranes. *Microbiology,*, 154 (6):1570–1583, 2008.

[53] Sarah Coulthurst. The Type VI secretion system: A versatile bacterial weapon. *Microbiology*, 165(5), 2019.

[54] Kaitlyn D. LaCourse, S. Brook Peterson, Hemantha D. Kulasekara, Matthew C. Radey, Jungyun Kim, and Joseph D. Mougous. Conditional toxicity and synergy drive diversity among antibacterial effectors. *Nature Microbiology*, 3:440–446, 2018.

[55] Sarah T. Miyata, Verena Bachmann, and Stefan Pukatzki. Type VI secretion system regulation as a consequence of evolutionary pressure. *Journal of Medical Microbiology,*, 62 (5):663–676, 2013.

[56] Daniel F. Aubert, Ronald S. Flannagan, and Miguel A. Valvano. A Novel Sensor Kinase-Response Regulator Hybrid Controls Biofilm Formation and Type VI Secretion System Activity in Burkholderia cenocepacia. *Infection and Immunity*, 76(5):1979–1991, 2008.

[57] Milena Jaskólska, Sandrine Stutzmann, Candice Stoudmann, and Melanie Blokesch. QstR-dependent regulation of natural competence and type VI secretion in Vibrio cholerae. *Nucleic Acids Research*, 46(20):10619–10634, 2018.

[58] Lisa C. Metzger, Sandrine Stutzmann, Tiziana Scrignari, Charles Van der Henst, Noémie Matthey, and Melanie Blokesch. Independent Regulation of Type VI Secretion in Vibrio cholerae by TfoX and TfoY. *Cell Reports*, 15(5):951–958, 2016.

[59] Xiaolong Shao, Xiaoning Zhang, Yingchao Zhang, Miao Zhu, Pan Yang, Jian Yuan, Yingpeng Xie, Tianhong Zhou, Wei Wang, Sheng Chen, Haihua Liang, and Xin Deng. RpoN-Dependent Direct Regulation of Quorum Sensing and the Type VI Secretion System in Pseudomonas aeruginosa PAO1. *Journal of Bacteriology*, 200(16):e00205–18, 2018.

[60] Jun Zheng, Ok S. Shin, D. Ewen Cameron, and John J. Mekalanos. Quorum sensing and a global regulator TsrA control expression of type VI secretion and virulence in Vibrio cholerae. *Proceedings of the National Academy of Sciences of the United States of America*, 107(49):21128–21133, 2010.

[61] Christophe S. Bernard, Yannick R. Brunet, Erwan Gueguen, and Eric Cascales. Nooks and Crannies in Type VI Secretion Regulation. *Journal of Bacteriology*, 192(15):3850–3860, 2010.

[62] Adam Ostrowski, Francesca R. Cianfanelli, Michael Porter, Giuseppina Mariano, Julien Peltier, Jun Jie Wong, Jason R. Swedlow, Matthias Trost, and Sarah J. Coulthurst. Killing with proficiency: Integrated post-translational regulation of an offensive Type VI secretion system. *PLOS Pathogens*, 14(7):e1007230, 2018.

[63] Marek Basler, Brian T. Ho, and John J. Mekalanos. Tit-for-tat: Type VI secretion system counterattack during bacterial cell-cell interactions. *Cell*, 152(4):884–894, 2013.

[64] M. Basler and J. J. Mekalanos. Type 6 secretion dynamics within and between bacterial cells. *Science (New York, N.Y.)*, 337(6096):815, 2012.

[65] Ka Yin Leung, Bupe A Siame, Heather Snowball, and Yu-Keung Mok. Type VI secretion regulation: Crosstalk and intracellular communication. *Current Opinion in Microbiology*, 14(1):9–15, 2011.

[66] Abderrahman Hachani, Thomas E Wood, and Alain Filloux. Type VI secretion and anti-host effectors. *Current Opinion in Microbiology*, 29:81–93, 2016.

[67] Lauren Speare, Andrew G. Cecere, Kirsten R. Guckes, Stephanie Smith, Michael S. Wollenberg, Mark J. Mandel, Tim Miyashiro, and Alecia N. Septer. Bacterial symbionts use a type VI secretion system to eliminate competitors in their natural host. *Proceedings of the National Academy of Sciences*, 115(36):E8528–E8537, 2018.

[68] Aaron L. Hecht, Benjamin W. Casterline, Zachary M. Earley, Young Ah Goo, David R. Goodlett, and Juliane Bubeck Wardenburg. Strain competition restricts colonization of an enteric pathogen and prevents colitis. *EMBO reports*, 17(9):e201642282, 2016.

[69] Vera Troselj and Daniel Wall. Metabolic disharmony and sibling conflict mediated by T6SS. *Microbial Cell*, 5(5):256–258, 2018.

[70] Sandrine Borgeaud, Lisa C. Metzger, Tiziana Scrignari, and Melanie Blokesch. The type VI secretion system of Vibrio cholerae fosters horizontal gene transfer. *Science*, 347(6217): 63–67, 2015.

[71] S. K. Aoki, J. S. Webb, B. A. Braaten, and D. A. Low. Contact-Dependent Growth Inhibition Causes Reversible Metabolic Downregulation in Escherichia coli. *Journal of Bacteriology*, 191(6):1777–1786, 2009.

[72] Angelica B. Ocasio and Peggy A. Cotter. CDI/CDS system-encoding genes of burkholderia thailandensis are located in a mobile genetic element that defines a new class of transposon. *PLOS Genetics*, 15(1):e1007883, 2019.

[73] Laure Journet and Eric Cascales. The Type VI Secretion System in Escherichia coli and Related Species. *EcoSal Plus*, 7(1), 2016.

[74] Andrew E. Blanchard, Venhar Celik, and Ting Lu. Extinction, coexistence, and localized patterns of a bacterial population with contact-dependent inhibition. *BMC Systems Biology*, 8(1):23, 2014.

[75] Bruno MC Martins and James CW Locke. Microbial individuality: How single-cell heterogeneity enables population level strategies. *Current Opinion in Microbiology*, 24:104–112, 2015.

[76] David Bruce Borenstein, Peter Ringel, Marek Basler, and Ned S. Wingreen. Established microbial colonies can survive type vi secretion assault. *PLoS Comput Biol*, 11(10):e1004520, 2015.

[77] Megan J. Q. Wong, Xiaoye Liang, Matt Smart, Le Tang, Richard Moore, Brian Ingalls, and Tao G. Dong. Microbial Herd Protection Mediated by Antagonistic Interaction in Polymicrobial Communities. *Applied and Environmental Microbiology*, 82(23):6881–6888, 2016.

[78] Luke McNally, Eryn Bernardy, Jacob Thomas, Arben Kalziqi, Jennifer Pentz, Sam P. Brown, Brian K. Hammer, Peter J. Yunker, and William C. Ratcliff. Killing by Type VI secretion drives genetic phase separation and correlates with increased cooperation. *Nature Communications*, 8:14371, 2017.

[79] Jared L. Wilmoth, Peter W. Doak, Andrea Timm, Michelle Halsted, John D. Anderson, Marta Ginovart, Clara Prats, Xavier Portell, Scott T. Retterer, and Miguel Fuentes-Cabrera. A microfluidics and agent-based modeling framework for investigating spatial organization in bacterial colonies: The case of pseudomonas aeruginosa and h1-type vi secretion interactions. *Frontiers in Microbiology*, 9:33, 2018.

[80] Liyang Xiong, Robert Cooper, and Lev S. Tsimring. Coexistence and Pattern Formation in Bacterial Mixtures with Contact-Dependent Killing. *Biophysical Journal*, 114(7):1741–1750, 2018.

[81] Giuseppina Mariano, Katharina Trunk, David J. Williams, Laura Monlezun, Henrik Strahl, Samantha J. Pitt, and Sarah J. Coulthurst. A family of Type VI secretion system effector proteins that form ion-selective pores. *Nature Communications*, 10(1):1–15, 2019.

[82] Christina M. Beck, Robert P. Morse, David A. Cunningham, Angelina Iniguez, David A. Low, Celia W. Goulding, and Christopher S. Hayes. CdiA from Enterobacter cloacae delivers a toxic ribosomal RNase into target bacteria. *Structure (London, England : 1993)*, 22(5):707–718, 2014.

[83] Class II Contact-Dependent growth Inhibition (CDI) systems allow for broad-range cross-species toxin delivery within the Enterobacteriaceae family. 111:1109–1125.

[84] Sonya Donato, David A. Low, and Christopher S. Hayes. Unpublished data on t6ss in *E. cloacae*. *UCSB*, 2019.

[85] Anne Davin-Regli and Jean-Marie Pagès. Enterobacter aerogenes and Enterobacter cloacae; versatile bacterial pathogens confronting antibiotic treatment. *Frontiers in Microbiology*, 6:392, 2015.

[86] M. Dalben, G. Varkulja, M. Basso, V. L. J. Krebs, M. A. Gibelli, I. van der Heijden, F. Rossi, G. Duboc, A. S. Levin, and S. F. Costa. Investigation of an outbreak of Enterobacter cloacae in a neonatal unit and review of the literature. *Journal of Hospital Infection*, 70(1):7–14, 2008.

[87] Ana Fernández, María José Pereira, José Manuel Suárez, Margarita Poza, Mercedes Treviño, Pilar Villalón, Juan Antonio Sáez-Nieto, Benito José Regueiro, Rosa Villanueva, and Germán Bou. Emergence in Spain of a Multidrug-Resistant Enterobacter cloacae Clinical Isolate Producing SFO-1 Extended-Spectrum beta-Lactamase. *Journal of Clinical Microbiology*, 49(3):822–828, 2011.

[88] Michele LeRoux, Justin A. De Leon, Nathan J. Kuwada, Alistair B. Russell, Delia Pinto-Santini, Rachel D. Hood, Danielle M. Agnello, Stephen M. Robertson, Paul A. Wiggins, and Joseph D. Mougous. Quantitative single-cell characterization of bacterial interactions reveals type VI secretion is a double-edged sword. *Proceedings of the National Academy of Sciences of the United States of America*, 109(48):19804–19809, 2012.

[89] Yannick R. Brunet, Leon Espinosa, Seddik Harchouni, Tâm Mignot, and Eric Cascales. Imaging Type VI Secretion-Mediated Bacterial Killing. *Cell Reports*, 3(1):36–41, 2013.

[90] Ferdi L. Hellweger, Robert J. Clegg, James R. Clark, Caroline M. Plugge, and Jan-Ulrich Kreft. Advancing microbial sciences by individual-based modelling. *Nature Reviews Microbiology*, advance online publication, 2016.

[91] Aisling J. Daly, Ward Quaghebeur, Tim M. A. Depraetere, Jan M. Baetens, and Bernard De Baets. Lattice-based versus lattice-free individual-based models: Impact on coexistence in competitive communities. *Natural Computing*, 18(4):855–864, 2019.

[92] Timothy J. Rudge, Paul J. Steiner, Andrew Phillips, and Jim Haseloff. Computational Modeling of Synthetic Microbial Biofilms. *ACS Synthetic Biology*, 1(8):345–352, 2012.

[93] Timothy J. Rudge, Fernán Federici, Paul J. Steiner, Anton Kan, and Jim Haseloff. Cell Polarity-Driven Instability Generates Self-Organized, Fractal Patterning of Cell Layers. *ACS Synthetic Biology*, 2(12):705–714, 2013.

[94] Bruno MC Martins and James CW Locke. Microbial individuality: How single-cell heterogeneity enables population level strategies. *Current Opinion in Microbiology*, 24:104–112, 2015.

[95] James C. W. Locke and Michael B. Elowitz. Using movies to analyse gene circuit dynamics in single cells. *Nature Reviews Microbiology*, 7(5):383–392, 2009.

[96] Thorsten Wiegand and Kirk A. Moloney. Rings, circles, and null-models for point pattern analysis in ecology. *Oikos*, 104(2):209–229, 2004.

[97] D. J. G. Agnew, J. E. F. Green, T. M. Brown, M. J. Simpson, and B. J. Binder. Distinguishing between mechanisms of cell aggregation using pair-correlation functions. *Journal of Theoretical Biology*, 352:16–23, 2014.

[98] Benjamin J. Binder and Matthew J. Simpson. Quantifying spatial structure in experimental observations and agent-based simulations using pair-correlation functions. *Physical Review E*, 88(2), 2013.

[99] S. Dini, B. J. Binder, and J. E. F. Green. Understanding interactions between populations: Individual based modelling and quantification using pair correlation functions. *Journal of Theoretical Biology*, 439:50–64, 2018.

[100] W.S. Rasband. Imagej. *U. S. National Institutes of Health, Bethesda, Maryland, USA*, 997-2018. URL https://imagej.nih.gov/ij/.

[101] Michael J. Bottery. Unpublished method for calculating the fractal dimension on binary images written in python. *Univeristy of York*, 2019.

[102] Adrian Baddeley, Ege Rubak, and Rolf Turner. *Spatial Point Patterns: Methodology and Applications with R*, volume Chapter 7. Chapman & Hall/CRC, 2016.

[103] Adrian Baddeley, Ege Rubak, and Rolf Turner. *Spatial Point Patterns: Methodology and Applications with R*. Chapman and Hall/CRC Press, London, 2015.

[104] Zachary C. Ruhe, Adam B. Wallace, David A. Low, and Christopher S. Hayes. Receptor Polymorphism Restricts Contact-Dependent Growth Inhibition to Members of the Same Species. *mBio*, 4(4):e00480–13, 2013.

[105] Jun Zheng, Brian Ho, and John J. Mekalanos. Genetic Analysis of Anti-Amoebae and Anti-Bacterial Activities of the Type VI Secretion System in Vibrio cholerae. *PLoS ONE*, 6(8), 2011.

[106] Nitzan Rosenfeld, Jonathan W. Young, Uri Alon, Peter S. Swain, and Michael B. Elowitz. Gene Regulation at the Single-Cell Level. *Science*, 307(5717):1962–1965, 2005.

[107] Daniel J. Kiviet, Philippe Nghe, Noreen Walker, Sarah Boulineau, Vanda Sunderlikova, and Sander J. Tans. Stochasticity of metabolism and growth at the single-cell level. *Nature*, 514(7522):376–379, 2014.

[108] Johan H. van Heerden, Hermannus Kempe, Anne Doerr, Timo Maarleveld, Niclas Nordholt, and Frank J. Bruggeman. Statistics and simulation of growth of single bacterial cells: Illustrations with B. subtilis and E. coli. *Scientific Reports*, 7(1):16094, 2017.

[109] Johannes Klein, Stefan Leupold, Ilona Biegler, Rebekka Biedendieck, Richard Münch, and Dieter Jahn. TLM-Tracker: Software for cell segmentation, tracking and lineage analysis in time-lapse microscopy movies. *Bioinformatics*, 28(17):2276–2277, 2012.

[110] Ahmad Paintdakhi, Bradley Parry, Manuel Campos, Irnov Irnov, Johan Elf, Ivan Surovtsev, and Christine Jacobs-Wagner. Oufti: An integrated software package for high-accuracy, high-throughput quantitative microscopy analysis. *Molecular Microbiology*, 2016.

[111] Stella Stylianidou, Connor Brennan, Silas B. Nissen, Nathan J. Kuwada, and Paul A. Wiggins. SuperSegger: Robust image segmentation, analysis and lineage tracking of bacterial cells. *Molecular Microbiology*, 102(4):690–700, 2016.

[112] Elowitz Lab. Schnitzcells User's Manual: Software for quantitative analysis of time-lapse movies. 2011. URL `https://biii.eu/schnitzcells`.

[113] Athanasios D. Balomenos, Panagiotis Tsakanikas, Zafiro Aspridou, Anastasia P. Tampakaki, Konstantinos P. Koutsoumanis, and Elias S. Manolakos. Image analysis driven single-cell analytics for systems microbiology. *BMC Systems Biology*, 11(1):43, 2017.

[114] T. G. Smith, G. D. Lange, and W. B. Marks. Fractal methods and results in cellular morphology — dimensions, lacunarity and multifractals. *Journal of Neuroscience Methods*, 69(2):123–136, 1996.

[115] A Karperien. FracLac for ImageJ, 1999/2013.

[116] Dominique Bérubé and Michel Jébrak. High precision boundary fractal analysis for shape characterization. *Computers & Geosciences*, 25(9):1059–1071, 1999.

[117] K Foroutan-pour, P Dutilleul, and D. L Smith. Advances in the implementation of the box-counting method of fractal dimension estimation. *Applied Mathematics and Computation*, 105(2):195–210, 1999.

[118] Jan-Ulrich Kreft, Caroline M. Plugge, Volker Grimm, Clara Prats, Johan H. J. Leveau, Thomas Banitz, Stephen Baines, James Clark, Alexandra Ros, Isaac Klapper, Chris J. Topping, Anthony J. Field, Andrew Schuler, Elena Litchman, and Ferdi L. Hellweger. Mighty small: Observing and modeling individual microbes becomes big science. *Proceedings of the National Academy of Sciences*, 110(45):18027–18028, 2013.

[119] Jack A Tuszynski, Philip Winter, Diana White, Chih-Yuan Tseng, Kamlesh K Sahu, Francesco Gentile, Ivana Spasevska, Sara Ibrahim Omar, Niloofar Nayebi, Cassandra DM Churchill, Mariusz Klobukowski, and Rabab M Abou El-Magd. Mathematical and computational modeling in biology at multiple scales. *Theoretical Biology and Medical Modelling*, 11(1):52, 2014.

[120] Şebnem Bora and Sevcan Emek. Agent-Based Modeling and Simulation of Biological Systems. *Computer Simulation*, 2018.

[121] Venhar Celik Ozgen, Wentao Kong, Andrew E. Blanchard, Feng Liu, and Ting Lu. Spatial interference scale as a determinant of microbial range expansion. *Science Advances*, 4(11): eaau0695, 2018.

[122] William P. J. Smith, Yohan Davit, James M. Osborne, Wook Kim, Kevin R. Foster, and Joe M. Pitt-Francis. Cell morphology drives spatial patterning in microbial communities. *Proceedings of the National Academy of Sciences*, 114(3):E280–E286, 2017.

[123] Michael A. Gibson and Jehoshua Bruck. Efficient exact stochastic simulation of chemical systems with many species and many channels. *The Journal of Physical Chemistry A*, 104 (9):1876–1889, 2000.

[124] Daniel T. Gillespie. Exact stochastic simulation of coupled chemical reactions. *Journal of Physical Chemistry*, 81(25):2340–2361, 1977.

[125] Alistair B. Russell, Michele LeRoux, Krisztina Hathazi, Danielle M. Agnello, Takahiko Ishikawa, Paul A. Wiggins, Sun Nyunt Wai, and Joseph D. Mougous. Diverse type vi secretion phospholipases are functionally plastic antibacterial effectors. *Nature*, 496(7446): 508–512, 2013.

[126] Nicolas Flaugnatti, Thi Thu Hang Le, Stéphane Canaan, Marie-Stéphanie Aschtgen, Van Son Nguyen, Stéphanie Blangy, Christine Kellenberger, Alain Roussel, Christian Cambillau, Eric Cascales, and Laure Journet. A phospholipase a1 antibacterial type vi secretion effector interacts directly with the c-terminal domain of the vgrg spike protein for delivery. *Molecular Microbiology*, 99(6):1099–1118, 2016.

[127] Alistair B. Russell, Pragya Singh, Mitchell Brittnacher, Nhat Khai Bui, Rachel D. Hood, Mike A. Carl, Danielle M. Agnello, Sandra Schwarz, David R. Goodlett, Waldemar Vollmer, and Joseph D. Mougous. A widespread bacterial type VI secretion effector superfamily identified using a heuristic approach. *Cell host & microbe*, 11(5):538–549, 2012.

[128] Peter David Ringel, Di Hu, and Marek Basler. The role of type vi secretion system effectors in target cell lysis and subsequent horizontal gene transfer. *Cell Reports*, 21(13):3927–3940, 2017.

[129] Thomas Trunk, Hawzeen S. Khalil, and Jack C. Leo. Bacterial autoaggregation. *AIMS Microbiology*, 4(1):140–164, 2018-03-01.

[130] Carey D. Nadell, Kevin R. Foster, and João B. Xavier. Emergence of spatial structure in cell groups and the evolution of cooperation. *PLOS Computational Biology*, 6(3):e1000716, 2010.

[131] Oskar Hallatschek, Pascal Hersen, Sharad Ramanathan, and David R. Nelson. Genetic drift at expanding frontiers promotes gene segregation. *Proceedings of the National Academy of Sciences of the United States of America*, 104(50):19926–19930, 2007.

[132] Juliana Alcoforado Diniz, Yi-Chia Liu, and Sarah J. Coulthurst. Molecular weaponry: Diverse effectors delivered by the Type VI secretion system. *Cellular Microbiology*, 17(12): 1742–1751, 2015.

[133] Mikhail M. Shneider, Sergey A. Buth, Brian T. Ho, Marek Basler, John J. Mekalanos, and Petr G. Leiman. PAAR-repeat proteins sharpen and diversify the type VI secretion system spike. *Nature*, 500(7462):350–353, 2013.

[134] Ying Peng, Xiangru Wang, Jin Shou, Bingbing Zong, Yanyan Zhang, Jia Tan, Jing Chen, Linlin Hu, Yongwei Zhu, Huanchun Chen, and Chen Tan. Roles of Hcp family proteins in the pathogenesis of the porcine extraintestinal pathogenic Escherichia coli type VI secretion system. *Scientific Reports*, 6(26816), 2016.

[135] David Yanni, Pedro Márquez-Zacarías, Peter J. Yunker, and William C. Ratcliff. Drivers of Spatial Structure in Social Microbial Communities. *Current Biology*, 29(11):R545–R550, 2019.

[136] Luke McNally and Sam P. Brown. Microbiome: Ecology of stable gut communities. *Nature Microbiology*, 1:15016, 2016.

[137] Thomas E. Wood, Sophie A. Howard, Andreas Förster, Laura M. Nolan, Eleni Manoli, Nathan P. Bullen, Hamish C. L. Yau, Abderrahman Hachani, Richard D. Hayward, John C. Whitney, Waldemar Vollmer, Paul S. Freemont, and Alain Filloux. The Pseudomonas aeruginosa T6SS Delivers a Periplasmic Toxin that Disrupts Bacterial Cell Morphology. *Cell Reports*, 29(1):187–201, 2019.

[138] Hanna Chen, Qian Fang, Qiang Tu, Chenlang Liu, Jia Yin, Yulong Yin, Liqiu Xia, Xiaoying Bian, and Youming Zhang. Identification of a contact-dependent growth inhibition system in the probiotic Escherichia coli Nissle 1917. *FEMS Microbiology Letters*, 365(11), 2018.

[139] Jiale Ma, Min Sun, Zihao Pan, Chengping Lu, and Huochun Yao. Diverse toxic effectors are harbored by vgrG islands for interbacterial antagonism in type VI secretion system. *Biochimica et Biophysica Acta (BBA) - General Subjects*, 1862(7):1635–1643, 2018.

[140] Jeffrey A. Melvin, Jordan R. Gaston, Shawn N. Phillips, Michael J. Springer, Christopher W. Marshall, Robert M. Q. Shanks, and Jennifer M. Bomberger. Pseudomonas aeruginosa Contact-Dependent Growth Inhibition Plays Dual Role in Host-Pathogen Interactions. *mSphere*, 2(6):e00336–17, 2017.

[141] Andrew I. Perault and Peggy A. Cotter. Three Distinct Contact-Dependent Growth Inhibition Systems Mediate Interbacterial Competition by the Cystic Fibrosis Pathogen Burkholderia dolosa. *Journal of Bacteriology*, 200(22), 2018.

[142] Wenzheng Liu, Samuel Jacquiod, Asker Brejnrod, Jakob Russel, Mette Burmølle, and Søren J. Sørensen. Deciphering links between bacterial interactions and spatial organization in multispecies biofilms. *The ISME Journal*, 13:3054–3066, 2019.

[143] J. M. Biernaskie, A. Gardner, and S. A. West. Multicoloured greenbeards, bacteriocin diversity and the rock-paper-scissors game. *Journal of Evolutionary Biology*, 26(10):2081–2094, 2013.

[144] Baizhen Gao, Rushant Sabnis, Tommaso Costantini, Robert Jinkerson, and Qing Sun. A peek in the micro-sized world: a review of design principles, engineering tools, and

applications of engineered microbial community. *Biochemical Society Transactions*, 48(2): 399–409, 2020.

[145] Michael E. Hibbing, Clay Fuqua, Matthew R. Parsek, and S. Brook Peterson. Bacterial competition: surviving and thriving in the microbial jungle. *Nature reviews. Microbiology*, 8(1):15–25, 2010.